LIGHT ALKANES TO HIGHER MOLECULAR WEIGHT OLEFINS: CATALYSTS FOR PROPANE DEHYDROGENATION AND ETHYLENE OLIGOMERIZATION

by

Laryssa Gonçalves Cesar

A Dissertation

Submitted to the Faculty of Purdue University

In Partial Fulfillment of the Requirements for the degree of

Doctor of Philosophy

Davidson School of Chemical Engineering

West Lafayette, Indiana

August 2019

THE PURDUE UNIVERSITY GRADUATE SCHOOL
STATEMENT OF COMMITTEE APPROVAL

Dr. Jeffrey T. Miller, Chair
Davidson School of Chemical Engineering
Dr. Fabio H. Ribeiro
Davidson School of Chemical Engineering
Dr. Rajamani Gounder
Davidson School of Chemical Engineering
Dr. Jeffrey Greeley
Davidson School of Chemical Engineering
Dr. Christina W. Li
Department of Chemistry
Dr. Luis Bollmann
DOW Chemical, Freeport, TX

Approved by:

Dr. John Morgan
Head of the Graduate Program

“I have not failed. I’ve just found 10,000 ways that won’t work.”

- *Thomas Edison*

To my husband, my family and my dog

ACKNOWLEDGMENTS

I am very grateful to Jeff Miller for taking me as his student. During these past few years, I have learned and grown a lot under his guidance. He has taught me not only how to do research, but also how to communicate more effectively and have more self-confidence in myself and my work. He was always very supportive and encouraging towards all of us and have pushed us to succeed after grad school. I'm also very grateful for the endless amounts of chocolates he has provided us in his office.

I am also very grateful to the group members, especially my seniors and previous Jeff Miller's students, Dr. Evan Wegener and Dr. Zhenwei Wu, and our post-doc Dr. Guanghui Zhang. They have both taught me everything about the lab work and EXAFS and XRD analysis, especially Zhenwei who was in the lab with me from day one. Guanghui was a true mentor in my journey as well, always patient and providing insightful discussions more my "quick" and "dumb" questions. I also want to thank the current group members, Nicole Libretto and Johnny Zhu-chen, for all the talks and laughs we had in the office and at Argonne. Especially Nicole, as we have been working together in the oligomerization project.

I'd also like to thank Dr. Luis Bollmann, Dr. Apoorva Kulkarni, Dr. Sandeep Dhingra and everybody in the EOEG and Hydrocarbons groups at DOW, Freeport, TX. They have provided me a unique opportunity with my internship at DOW. I was able to learn a lot about industrial research and Luis, Apoorva and Sandeep were great mentors, who taught me a lot in the short period I was there.

I'd also like to thank Dr Fabio Ribeiro, Dr. Jeff Greeley, Dr. Christina Li and Dr. Rajamani Gounder for being part of my committee during my qualifications and preliminary exams and my final defense. Their questions and discussions were always insightful and helped guide my

research. As for discussions and research learning, I'm also thankful to the whole Purdue Catalysis Group.

Lastly, but even more important, I'm thankful to my friends and family for all the support they have given me. Thank you to Claire Liu, Noelia Almodovar and Seulgi Choi, who made the transition to a new country, where I knew nobody, less stressful and more enjoyable. I'm also thankful to my mother and grandmother for raising me to be the person I am today and all the support thorough those years. Finally, I'm deeply grateful for all the emotional support my husband, Dayvison, my dog, Cookie, and my family have provided me during these past years. My husband was always supportive, from day one in Brazil, and he has always cheered me up when I was feeling down, or the experiments were not working.

TABLE OF CONTENTS

LIST OF TABLES

LIST OF FIGURES

ABSTRACT

Author: Cesar, Laryssa Gonçalves. PhD
Institution: Purdue University
Degree Received: August 2019
Title: Light Alkanes to Higher Molecular Weight Olefins: Catalysts for Propane Dehydrogenation and Ethylene Oligomerization.
Committee Chair: Jeffrey T. Miller

The increase in shale gas exploitation has motivated the studies towards new processes for converting light alkanes into higher valuable chemicals, including fuels. The works in this dissertation focuses on two processes: propane dehydrogenation and ethylene oligomerization. The former involves the conversion of propane into propylene and hydrogen, while the latter converts light alkenes into higher molecular weight products, such as butylene and hexene.

The thesis project focuses on understanding the effect of geometric effects of Pt alloy catalysts for propane dehydrogenation and the methodologies for their characterization. Pt-Co bimetallic catalysts were synthesized with increasing Co loadings, characterized and evaluated for its propane dehydrogenation performance. In-situ synchrotron X-Ray Powder Diffraction (XRD) and X-Ray Absorption (XAS) were used to identify and differentiate between the intermetallic compound phases in the nanoparticle surface and core. Difference spectra between oxidized and reduced catalysts suggested that, despite the increase in Co loading, the catalytic surface remained the same, Pt_3Co in a Au_3Cu structure, while the core became richer in Co, changing from a monometallic Pt fcc core at the lowest Co loading to a PtCo phase in a AuCu structure at the highest loading. Co^{II} single sites were also observed on the surface, due to non-reduced Co species. The catalytic performance towards propane dehydrogenation reinforced this structure, as propylene selectivity was around 96% for all catalysts, albeit the difference in composition. The Turnover Rate (TOR) of these catalysts was also similar to that of monometallic Pt catalysts, around 0.9 s^{-1}, suggesting Pt was the active site, while Co atoms behaved as non-active, despite both atoms being active in their monometallic counterparts.

In the second project, a single site Co^{II} catalyst supported on SiO_2 was evaluated for ethylene oligomerization activity. The catalyst was synthesized, evaluated for propane dehydrogenation, propylene hydrogenation and ethylene oligomerization activities and characterized *in-situ* by XAS and EXAFS and H_2/D_2 exchange experiments. The catalysts have shown negligible conversion at

250ºC for ethylene oligomerization, while a benchmark Ni/SiO_2 catalyst had about 20% conversion and TOR of $2.3x10^{-1}$ s^{-1}. However, as the temperature increased to above 300ºC, ethylene conversion increased significantly, reaching about 98% above 425ºC. *In-situ* XANES and EXAFS characterization suggested that H_2 uptake under pure H_2 increased in about two-fold from 200ºC to 500ºC, due to the loss of coordination of Co-O bonds and formation of Co-H bonds. This was further confirmed by H_2/D_2 experiments with a two-fold increase in HD formation per mole of Co. *In-situ* XAS characterization was also performed with pure C_2H_4 at 200ºC showed a similar trend in Co-O bond loss, suggesting the formation of Co-alkyl, similarly to that of Co-H. The *in-situ* XANES spectra showed that the oxidation state remained stable as a Co^{2+} despite the change in the coordination environment, suggesting that the reactions occurs through a non-redox mechanism. These combined results allowed the proposition of a reaction pathway for dehydrogenation and oligomerization reactions, which undergo a similar reaction intermediate, a Metal-alkyl or Metal-Hydride intermediates, activating C-H bonds at high temperatures.

1. INTRODUCTION

Due to the recent increase in shale gas exploitation and the abundance of its wells in the U.S., new studies have been focusing on the development of new technologies to transform the exploited light paraffins into valuable chemicals[1]. Given that up to 70% of its composition are non-methane light alkanes, i.e., ethane and propane, and due to the stablished technology for ethane conversion, i.e., steam crackers, most studies for new technologies have converged to the propylene production, such as in the propane dehydrogenation process.

These light olefins, ethylene and propylene, are widely used in the industry as feedstock to produce valuable materials, such as polymers and chemical intermediates[2]. One of the most common process for upgrading light olefins is ethylene oligomerization. However, the conditions under which dehydrogenation and steam cracking occur are extremely different from those for ethylene oligomerization. While both steam cracking and dehydrogenation are run at high temperatures, between 500^{o}C to 900^{o}C range, commercial oligomerization reactions occur in a homogeneous process with temperatures below 80^{o}C. A process for upgrading light alkanes into high molecular weight olefins for fuel production can be feasible in a multi-step process with low economical cost if both processes, dehydrogenation and oligomerization, are performed at similar conditions[3]–[5].

1.1 Light Alkane Dehydrogenation

Light alkane dehydrogenation reactions occur due to the C-H bond activation in light alkanes, producing their corresponding olefin and H_2. For example, propane dehydrogenation will cleave the C-H bonds in neighboring Carbon species, producing propylene and H_2. This reaction is highly endothermic and, consequently, requires high reaction temperatures, for example, above

550ºC for propane conversion and above 650ºC for ethane. The entire process is very cost-efficient because the energy required is provided by burning the coke deposits in the catalysts during regeneration [3].

Currently, propane dehydrogenation (PDH) global plants produce more than 5 million tons of propylene annually. The two main processes are the Catofin process, which uses Chromia-Alumina catalysts, and the Oleflex process, using a Pt-Sn catalyst [3] . Although pure Pt is an active catalyst for the dehydrogenation process, it has a low alkene selectivity and a fast deactivation rate due to coke formation [6]. The addition of Sn has shown an increase in the propylene selectivity and lower deactivation rates, albeit these are still high[7]–[11].

Recent studies have investigated new catalysts, such as metals (Co, Ir), oxides (GaO_x, VO_x, MoO_x and InO_x), and bimetallic catalysts (Pt-Fe, PtGa, PtGe, PtSn, PdZn) [3], [12]–[19]. These new catalysts must have several characteristics, such as high olefin selectivity, minimal coke formation, good catalyst activity and a non-acid, high surface area oxide support. To achieve high olefin selectivity, the cleavage of C-H bonds must be favored over the C-C bond cleavage. The latter leads to side reactions, such as hydrogenolysis, producing light alkanes, and coking, blocking the metallic sites and losing activity [3].

Recently, intermetallic alloys have been identified as promising catalysts, mainly Pt and Pd based catalysts. The addition of a second metal to a monometallic catalyst can enhance its performance by changing its electronic or geometric properties. This can lead to higher selectivity towards propylene in a PDH process. For example, according to Childers *et al*, Pd-Zn alloyed catalysts are highly selective towards propylene, while its Pd monometallic catalysts are highly selective towards reactions producing methane and coke [13].

It's believed that this enhanced selectivity is due to the isolation of the active metal. For example, in a Pd-In bimetallic catalysts, an inactive metal, Zn, was used as a non-active promoter for the Pd active sites. Upon formation of an intermetallic compound, the Pd atoms are surrounded by Zn atoms in its crystal cell.

1.2 Ethylene Oligomerization

Oligomerization reactions consist in the formation of longer chain hydrocarbons by the addition of short chain olefins, like ethylene and propylene, producing intermediate molecular weight hydrocarbons[20], [21]. These are building blocks for many industrial process and the synthesis of linear higher weight α-olefins is a key step to produce detergents, plasticizers and even fuels[22].

Light alkene oligomerization processes can be carried out by both homogeneous and heterogeneous catalysts. However, most of industrial processes are dominated by homogeneous transition metal complex catalysts, especially Nickel (Ni) and Chromium (Cr). Nickel-based catalysts are applied in the Shell Higher Olefin Process (SHOP), producing a range of LAOs, from C_4 to C_{20}. The only ethylene trimerization process commercialized occurs through the Phillips Catalysts, composed of a Cr complex catalyst and an alkylating agent, such as $AlEt_3$. An ethylene tetramerization process has also been commercialized by Sasol using a Cr-based catalyst. Other commercial catalysts include a Titanium (Ti) compounds used in the IFP/Sabic Alphabutol Process for ethylene dimerization and a Zirconium (Zr) complex used for C_4 to C_{10} production in the Alpha-SABLIN process[23], [24]. Recent research has also focused on the development of new catalysts containing as iron (Fe) and Cobalt (Co)[25]–[27]

The mechanism of alkene oligomerization with homogeneous catalysts have been widely investigated and the literature suggests the existence of two main possible pathways: the Cossee-Arlman mechanism and the Metallacycle mechanism (Figure 1.1).

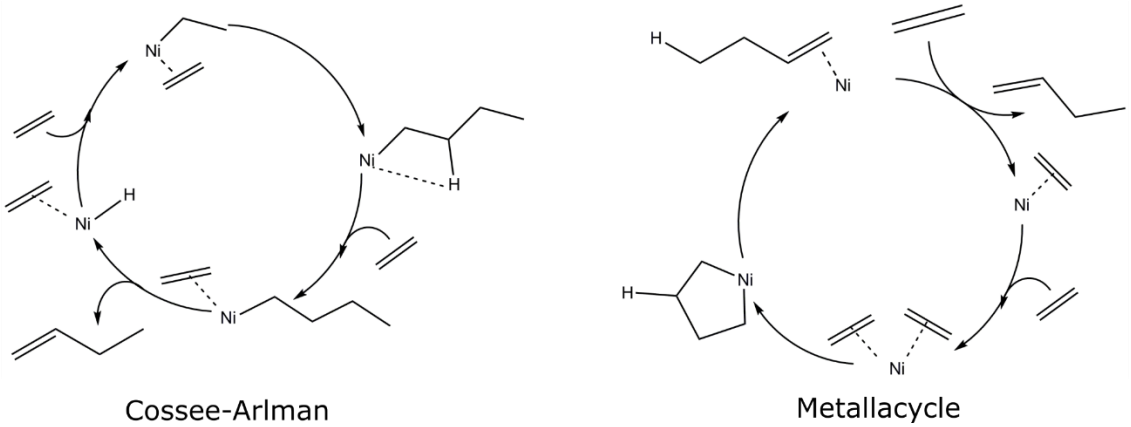

Figure 1.1. Proposed mechanisms for ethylene oligomerization on homogeneous catalysts. On the left, the Cossee-Arlman mechanism; on the right, the metallacycle mechanism.

As illustrated on Figure 1.1, the Cossee-Arlman mechanism was proposed to start with the π-complexation of an ethene molecule on a vacant site in a Ni-Hydride complex. A second ethene molecule is, then, inserted at the Ni-Hydride bond, forming a Ni-alkyl bond. The propagation step starts with the π-coordinated ethene undergoing a migratory insertion reaction to the alkyl radical, creating a neighboring vacancy at the $Ni^{(II)}$ ion. A new ethene molecule can, then, coordinate itself to the Ni atom and the polymer chain can grow through multiple propagation steps[20], [28], [29]. The termination step for this mechanism have been traditionally thought to happen through a β-hydrogen elimination, as shown on Figure 1.1[20], [28]–[30]. Recent calculations in DFT, however, suggests the possibility of Ni-alkyl being the catalytic active species and the termination step occurs through the bond breakage of the rest of the molecule, releasing the oligomer molecule[31]. Due to the propagation mechanism, this mechanism results in a Schulz-Flory

distribution of the products, with a full range of different chain lengths of LAO. This product distribution does not match the market demand, which shows increasingly interest in the lower molecular weight LAOs, such as 1-butene, 1-hexene and 1-octene fractions[26].

To supply the demand for lower molecular weight olefins, homogeneous Ni, Cr, Ti and Zr catalysts that undergo a metallacycle mechanisms have been developed. As shown on Figure 1.1, the mechanism starts with two ethene molecules that coordinate with the Ni^{2+} site through π-complexation bonds, occupying vacant neighboring sites. These ethylene molecules, then, undergo an oxidative coupling producing a metallacyclopentane complex, changing the oxidation state of the metal, i.e. $Ni^{(II)}$ becomes $Ni^{(IV)}$, $Ti^{(II)}$ oxidizes to $Ti^{(IV)}$, etc. Upon the formation of the metallacycle, the propagation steps occur through the insertion of new ethene molecules, producing larger rings. When the ring growth becomes unfavorable, the termination mechanism takes place, which is believed to be through a β-hydrogen elimination, forming a linear α-olefin. Due to geometric constraints, M-C_6 and M-C_8 intermediates have a energetically preference to release the product LAO's, while further ethylene insertion is more energetically favorable for M-C_4 intermediates. Therefore, this type of mechanism tends to produce higher amounts of 1-hexene and 1-octene, hindering 1-butene production [23], [32]–[34].

Both mechanisms are believed to occur for heterogeneous catalysts by extrapolation. However, little evidence has been actually published for the presence of either mechanism and there is still no consensus about either the pathway or the active site nature for heterogeneous Ni catalysts. Recent work published by Delcroix *et al* suggests that the dominant mechanism for these catalysts are the Cossee-Arlman mechanism with the formation of Nickel-Hydrides[35], [36].

Therefore, there has been an increase in the interest for heterogeneous catalysts for oligomerization. Despite the high activity and selectivity of the homogeneous catalysts, a highly

active heterogeneous counterpart would translate in a decrease of the economic costs as well as "greener" process due to an easier separation of products and catalysts and less generation of waste. Most heterogeneous catalysts present in the literature are Ni-based catalysts supported on zeolites, due to both the shape selectivity for products and the presence of acid sites that also catalyze oligomerization reactions[35]–[42]. Some recent studies have also studied heterogeneous Co and Fe based catalysts supported on zeolites and carbon[22].

1.3 Dissertation Overview

The goal of this dissertation is to characterize two catalysts for each of a two-step process of converting light alkanes into higher molecular weight alkenes to be used as fuels and evaluate their catalytic performance. By characterizing the catalysts in-situ at the Advanced Photon Source (APS) at Argonne National Laboratory (ANL), using in-situ X-Ray Absorption Spectroscopy (XAS) and Powder X-Ray Diffraction (XRD), it's possible to understand the catalysts' structural properties and their correlation to catalytic performance. This fundamental understanding can lead to the development of better materials for this complex process. This work will focus on the methodologies used to characterize these catalysts.

In chapter 2, a Pt-Co bimetallic catalyst was synthesized, characterized and evaluated for its propane dehydrogenation performance. In-situ synchrotron X-Ray Powder Diffraction (XRD) and X-Ray Absorption (XAS) were used to identify the intermetallic compounds phases that constituted the nanoparticle and to differentiate between surface and core structures. The surface differentiation was possible due to the comparison between the ratios of Pt-Co and Pt-Pt bonds on each catalyst using difference spectra in Extended X-Ray Absorption (EXAFS) between the oxidized and fully reduced catalysts. As the Cobalt loading in these catalysts increased, the surface remained the same, as a Pt_3Co intermetallic surface, while the nanoparticle core became richer in

Cobalt species. The surface was further probed by propane dehydrogenation reaction. Given the same surface was present in all catalysts, their selectivity towards propylene formation was about the same, around 96%, and the Turnover Rate (TOR) was within the same order of magnitude as that of monometallic Pt catalysts. Thus, the selectivity not only improved due to the geometric effects due to the isolated Pt sites on the surface, i.e., Pt_3Co structure, but Pt also behaved as the only active site, while Co atoms behaved as non-active, despite both atoms being active in their monometallic counterparts.

In chapter 3, a single site Cobalt catalyst supported on silica was evaluated for ethylene oligomerization at high temperature. Due to commercial catalysts being homogenous and the high intrinsic activity of Nickel catalysts, the usual conditions for ethylene oligomerization in the literature are high pressures and low temperatures, between 50^{o}C to 200^{o}C. At these low temperatures, silica supported Co single sites catalysts were not active and negligible conversions were achieved at 250^{o}C. However, due to its thermal stability at high temperatures and activity towards propane dehydrogenation at 550^{o}C, these catalysts were evaluated at higher temperatures under 500 psi of C_2H_4. As the temperature increased above 300^{o}C, the ethylene conversion also increased significantly, and higher molecular weight products were observed, i.e., above C_6. In-situ Near Edge X-Ray spectra (XANES) and Extended X-Ray Fine Structure Spectra (EXAFS) suggested that Co-H species greatly increased from 200^{o}C to 550^{o}C in the presence of pure H_2. Likewise, these methods suggested the formation of Co-alkyl intermediated at 200^{o}C, albeit low coverage. This suggested that high temperatures favor the formation of Co-H and Co-alkyl intermediated. These spectra also showed no change in the oxidation state and, thus, a non-redox mechanism. A reaction pathway was proposed for ethylene oligomerization, sharing a common intermediate, Co-H, with dehydrogenation and hydrogenation reactions.

2. IDENTIFICATION OF A Pt_3Co SURFACE INTERMETALLIC ALLOY IN PT-CO PROPANE DEHYDROGENATION CATALYSTS

Cesar, L.G.; Yang, C.; Lu, Z.; Ren, Y.; Zhang, G.; Miller, J.T; "Identification of a Pt_3Co Surface Intermetallic Alloy in Pt–Co Propane Dehydrogenation Catalysts". ACS Catal., 2019, 9, 65231-5244. Reprinted with permission from *ACS Catal*.

2.1 Abstract

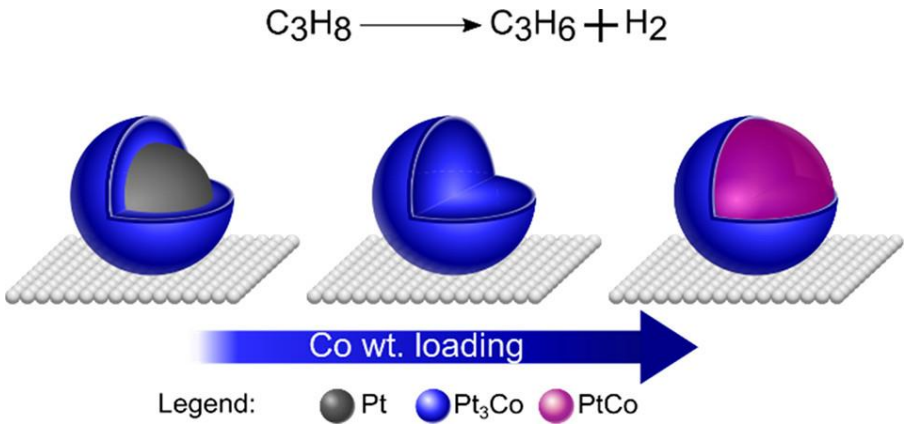

Figure 2.1. Scheme for the Alloy formation of Pt-Co nanoparticles structure formation. Reprinted with permission from ACS Catal., 2019, 9, 6, 5231-5244[43]. Copyright 2019 American Chemical Society.

Bimetallic Pt–Co nanoparticles (NPs) were prepared and characterized by scanning transmission electron microscopy, in situ X-ray absorption spectroscopy, in situ synchrotron X-ray diffraction, and catalytic conversion for propane dehydrogenation with and without added H2. In addition, the surface extended X-ray absorption fine structure (EXAFS) obtained by fitting the difference spectrum between the fully reduced and room-temperature-oxidized catalysts suggest that the surface structure remains Pt_3Co, although the core changes from Pt to Pt3Co and to PtCo. At low Co loading, the bimetallic nanoparticles form a Pt3Co intermetallic surface alloy with Pt-rich core. With increasing Co loading, a full alloy forms where both the surface and NP

compositions are Pt_3Co. A further increase in Co loading leads to a Co-rich NP core, likely PtCo, with a surface of Pt_3Co. Although Pt–Co intermetallic alloys form two different phases and several morphologies, the surface structures are similar in all catalysts. Although both monometallic Pt and Co are active for alkane dehydrogenation, all bimetallic Pt–Co catalysts are significantly more olefin selective than either single metal. The turnover rates of the bimetallic catalysts indicate that Pt is the active atom with little contribution from Co atoms. The high olefin selectivity is suggested to be due to Co acting as a less active structural promoter to break up large Pt ensembles in bimetallic NPs.

2.2 Introduction

In heterogeneous catalysts, chemical reactions occur at the interface between the gas-phase reactants and surface atoms. The reaction mechanisms happen through multiple steps involving reactants adsorption, adsorbates' reaction and the product desorption. The surface structure is, therefore, responsible for determining these reaction pathways, as it determines not only the reaction rates but also the selectivity towards certain products.

One important example is propane dehydrogenation, where C-H bonds (Reaction I) are broken to form propylene. Since this reaction is highly endothermic, it requires high temperatures which also favor light gas formation by hydrogenolysis and rapid deactivation by coke formation. Hydrogenolysis reactions are due to C-C bonds dissociation (Reaction II) in presence of H_2, while the coke formation on the surface rapidly deactivates the catalysts by active sites blockage. Active catalysts for propane dehydrogenation process are those of group VIII metals such as Pt, Pd, Co and Fe[44]. Among these, Pt shows the highest activity, at temperatures as low as 500ºC, and the best olefin selectivity due to its superior ability to favor Reaction I over Reaction II. However, its reported olefin selectivity is still low, typically about 60% to 80%[45]–[48].

$C_3H_8 \leftrightarrow C_3H_6 + H_2$ [I]

$C_3H_8 + H_2 \leftrightarrow C_2H_6 + CH_4$ [II]

Reduction of hydrogenolysis rate improves propylene selectivity and can be achieved by adding non-active, post transition metals as promoters forming bimetallic Pt catalysts. Sn is the most common promoter, being commercially available, with reported selectivity ranging from 74% to 96%[7], [8], [47]–[52]. Reported catalysts for light alkane dehydrogenation often contain Pd or Pt as the active metal and a second metal as a promoter, such as Pd-Zn, Pt-Ga, Pt-Ge, Pt-Pb, Pt-Cu, Pd-In, Pt-In, and Pt-Sb, with initial selectivity above 90% [12]–[14], [16], [18], [19], [53]–[55]. This increase in selectivity can be attributed to the inhibition of hydrogenolysis and coke formation. According to Boudart, catalyzed reactions can be classified as structure sensitive and structure insensitive[56], [57]. Hydrogenolysis, being an example of the former, is affected by the surface ensemble size; while dehydrogenation is a structure insensitive reaction where all surface Pt atoms are active[58]–[60]. The addition of a non-catalytic promoter acts by decreasing the surface Pt ensemble size, responsible for hydrogenolysis. The high selectivity of bimetallic Pt NP's is, therefore, linked to the geometric effect caused by the non-catalytic promoter[13], [45]. Bimetallic NP's can form either a solid solution (disordered structure) or an intermetallic compound (ordered structure). Common ordered alloy phases are Pt_3M[18] and PtM[13], [19], with Au_3Cu and AuCu structures, respectively, as shown on Figure 2.2. Both structures have fewer Pt-Pt neighbors, resulting in small Pt ensembles or isolated Pt atoms.

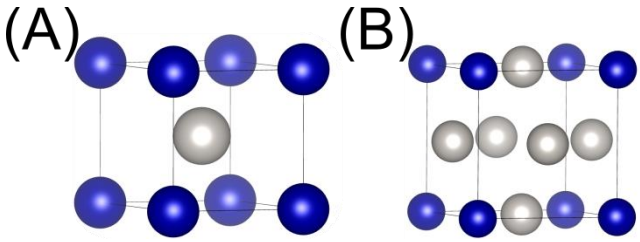

Figure 2.2. Schematics for (a) a PtM (AuCu type) and (b) a Pt_3M (Au_3Cu) alloy phase structures. The Pt atoms are represented in grey and promoter atoms in blue. Reprinted with permission from *ACS Catal.*, 2019, 9, 6, 5231-5244[43]. Copyright 2019 American Chemical Society.

In addition to single phase bimetallic and alloy phases, the nanoparticles can also form two phases: for example, a bimetallic shell with a monometallic Pt core[17], [18], [61]. In such cases, it's crucial to determine the surface composition to understand the reaction selectivity. However, in small nanoparticles (<2 nm), this can be challenging due to the limitations of traditional surface analysis methods, especially when two phases are present.

Cobalt forms two ordered intermetallic compounds with Pt, Pt_3Co and PtCo[62]. Given that Co is also a VIII group metal, it is also active for propane dehydrogenation, but exhibits a poor selectivity and rapid deactivation compared to Pt[44]. Therefore, it might be expected that promoting Pt with Co might result in a catalyst with poor selectivity and stability from the Pt-Co ensembles. Additionally, PtCo alloys have been reported to improve activity in electrocatalysts, but careful characterization to differentiate solid solutions and intermetallic compounds have not been performed[63], [64].

The goal of this work is to synthesize and investigate the surface structure of bimetallic Pt-Co catalysts for propane dehydrogenation where two intermetallic compounds are formed, PtCo and Pt_3Co. The catalysts were prepared and their catalytic performance for propane dehydrogenation was determined. Additionally, their structures were determined by in situ, X-ray

absorption spectroscopy (XAS), synchrotron X-ray diffraction, (XRD) and surface extend X-ray absorption fine structure (EXAFS) analysis.

2.3 Experimental Section

2.3.1 Catalyst Synthesis

A series of catalysts were synthesized using a fixed amount of Pt (2 wt.%) with varying weight loading of Co: 2wt.%Pt-0.6 wt.%Co (2Pt0.6Co), 2 wt.%Pt-1 wt.%Co (2Pt1Co), 2 wt.%Pt-2 wt.%Co (2Pt2Co) and 2 wt.%Pt-4 wt.%Co (2Pt4Co). Monometallic Pt and Co catalysts were also prepared for comparison. All catalysts were supported on SiO_2 (Davisil 636 silica gel, Sigma–Aldrich, 35-60 mesh, surface area = 480 m^2/g, pore volume = 0.75 cm^3/g).

For the monometallic catalysts, a 3 wt.% Pt ($3Pt/SiO_2$) and a 10 wt.% Co ($10Co/SiO_2$) catalyst were prepared by Incipient Wetness Impregnation (IWI); while a 2wt%, single-site $Co^{(II)}/SiO_2$ was prepared by Strong Electrostatic Adsorption (SEA)[65].

For the 3 wt.% Pt catalyst, the precursor solution was prepared by dissolving 0.3 g of tetraamineplatinum(II) nitrate ($Pt(NH_3)_4(NO_3)_2$, Sigma Aldrich) in 5 mL solution of deionized water and NH_4OH. The NH_4OH was added for pH correction to about 11. This solution was, then, added dropwise to 5 g of dry SiO_2, until the SiO_2 was moist to avoid over-impregnation of the pores. This method is called charge enhanced dry impregnation (CEDI)[65]. The impregnated SiO_2 was, then, dried overnight at 125ºC, followed by calcination at 350ºC for 3 hours. The reduction step was performed under 5% H_2/N_2 atmosphere at 250ºC for 30 min, followed by 600ºC for another 30 minutes.

Similarly, the metallic Co/SiO_2 was prepared by two sequential impregnations of cobalt$^{(II)}$ nitrate hexahydrate ($Co(NO_3)_2 \cdot 6H_2O$, Sigma Aldrich). Initially, 3.7 g of cobalt nitrate was dissolved in 15 mL of deionized water and the solution was mixed to 15 g of dry SiO_2 by dropwise

addition. This yielded a total 5 wt.% Co loading to the catalyst. During this preparation, the pH was not adjusted with NH_4OH to avoid precipitation of the precursor. After impregnation, the catalyst was dried overnight at 125ºC, followed by calcination at 400ºC for 3 hours. The calcined catalyst went through a second impregnation using the same amount of precursor solution and same conditions for drying and calcination steps. To fully reduce the Co precursor, the catalyst was reduced in 5% H_2/N_2 at 750ºC for 30 min.

For the single site $Co^{(II)}/SiO_2$, the synthesis occurred through strong electrostatic absorption (SEA) with hexamine cobalt (III) chloride ($Co(NH_3)_6Cl_3$ – Sigma-Aldrich) as a precursor, as described by Hu et al[66]. The precursor solution was prepared by dissolving 1.7 g of $Co(NH_3)_6Cl_3$ in about 50 mL of deionized water and NH_4OH, to adjust the pH to 11. Simultaneously, 15 g of SiO_2 was suspended in 50 mL of H_2O in a separate beaker, also correcting the pH to 11 by NH_4OH. This pH deprotonates the surface SiOH and results in a negatively charged surface, allowing the metal cations to be strongly adsorbed to the support. The precursor solution was mixed with the SiO_2 and stirred for 20 minutes to allow the adsorption and saturation of the metal cation on the support surface. After the SiO_2 settled, the solids were separated by decantation and triple rinsed with deionized water and vacuum filtered. The filtered solids were dried first at room temperature (RT) and then at 125ºC, both for overnight periods. Lastly, the catalyst was calcined at 400ºC for 3 hours.

For the lowest Co loading, 2Pt0.6Co, the chosen method was also CEDI. The precursors solution was prepared for a total volume of 4.5 mL, containing 0.2 g of $Pt(NH_3)_4(NO_3)_2$ and 0.136 g of $Co(NH_3)_6Cl_3$, with pH correction to 11 with NH_4OH. This solution was added dropwise to 5 g of dry SiO_2, the resulting catalysts were sequentially dried at RT and 125ºC, for overnight periods, and then calcined at 225ºC for 3 hours.

For the 2Pt1Co on SiO_2, a precursor solution of 1 wt.% Co was initially prepared for SEA, similarly to the $Co^{(II)}$ single site method. A 15 mL solution containing 0.227g of $Co(NH_3)_6Cl_3$ was added to 5.0 g of SiO_2 suspension in 25 mL of water, both at pH 11, and stirred for 20 minutes. After the solids settled, they were triple rinsed, vacuum filtered, dried at RT and 125ºC for overnight periods and calcined at 400ºC for 3 hours. The resulting solid had 1wt.% Co loading and it was then impregnated (CEDI) with a 4.5 mL of precursor Pt solution at a pH of 11 with NH_4OH, containing 0.2 g of $Pt(NH_3)_4(NO_3)_2$ by dropwise addition. This resulting solid was dried as described previously and calcined at 225ºC for 3 hours.

The procedure for the 2Pt2Co/SiO_2 catalyst was the same as described for 2Pt1Co, via initial SEA and followed by IWI with Pt. The precursor solution for SEA contained 0.567g of $Co(NH_3)_6Cl_3$ for the same 15mL volume to reach a 2wt.%Co loading on the catalyst. The precursor solution for IWI contained the same amount of Pt. The synthesis, drying and calcination procedure were performed as described above.

For 2Pt4Co, the initial step was also SEA to produce an initial 3wt.%Co/SiO_2 catalyst. A 25 mL of precursor solution was prepared with 1.114 g of $Co(NH_3)_6Cl_3$ and it was stirred to 5.0 g of suspended SiO_2 in 25 mL of deionized water for 20 minutes, with the system kept at pH 11. Similar to the previous catalysts, the solids were rinsed, vacuum filtered, dried and calcined at 400ºC for 3 hours. The resulting catalyst was then impregnated with a Pt and Co precursor solution (CEDI) by dropwise addition. This solution contained 0.2 g of $Pt(NH_3)_4(NO_3)_2$ and 0.227 g of $Co(NH_3)_6Cl_3$ with pH adjusted to 11, with a total volume of 5 mL. The catalysts were then dried as described before and calcined at 225ºC for 3 hours.

After the last calcination, all the bimetallic catalysts were reduced in flowing 5%H_2 in balance N_2 sequentially at 250ºC and at 600ºC, both for 30 min.

2.3.2 Scanning Transmission Electron Microscopy (STEM)

STEM images were obtained at Argonne National Laboratory (ANL) to measure the particle size distribution. The images were analyzed using ImageJ software[67]. Depending on the catalysts, about 5 to 10 micrographs were taken at different places on the SiO_2 surface. In each image, it was possible to count about 50 to 100 particles. Therefore, the particle size distribution was determined using a sample space consisting of 100 to 300 particles for accurate determination of the mean particle size of the bimetallic catalysts.

2.3.3 Synchrotron X-Ray Absorption Spectroscopy (XAS)

The X-ray Absorption Spectroscopy (XAS) characterization was carried out in the 10-BM bending magnet and 10-ID Insertion device beamlines, at the Advanced Photon Source facility at Argonne National Laboratory. The monochromator was calibrated by acquiring a metal foil spectrum at each absorption edge. A simultaneous measurement of the metal foil in a third chamber was performed for each catalyst for energy calibration. The spectra were obtained *in situ* in transmission mode for the Pt L_{III} edge and Co K edge in step scan mode in approximately 10 minutes. Before each measurement, the samples were reduced at 550ºC for 30 minutes under a 100 cm^3/min flow rate of 3.5%H_2 in balance He. The XAS cell was purged in He and the measurements were taken at room temperature in presence of He. He was purified with an Oxytrap to prevent oxidation of the reduced catalysts by trace O_2.

All the acquired XAS Data was fit using the WINXAS 3.1 software[68]. The EXAFS coordination parameters can be obtained by fitting the Fourier Transform. The k^2-weighted Fourier transform magnitudes were fit for the coordination shell for the corresponding k-space from ΔK=2.6-12.1 $Å^{-2}$ by the least-squares methods. The first shell was fit (magnitude and imaginary parts) from R=1.6 to 3.0 Å. The Pt-Pt and Co-Co experimental phase and amplitude were

determined from the Pt (12 Pt-Pt at 2.77 Å) and Co (12 Co-Co at 2.51 Å) foils, respectively. Pt-Co phase and amplitude were determined with FEFF 6.0[69].

Additional experiments were performed at the Pt L_{III} edge for surface characterization in each bimetallic Pt-Co catalyst. After full reduction and data collection of the reduced catalysts, the catalysts were oxidized by air at room temperature for 30 minutes. A second scan was obtained on the surface oxidized catalyst. To quantify the fraction of surface Pt, the XAS spectra was analyzed for both XANES and EXAFS. For the XANES, the oxidized spectra were fit through a linear combination between the fully reduced catalyst and a reference PtO spectra, i.e., fully oxidized $Pt^{(II)}$ prepared from oxidation of a 1 nm Pt/SiO_2 catalyst (the EXAFS contained 4 Pt-O bonds at 2.04 Å with no detectable Pt-Pt bonds). For the EXAFS determination of the surface Pt and Co composition, a difference spectra analysis was performed. The chi spectra for the oxidized catalyst was subtracted from the fully reduced catalyst. The result was a difference spectrum that represents the metal peaks (with a normal phase shift) at the catalyst surface. In addition, the difference spectrum has a negative a Pt-O peak, i.e., the phase is π radius out of phase compared to a standard Pt-O scattering pair. The surface Pt fraction can be obtained from the surface Pt-O CN. Fully oxidized PtO has a Pt-O coordination number equal to 4, therefore, the surface Pt-O CN/4 is equal to the fraction of surface Pt, i.e., the Pt dispersion.

2.3.4 Synchrotron X-Ray Diffraction (XRD)

The XRD measurements were performed at the 11-ID-C beamline at Advanced Photon Source at Argonne National Laboratory. This high flux beamline provided high-energy X-rays at 105.70 keV (λ = 0.1173 Å) and a PerkinElmer large area detector.

Two *in situ* measurements were performed. The first diffraction pattern was collected after the samples were reduced at 600ºC, under a flow of 3.5%H_2 in balance He. The second

measurement was taken post-reduction at room temperature under the same 3.5%H_2 in balance He flowrate. Additional measurements of the empty cell and the SiO_2 support were taken under the same conditions for background subtraction.

The data was treated by using two software: Fit2D[70] and Materials Analysis Using Diffraction (MAUD)[71]. The Fit2D program was used to calibrate and integrate the diffraction patterns, generating the 1D diffraction pattern of the intensity *versus* 2θ degrees. MAUD was used to simulate the diffraction patterns of the alloy phases from the literature structures. The alloy phase for each sample was determined by comparing the experimental and calculated patterns. For the monometallic catalysts, Pt and Co, the particle size could be estimated through Scherrer Equation's calculation, where the full width at half maximum (FWHM) of the largest peaks were measured.

2.3.5 Catalyst Evaluation for Propane Dehydrogenation

An appropriate amount of monometallic Pt/SiO_2 or the bimetallic Pt-Co/SiO_2 was mixed with SiO_2, totaling 1.0 g of catalyst bed, was loaded into a ½' O.D. quartz plug flow reactor, secured by quartz wool plugs. Each catalyst was reduced for 60 min in 5% H_2/N_2 at 50 cm^3/min at 550ºC before each test. Due to different activities between the catalysts, the amount of each Pt-Co/SiO_2 varied between 0.0105 g to 0.0700 g. Different amount of catalysts were evaluated for initial conversions and selectivities (zero time on stream), corresponding to minimum catalyst deactivation. The gas products were detected by a gas chromatograph (GC), Agilent 6890, coupled to a FID detector. In a non-oxidative propane dehydrogenation reaction, only light hydrocarbons are detected: methane, ethane, ethylene, propane and propylene. The conversion (X) was calculated by the propane molar difference between the inlet and outlet, while the propylene selectivity (S) was calculated based on the gas product distribution. The formulas are shown below.

$$X=\frac{\text{moles of propane in inlet-moles of propane in outlet}}{\text{moles of propane in inlet}}*100\%$$

$$S=\frac{\text{moles of } C_3H_6}{\text{moles of } C_3H_6+\frac{2*\text{moles of } C_2}{3}+\frac{\text{moles of } CH_4}{3}}*100\%$$

Two experimental conditions were tested: with and without cofeeding H_2. For the first screening, the total flow rate was 200 cm^3/min, with 2.5% C_3H_8 in balance N_2. For the H_2 cofeeding the total flowrate was 250cm^3/min, with 2.0% C_3H_8 and 1.0% H_2 in balance N_2. Both experiments were at 550ºC and atmospheric pressure. Each run was performed for 45 minutes, with data points analyzed every 5 minutes. Due to coke formation, part of converted propane stays in the surface, blocking some active sites and deactivating the catalysts. Thus, the initial conversion and selectivity were determined by extrapolation to zero deactivation at time t=0 min, to minimize the effects of coke formation and to assume a clean surface for the catalysts for TOR estimations. The initial conversions were between 5 and 35%.

The monometallic Co/SiO_2 and single site $Co^{(II)}/SiO_2$ were also tested. However, due to the very rapid deactivation and lower rates compared to the bimetallic Pt-Co, lower flow rates and larger amounts of catalysts were used.

2.4 Results

2.4.1 Scanning Transmission Electron Microscopy

The nanoparticle size was determined by STEM. For an accurate representation, several images were taken at different spots on the SiO_2 surface and the mean particle size and deviation were obtained based on the frequency distribution between 200 and 400 nanoparticles for each

catalyst. Table 2.1 summarizes these results, and the 2Pt1Co and 2Pt4Co catalysts are shown in Figure 2.3 and Figure 2.4, respectively.

Table 2.1. Particle Size Distribution of the nanoparticles. Reprinted with permission from *ACS Catal.*, 2019, 9, 6, 5231-5244[43]. Copyright 2019 American Chemical Society.

Sample	Mean Particle Size (nm)	Standard Deviation (nm)
3Pt	2.3	0.6
10Co	12.4	4.6
2Pt0.6Co	1.3	0.1
2Pt1Co	1.6	0.4
2Pt2Co	1.8	0.1
2Pt4Co	1.4	0.4

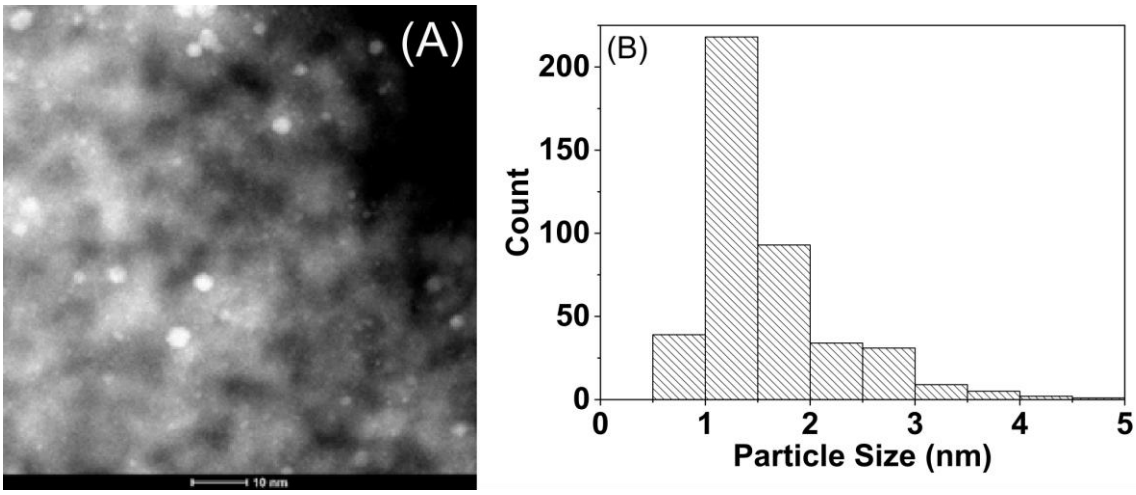

Figure 2.3. STEM images for (a) 2Pt1Co (left) and its respective (b) particle size distribution (right). Reprinted with permission from *ACS Catal.*, 2019, 9, 6, 5231-5244[43]. Copyright 2019 American Chemical Society.

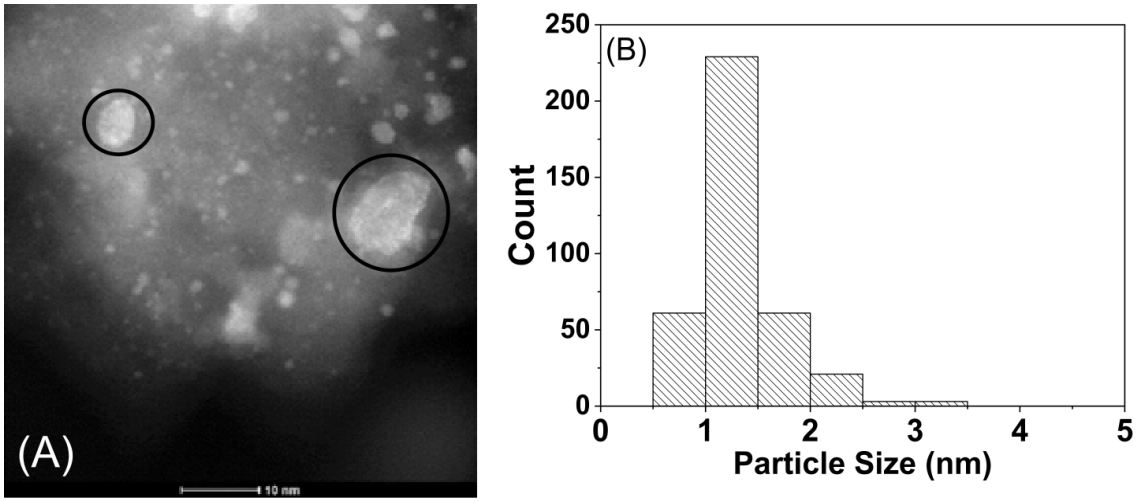

Figure 2.4. STEM images for (a) 2Pt4Co (left) and its respective (b) particle size distribution (right). Large nanoparticles, likely monometallic Co, are circled in black. Reprinted with permission from *ACS Catal.*, 2019, 9, 6, 5231-5244[43]. Copyright 2019 American Chemical Society.

The metallic Pt nanoparticles were found to be around 2.3 nm, while the 10Co nanoparticles were significantly larger, around 12 nm. For all the bimetallic catalysts, the mean particle size distributions are similar, around 1.5 nm with few larger particles. The particles are also well distributed over the SiO_2 surface. At higher Co loading, 2Pt4Co, large nanoparticles of 10 to 20 nm are present, circled in black in Figure 2.4, along with well dispersed small particles. It will be shown later by XRD that the former are likely monometallic Co. Single site $Co^{(II)}/SiO_2$ showed no evidence of metallic Co or oxide NP's.

2.4.2 X-Ray Absorption Spectroscopy (XAS)

2.4.2.1 Pt L_{III} Edge

The XAS measurements for the bimetallic catalysts were performed both at the Pt L_{III} edge (11.564 keV) and Co K edge (7.709 keV). All measurements were taken at room temperature under He atmosphere after reduction at 550ºC. The XANES spectra provide information regarding the oxidation state while the EXAFS identifies the local coordination environment, such as bond

distance and coordination number. The XANES spectra at the Pt L_{III} edge for the monometallic Pt and the bimetallic Pt-Co catalysts are shown in Figure 2.5. The monometallic Pt nanoparticles (NP) have a similar shape, white line intensity and edge energy (11.5640 keV) to those of a Pt foil (Table 2.2). The similarity to both the Pt foil and edge energy suggests that all the Pt atoms in this catalyst are fully reduced, with Pt atoms surrounded only by other Pt atom neighbors.

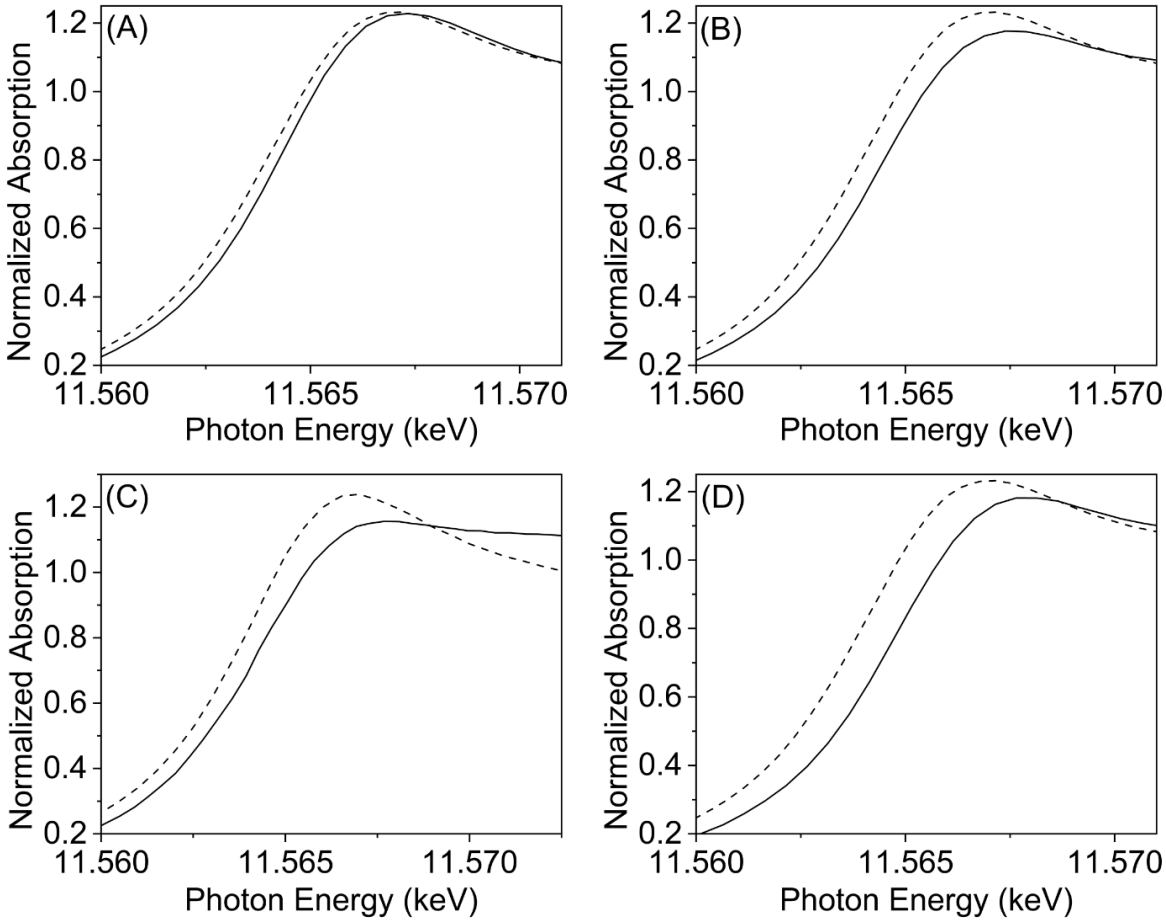

Figure 2.5. Comparison of the XANES Spectra at the Pt L_{III} edge of $3Pt/SiO_2$ (dashed line in all the figures) with (a) 2Pt0.6Co (solid line) in the upper left, (b) 2Pt1Co (solid line) in the upper right, (c) 2Pt2Co (solid line) in the bottom left and (d) 2Pt4Co (solid line) on the bottom right. Reprinted with permission from *ACS Catal.*, 2019, 9, 6, 5231-5244[43]. Copyright 2019 American Chemical Society.

The 2Pt0.6Co spectra shows a similar shape and white line intensity as the Pt NP's, with a slight shift to higher energy, implying that all the Pt atoms are fully reduced and the coordination environment are mainly neighboring Pt atoms. However, the slight decrease and broadening in the white line and the shift to higher edge energy, 11.5642 keV (Table 2.2), suggests the presence of Co atoms. In the 2Pt1Co spectrum, there is also a decrease in the white line intensity and a shift to higher edge energy. Its edge energy, 11.5647 keV (Table 2.2) is larger than that in 2Pt0.6Co, also suggesting higher levels of Co within the Pt bonding distance. The Pt XANES spectrum of 2Pt2Co further decreases in the white line intensity and shifts to higher edge energy, 11.5644 keV. Similarly, the 2Pt4Co XANES spectrum shifts even further (Table 2.2), indicative of bimetallic particles with an increasing Co composition.

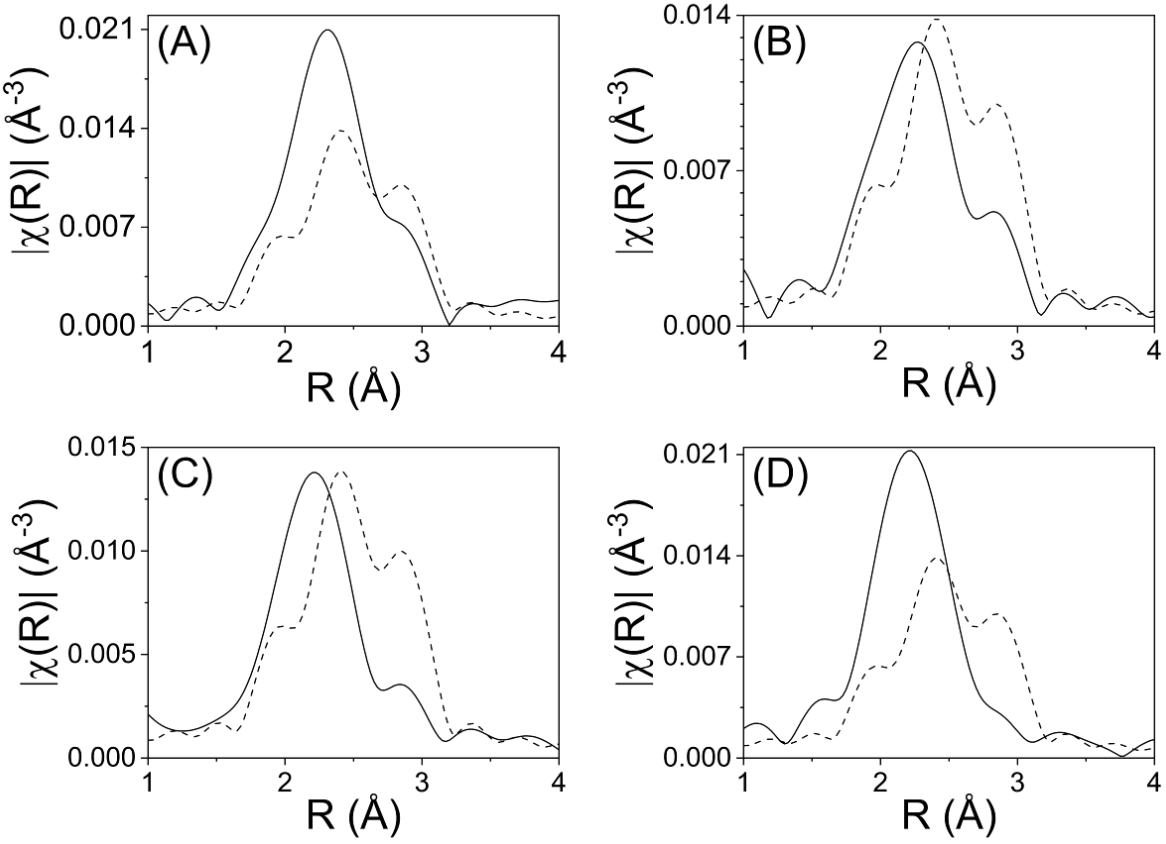

Figure 2.6. Comparison of EXAFS of $3Pt/SiO_2$ (dashed line) at Pt L_{III} Edge with (a) 2Pt0.6Co (solid line) in the upper left, (b) 2Pt1Co (solid line) in the upper right, (c) 2Pt2Co (solid line) in the bottom left and (d) 2Pt4Co on the bottom (solid line) in the bottom right. Reprinted with permission from *ACS Catal.*, 2019, 9, 6, 5231-5244[43]. Copyright 2019 American Chemical Society.

The k²-weighted magnitude of the Fourier Transform (FT) of the EXAFS spectra at the Pt L_{III} edge show different shapes between the four bimetallic particles and Pt (Figure 2.6). The imaginary parts of the FT (not shown) are also different for each catalyst. As shown in the monometallic Pt nanoparticle in Figure 2.6, Pt-Pt bonds show three peaks between 2 and 3 Å (phase uncorrected distance), where the center peak is the largest and the first peak is the smallest. By using the experimental phase and amplitude calculated for a Pt foil, the Pt/SiO_2 catalyst was fit. The Pt-Pt coordination number (CN) was 9.3 at 2.75 Å (Table 2.2). In a Pt foil, the Pt-Pt bond

CN is 12 at 2.77 Å distance. These slightly shorter Pt-Pt bond distance are consistent with small Pt nanoparticles[72].

Table 2.2. EXAFS data at the Pt L_{III} edge for the fully reduced bimetallic Pt-Co and monometallic Pt catalysts. Reprinted with permission from *ACS Catal.*, 2019, 9, 6, 5231-5244[43]. Copyright 2019 American Chemical Society.

Sample	Edge Energy (keV)	Bond	Bond Length (Å)	CN	(Pt-Co):(Pt-Pt) ratio	σ^2	E_0 shift (keV)
3Pt	11.5640	Pt-Pt	2.75	9.3	0	0.002	-1.1
2Pt0.6Co	11.5642	Pt-Pt	2.73	7.8	0.32	0.002	0.22
		Pt-Co	2.56	2.5		0.002	-1.89
2Pt1Co	11.5647	Pt-Pt	2.73	4.5	0.49	0.002	-1.31
		Pt-Co	2.56	2.2		0.002	1.05
2Pt2Co	11.5644	Pt-Pt	2.73	3.0	0.97	0.002	-2.21
		Pt-Co	2.56	2.9		0.002	3.23
2Pt4Co	11.5645	Pt-Pt	2.73	2.5	2.08	0.002	-3.48
		Pt-Co	2.56	5.2		0.002	4.64

The shape of the EXAFS spectrum of 2Pt0.6Co particles is strongly distorted compared to monometallic Pt, Figure 5a. The central peak is shifted to lower R and the first and second peaks overlap. The third peak decreased sharply in intensity. The EXAFS was fit with experimental Pt-Pt reference and FEFF6 simulated Pt-Co scattering pair. Good fits were obtained with a Pt-Pt bond length of 2.73 Å, with a CN of 7.9 and Pt-Co bond length of 2.56 Å with 2.5 CN. The EXAFS is consistent with the XANES and confirms the formation of bimetallic Pt-Co NP's. The higher Pt-Pt CN indicates these particles are Pt-rich.

In the 2Pt1Co spectrum (Figure 2.6b), the central peak shifts to an even lower R, overlapping with the first peak. The third (high R) peak is still present, but at a significantly lower height. A

fit of the EXAFS gives a Pt-Pt CN of 4.5 at 2.73 Å and a Pt-Co CN of 2.2 at 2.56 Å (Table 2.2). The bimetallic NP's are also Pt rich but contain more Co than in the 2Pt0.6Co, consistent with the larger shift in the XANES energy. The (Pt-Co):(Pt-Pt) CN ratio is about 1:2 in the reduced catalyst.

The 2Pt2Co catalyst spectrum, as shown in Figure 2.6c and Table 2.2, has a similar shape to that of 2Pt1Co, with the first and central peak overlapping but with an even lower height third peak. The fit has a Pt-Pt CN of 3.0 at 2.73 Å and a Pt-Co CN of 2.9 at 2.56 Å. The ratio of (Pt-Co):(Pt-Pt) CN ratio was about 1:1. Thus, these bimetallic NP's contain about equal amounts of Pt and Co, and an increased Co composition compared to 2Pt1Co.

In the 2Pt4Co spectrum, only one large peak shifted to low R is present. Due to the large number of Pt-Co bonds, it is difficult to quantify the Pt-Pt CN in the first shell. As a result the Pt-Pt bond distance for the shell was fixed at 2.73 Å similar to those in the other catalysts. The resulting Pt-Co bond distance is 2.55 Å with a CN of 5.2, while Pt-Pt has a CN of 2.5 at 2.73 Å (Table 2.2). The (Pt-Co):(Pt-Pt) CN ratio was approximately 2:1. These NP's have the highest Co content of the four bimetallic catalysts.

The Pt L_{III} EXAFS show the same trends observed with the XANES spectra. As the Co metallic loading increases, bimetallic particles are formed with increasing amounts of Co in the metallic NPs.

2.4.2.2 Co K edge

The XANES spectra at the Co K edge of the bimetallic Pt-Co, monometallic Co and single site $Co^{(II)}/SiO_2$ catalysts are shown in Figure 2.7. The shape of the spectra and the edge energy of the monometallic $10Co/SiO_2$ (7.709 keV) is similar to the Co foil (Figure 6A-D, dotted, Table 2.2), suggesting that $10Co/SiO_2$ is fully reduced, i.e. a Co^0 oxidation state

The XANES spectra for the $2Co^{(II)}/SiO_2$ (Figure 6A-D, dashed) on the other hand, shows a large white line intensity, as well as a higher XANES edge energy. The pre-edge peak at 7.7085 keV is consistent a Co^{2+} oxidation state.

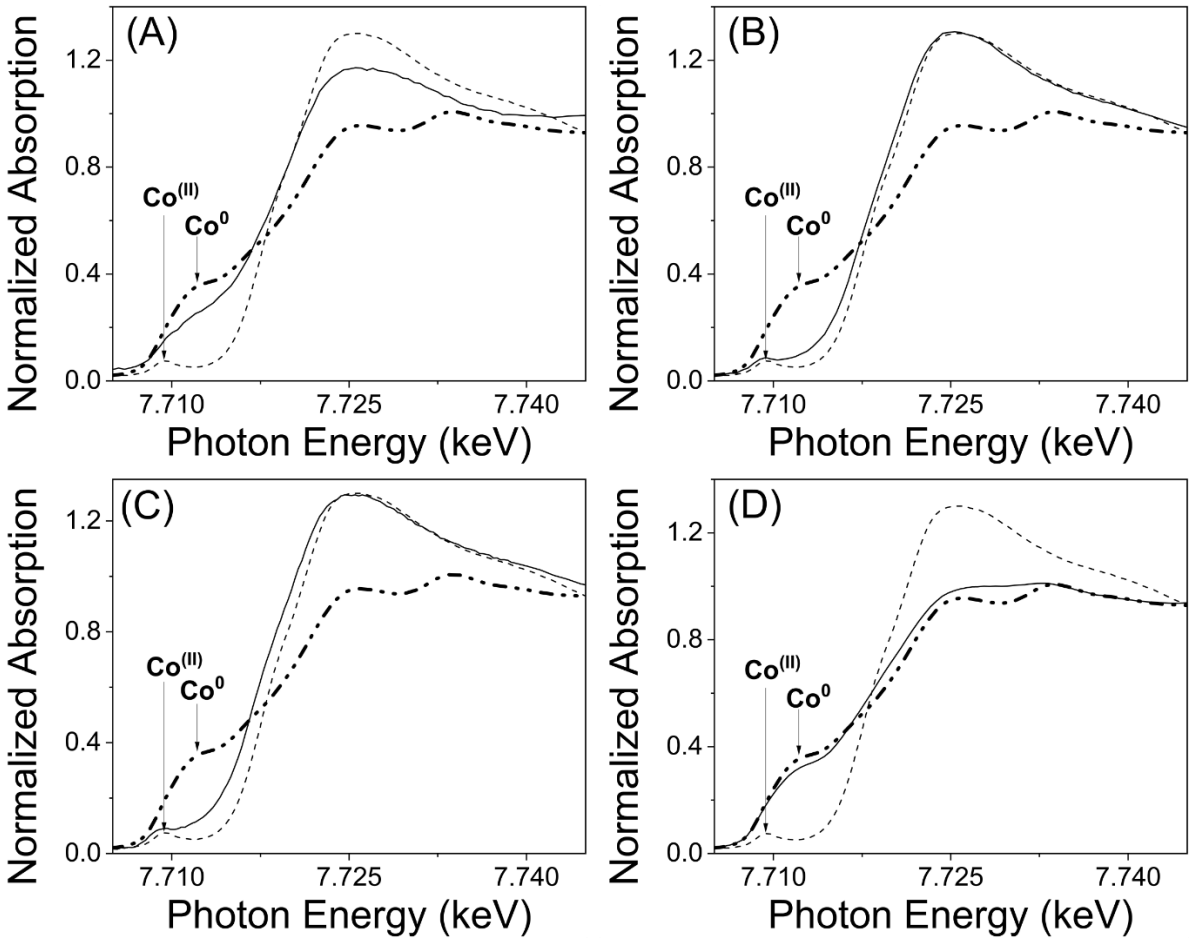

Figure 2.7. Comparison of XANES Spectra at the Co K edge for between metallic Co (bold dashed dotted line) and $Co^{(II)}$ (dashed line) oxidation states with (a) 2Pt0.6Co (solid line) in the upper left, (b) 2Pt1Co (solid line) in the upper right, (c) 2Pt1Co (solid line) in the bottom left and (d) 2Pt4Co on the bottom (solid line) in bottom right. Reprinted with permission from *ACS Catal.*, 2019, 9, 6, 5231-5244[43]. Copyright 2019 American Chemical Society.

The spectrum for 2Pt0.6Co has an intermediate shape compared to monometallic Co and $Co^{(II)}$. Both the edge energy, 7.7202 keV (Table 2.2), and the larger white line are similar to those expected for $Co^{(II)}$. A Linear Combination (LC) fit using the monometallic Co^0 and $Co^{(II)}$ single site spectra suggests the fraction of $Co^{(II)}$ is 0.41; while the remaining 0.59 is metallic Co (Table

2.3). Therefore, at 0.6% Co loading, not all Co atoms have been fully reduced and alloyed with Pt. There is a significant fraction of unreduced $Co^{(II)}$.

Table 2.3. XANES and EXAFS data at the Co K edge for the fully reduced Pt-Co bimetallic and monometallic Co catalysts. Reprinted with permission from *ACS Catal.*, 2019, 9, 6, 5231-5244[43]. Copyright 2019 American Chemical Society.

Sample	Edge Energy (keV)	Co^0 fraction	Co^{2+} fraction	Bond	Bond Distance (Å)	CN	σ^2	E_0 shift (keV)
10Co	7.7090	1.00	-	Co-Co	2.52	12	0.002	-0.2
$2Co^{(II)}$	7.7176	-	1.00	Co-O	1.98	4.2	0.000	-1.0
2Pt0.6Co	7.7202	0.59	0.41					
2Pt1Co	7.7173	0.11	0.89					
2Pt2Co	7.7166	0.21	0.79					
2Pt4Co	7.7089	0.86	0.14	Co-Co	2.51	11.4	0.002	-0.8

The spectrum for 2Pt1Co is similar to that of $Co^{(II)}$, except for a slight increase in absorption between the pre-edge peak and the white line, suggesting that almost all the Co is present as $Co^{(II)}$ ions. The edge energy is at 7.7173 keV (Table 2.2) slightly lower than the expected energy for pure $Co^{(II)}$ species. The LC fit suggests that $Co^{(II)}$ single site fraction is 0.89 while the remaining 0.11 is metallic. Given the previous results in the Pt L_{III} edge, it's likely the metallic Co is present in the Pt-Co bimetallic NP's (Table 2.3). The larger fraction of $Co^{(II)}$ likely result from the higher Co loading. Similarly, the XANES for the 2Pt2Co catalysts gives a LC fit with a $Co^{(II)}$ fraction of 0.79, indicating a large fraction of unreduced $Co^{(II)}$.

The spectrum of 2Pt4Co is similar in shape to the monometallic Co. This catalyst has a slight decrease in the absorption edge around 7.711 keV, with a slightly higher white line than Co^0. Its

edge energy, however, is 7.7089 keV (Table 2.2), the same as the monometallic Co spectra. The LC fit suggests that the fraction of $Co^{(II)}$ is 0.14; while the remaining 0.86 is reduced (Table 2.3).

Figure 2.8 shows the Fourier Transform (FT) of the EXAFS spectra for the Co foil, $2Co^{(II)}/SiO_2$, and bimetallic Pt-Co particles. As shown in the Figure 2.8d, Co foil, i.e., metallic Co, has a first shell around 2Å (phase uncorrected distance) consisting of one large peak with a small shoulder at lower R. From the EXAFS fit, the Co-Co bonds in $10Co/SiO_2$ have an average distance of 2.52 Å with a CN of 12 (Table 2.2), suggesting a large size for these nanoparticles.

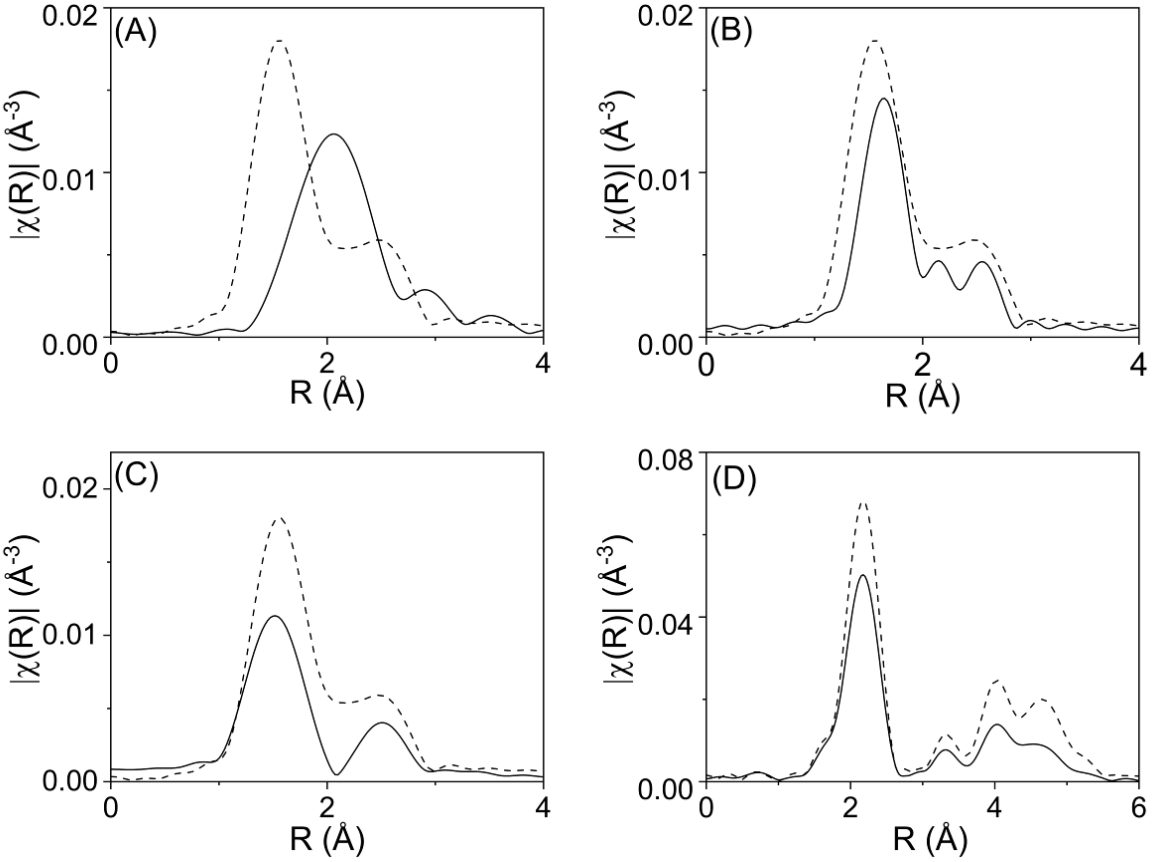

Figure 2.8. FT magnitudes of EXAFS Spectra at the Co K edge. (a), in the upper left, shows the comparison 2Pt0.6Co (solid) and $Co^{(II)}$ peaks (dashed); (b), in the upper right, shows the comparison between 2Pt1Co (solid) and $Co^{(II)}$ peaks (dashed); (c), in the bottom left, shows the comparison between 2Pt2Co (solid) and $Co^{(II)}$ peaks (dashed); and figure (d), in the bottom right, shows 2Pt4Co (solid) and Co foil (dashed). Reprinted with permission from *ACS Catal.*, 2019, 9, 6, 5231-5244[43]. Copyright 2019 American Chemical Society.

The $2Co^{(II)}/SiO_2$ spectrum, on the other hand, has a characteristic peak at lower R, (about 1.5 Å phase uncorrected distance) and negligible peaks at higher R. The EXAFS can be fit with 4.2 Co-O bonds at 1.98 Å and is consistent with $Co^{(II)}$ single sites on SiO_2 previously reported[66] , and no bulk Co oxides are visible.

The EXAFS spectra at the Co K edge for the reduced bimetallic samples are shown in Figure 2.8. Due to the overlapping Co-Co, Co-Pt, Co-O peaks in 2Pt0.6Co and 2Pt1Co, it's not possible to obtain a satisfactory fit of these spectra. A qualitative analysis, however, confirms what was observed in XANES. In the spectrum of 2Pt0.6Co, the main peak matches the position for the metallic Co peaks with some residual ionic Co-O bonds. This is consistent with the 0.59 metallic Co fraction found in XANES. The spectrum of 2Pt1Co matches the peak position for $Co^{(II)}$, also consistent with the 0.89 fraction found in XANES.

In the Co K edge EXAFS, 2Pt4Co has the same shape as the monometallic Co particles, with slightly lower magnitude of the Fourier transform. Even the higher shell scattering, between 3 and 5Å (phase uncorrected distance) can be observed, suggesting the presence of fully reduced, but larger monometallic Co nanoparticles with hcp structure. These Co-Co bonds are 2.50 Å with a CN of 11.4 (Table 2.2) consistent with the XANES LC fit. Given the strong presence of monometallic Co and the small fraction of $Co^{(II)}$, the Pt-Co and Co-O bonds are not observed.

The trend in the EXAFS spectra is consistent with that of the XANES spectra. Despite forming bimetallic Pt-Co particles, there's an excess of $Co^{(II)}$ single sites on the surface for loadings less than 2%. As the Co loading increases, the available amount of $Co^{(II)}$ single site species increases until enough $Co^{(II)}$ are available to fully reduce into metallic Co nanoparticles. At high Co loading, most of the Co is reduced forming monometallic Co NP's with little unreduced $Co^{(II)}$.

2.4.3 Synchrotron X-Ray Powder Diffraction (XRD)

In-situ synchrotron X-Ray Diffraction (XRD) measurements were performed at the 11-ID-C beamline, at Argonne National Lab. Due to the small sizes of the bimetallic NP's, the resulting peaks are broad and low in intensity and high flux synchrotron radiation is required. The high X-ray energy (105.70 keV, or $\lambda = 0.1173$ Å) gives diffraction patterns at lower 2θ angles than the laboratory XRD, typically, from 0 to 10º.

Figure 2.9a shows the XRD spectra for $3Pt/SiO_2$ catalysts. Due to the small size of these NP's, the peaks are broader than the bulk metallic Pt fcc structure, but it's clear all the catalyst peaks match those of the simulation. Therefore, this catalyst contains fully reduced monometallic fcc Pt. Based on the peaks' intensity, the size of the nanoparticle was determined as 2.5nm through Scherrer equation, consistent with the STEM.

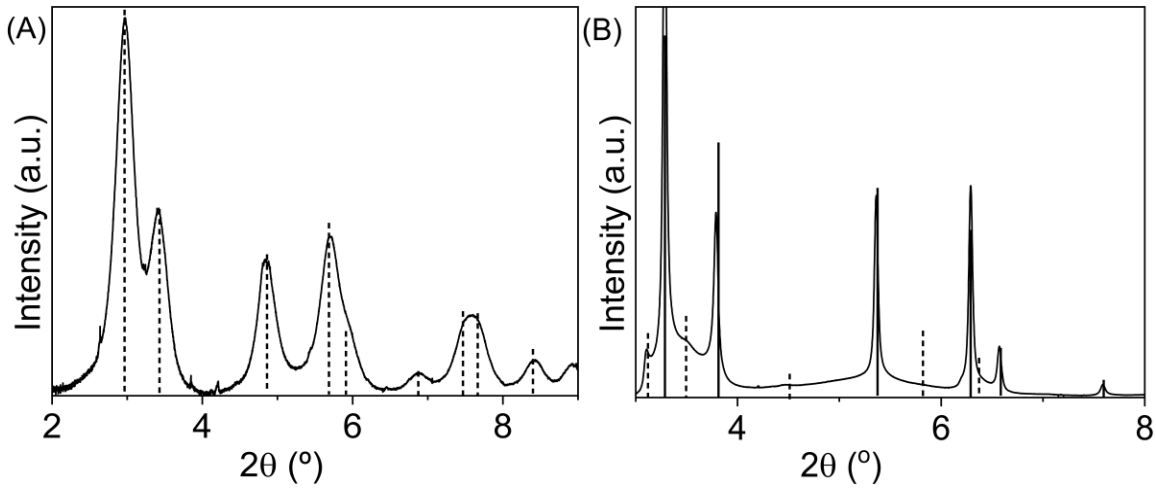

Figure 2.9. XRD Spectra for (a) $3Pt/SiO_2$ (solid line) with metallic Pt peaks position identified (vertical dotted lines) and (b) $10Co/SiO_2$ (solid lines), with peaks identified for fcc Co (vertical solid lines) and hcp Co (vertical dotted lines). Reprinted with permission from *ACS Catal.*, 2019, 9, 6, 5231-5244[43]. Copyright 2019 American Chemical Society.

The XRD pattern for the $10Co/SiO_2$ is shown in Figure 2.9b. In this pattern, two different phases can be identified based on the peak positions: hcp and fcc Co. The fcc peaks in the catalysts are very sharp and narrow, suggesting the presence of large nanoparticles. The peaks

corresponding to the hcp structure are broader and represent a stacking fault in the crystallites. The XRD for all catalysts were measured at room temperature after reduction in H_2 at 550ºC to reduce the effects of thermal displacement of the peaks at high temperatures. At room temperature metallic Co has an hcp structure and, as the temperature increases, it converts to fcc. Upon cooling the structure reverts back to hcp. However, as Figure 2.9b shows if cooling occurs rapidly the fcc structure does not fully relax to the hcp structure. Therefore, some Co is present in hcp structure, while the majority remains in the fcc structure. The estimated particle size calculated from the Scherrer Equation was 12 nm, which is consistent with the TEM particle size determination.

Figure 2.10a shows the diffraction pattern for the 2Pt0.6Co catalyst. In this catalyst, all peaks are slightly asymmetric towards higher 2θ angles. This asymmetric shape is the result of overlapping peaks of two different, but closely related phases. Comparison to simulated patterns reveals the peaks are consistent with monometallic Pt and Pt_3Co intermetallic alloy. The large peak positions are similar to fcc Pt, while the shoulders represent the peaks from Pt_3Co alloy phase. However, both Pt and Pt_3Co are slightly shifted to higher 2θ angles compared to bulk structures. This occurs due to the small size and the contraction of the bond distance in the NP's, resulting in surface strains effects and slightly smaller lattice parameters. Thus, the simulations were adjusted for lattice parameters contractions. These (Figure 2.10a) have the lattice parameter, *a*, contracted by 0.5% for the Pt phase and 1.5% for the Pt_3Co (structure type Au_3Cu), corresponding to 0.014Å and 0.041Å respectively. These changes are consistent with the shorter bond distances in the EXAFS.

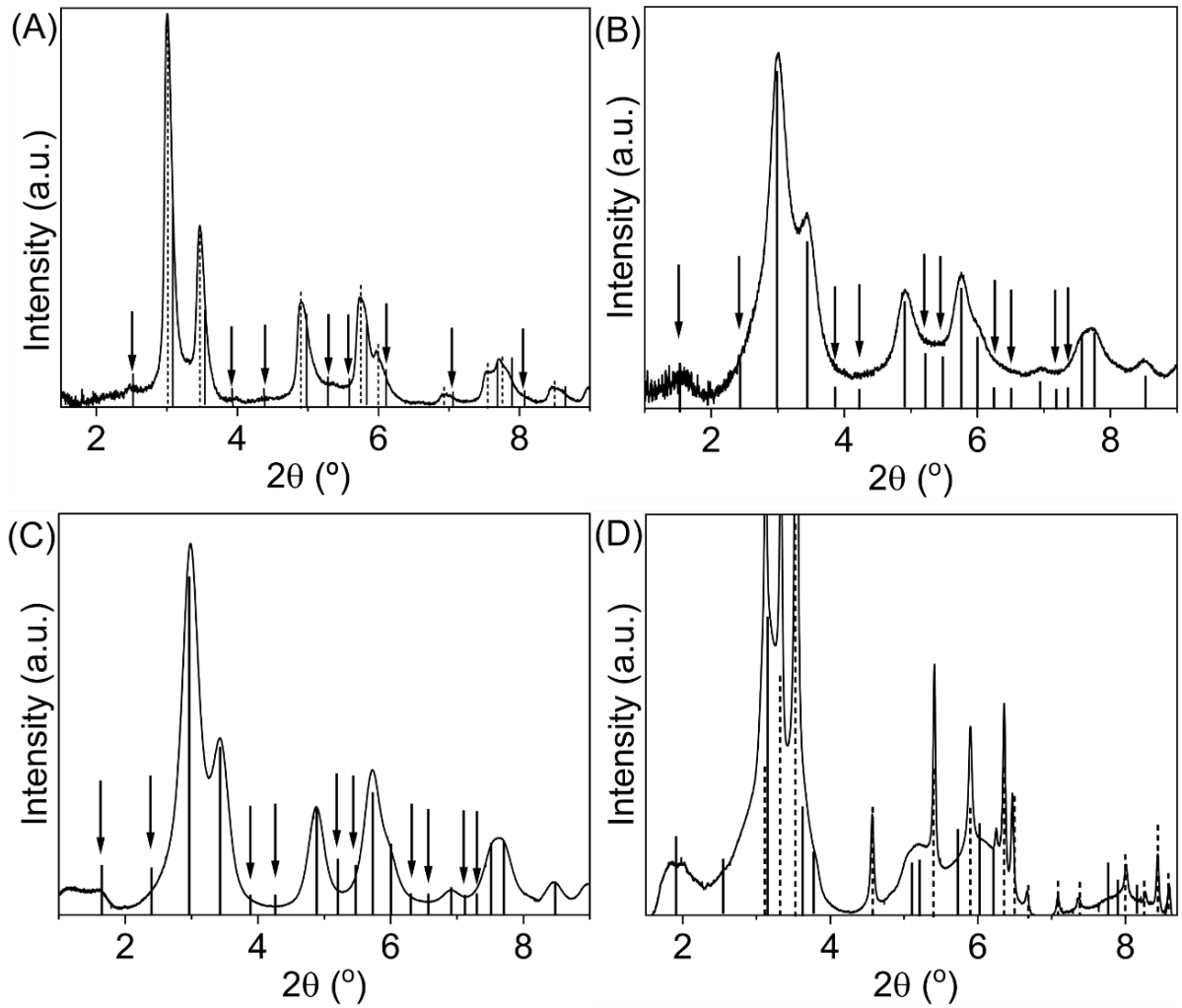

Figure 2.10. XRD Patterns for (a) 2Pt0.6Co/SiO2, compared to Pt fcc pattern (dotted vertical line), with lattice parameter *a* contracted by 0.5% (Δa=-0.5%), and Pt_3Co alloy phase (solid vertical lines), with Δa=-1.5%; (b) 2Pt1Co nanoparticles, compared with Pt_3Co alloy phase (solid vertical line), with Δa=-0.5%, and super lattice peaks indicated by arrows; (c) 2Pt2Co nanoparticles, compared with Pt_3Co alloy phase (solid vertical line) with Δa=-0.5%, and super lattice peaks indicated by arrows; and (d) for 2Pt4Co nanoparticles, compared to Co hcp (dotted vertical line) and orderd PtCo alloy phase (solid vertical lines) with Δa=-1.0% and 1.5% contraction for lattice parameter *c*. Reprinted with permission from *ACS Catal.*, 2019, 9, 6, 5231-5244[43]. Copyright 2019 American Chemical Society.

In addition to the asymmetric peaks, superlattice peaks arising from the lower symmetry of Pt_3Co are observed in diffraction pattern. Since these nanoparticles are less than 2nm in size, these peaks are very small, as shown on Figure 2.10a. The superlattice positions are listed Table 2.4. Thus, the XRD indicates the presence of two phases in 2Pt0.6Co: monometallic Pt and Pt_3Co.

Table 2.4. List of peak positions identified for the ordered alloy phases in each catalyst diffraction pattern. Reprinted with permission from *ACS Catal.*, 2019, 9, 6, 5231-5244[43]. Copyright 2019 American Chemical Society.

Catalyst	Phase	Main XRD Diffraction Peaks	XRD Superlattice peaks
2Pt0.6Co	Pt_3Co	3.03º, 3.5º, 4.96º, 5.81º, 6.07º, 7.01º, 7.64º, 7.84º	2.48º, 3.92º, 4.30º, 5.26º, 5.54º, 6.32º, 6.56º, 7.23º, 7.44º
2Pt1Co	Pt_3Co	2.99º, 3.45º, 4.88º, 5.73º, 5.98º, 6.91º, 7.53º, 7.72º	2.44º, 3.86º, 4.23º, 5.18º, 5.46º, 6.23º, 6.46º, 7.12º, 7.33º, 7.91º
2Pt2Co	Pt_3Co	2.99º, 3.43º, 4.87º, 5.72º, 6.00º, 6.91º, 7.52º, 7.71º	2.40º, 3.88º, 4.25º, 5.20º, 5.47º, 6.30º, 6.57º, 7.12º, 7.29º
2Pt4Co	Likely PtCo	3.10º, 3.54º, 5.08º, 5.88º, 6.03º	1.82º, 2.50º, 3.65º, 3.98º, 4.43º, 5.00º, 5.32º, 5.48º, 5.59º, 6.20º

Figure 2.10A shows the diffraction pattern for $2Pt1Co/SiO_2$ catalysts. In this spectrum, the peaks are symmetric and broad. Comparison with the simulated spectra, a good agreement was obtained for Pt_3Co phase with a 0.5% contraction in the lattice parameter *a*. Weak superlattice peaks are also observed and their positions are listed in Table 2.4. The 2Pt2Co diffraction pattern (Figure 2.10c) had very small, broad diffraction peaks with some peaks matching Pt_3Co; however, other peaks could not be identified.

The diffraction pattern for $2Pt4Co/SiO_2$ shows significant differences from the previous catalysts (Figure 2.10d). Two different phases can be identified in these nanoparticles. The first phase contains large, sharp peaks corresponding to a Co hcp pattern (with 1.0% contraction in lattice parameter *a* and 1.5% contraction on lattice c) suggesting the presence of larger monometallic Co nanoparticles. This agrees with the results from STEM and EXAFS fits. The second phase contains very small and broad peaks, indicating the presence of small bimetallic Pt-Co nanoparticles. However, due to the small size and the interference of much larger Co peaks, it is difficult to confirm the presence of either PtCo or Pt_3Co. Some peaks match closely those of

PtCo (between 5 and 6°, Table 2.4). However, the remaining peaks are difficult to confirm this structure.

Based on the XRD results, at very low Co loadings, there are two phases present: metallic Pt and a smaller ordered Pt_3Co alloy phase. As the Co loading increases, an ordered Pt_3Co alloy phase is formed. At high Co loading, formation of a more Co-rich PtCo alloy phase is likely and metallic Co nanoparticles are also present.

2.4.4 Surface Characterization

Despite the presence of similar intermetallic phases in the XRD patterns, i.e. Pt_3Co, the varying (Pt-Co):(Pt-Pt) ratios in the FT magnitude EXAFS at the Pt L_{III} edge and the presence of two phases in some of the XRD patterns suggest that the average composition of the nanoparticles among the catalysts is not similar. It is possible this difference is due to different compositions between the particle interior and the catalytic surface. Due to their small particle size, these catalysts have a large enough surface area that differences in the surface monolayer could be detected by EXAFS. Therefore, to characterize the surface structure, oxidation experiments were performed, and the oxidized and reduced spectra were subtracted to obtain the difference spectra corresponding to the surface composition (see the experimental section for details).

2.4.4.1 Pt L_{III} Edge – Oxidized Sample: Core Structure

After H_2 reduction at 550°C, the catalysts were exposed at room temperature to flowing 20% O_2 (balance He). Upon oxidation, there are loss of surface Pt-Pt and Pt-Co metallic bonds. The remaining metallic bonds in the spectra (Pt-Co and Pt-Pt), therefore, are due to metallic atoms from the nanoparticle interior, i.e. the NP core. Since there is a large fraction of surface atoms in these small NP's, by comparing the ratios of (Pt-Co):(Pt-Pt) bonds between the fully reduced and oxidized particles, it's possible to evaluate whether the composition is homogeneous throughout

the particle. In addition, the ratio of Pt-Co to Pt-Pt neighbors can be used to identify the ordered surface structure. Table 2.5 summarizes the results from the k²-weighted magnitude of the Fourier Transform (FT) of the EXAFS spectra at the Pt L_{III} edge for the oxidized bimetallic catalysts.

Table 2.5. EXAFS data at the Pt L_{III} edge for surface oxidized bimetallic Pt-Co and monometallic Pt catalysts. Reprinted with permission from *ACS Catal.*, 2019, 9, 6, 5231-5244[43]. Copyright 2019 American Chemical Society.

Sample	Edge Energy (keV)	Bond	Bond Length (Å)	CN	(Pt-Co):(Pt-Pt) ratio	σ²	E_0 shift (keV)
2Pt0.6Co	11.5641	Pt-O	2.05	0.5	0.29	0.001	5.44
		Pt-Pt	2.73	7.6		0.002	0.29
		Pt-Co	2.56	2.2		0.002	-3.38
2Pt1Co	11.5645	Pt-O	2.05	1.3	0.52	0.001	0.19
		Pt-Pt	2.73	2.3		0.002	-0.59
		Pt-Co	2.56	1.2		0.002	1.80
2Pt2Co	11.5644	Pt-O	2.05	1.3	1.67	0.001	1.62
		Pt-Pt	2.69	0.9		0.002	0.25
		Pt-Co	2.56	1.5		0.002	3.89
2Pt4Co	11.5645	Pt-O	2.05	1.2	2.23	0.001	1.24
		Pt-Pt	2.69	1.7		0.002	-2.54
		Pt-Co	2.56	3.8		0.002	5.54

The oxidation of 2Pt1Co led to a CN of 1.3 Pt-O bonds at 2.05 Å, 2.3 Pt-Pt at 2.73Å and 0.9 Pt-Co at 2.56 Å. Fully oxidized Pt has 4 Pt-O bonds (at 2.05 Å). Thus, the fraction of oxidized Pt, i.e., surface atoms, is given by the Pt-O CN/4. The (Pt-Co):(Pt-Pt) CN ratio of the metallic core is

0.51 , similar to that of the fully reduced 2Pt1Co (ca. 0.5) (Table 2.2). Thus, the core and average composition are very similar.

The oxidation of 2Pt2Co led to a CN of 1.3 Pt-O at 2.05 Å, and the metallic bonds in the core were a good fit for 1.3 CN for Pt-Pt at 2.69 Å and CN of 1.5 Pt-Co for 2.56 Å. The (Pt-Co):(Pt-Pt) CN ratio in the reduced sample is 0.97, while the metallic peaks in the core (oxidized catalyst) have a ratio of 1.7. This significant difference suggests a non-uniform metallic distribution, with the core composition much richer in Co than the fully reduced NP.

The oxidized 2Pt4Co catalyst had 1.2 Pt-O bonds at 2.05 Å, 1.7 Pt-Pt bonds at 2.69 Å and 3.8 Pt-Co bonds at 2.56 Å. The (Pt-Co):(Pt-Pt) CN ratio is 2.2, similar to that of 2.1 in the reduced catalyst (Table 2.2) suggesting a generally uniform metals distribution throughout the NP's.

2.4.4.2 Pt L_{III} Edge – Difference Spectra: Surface Structure

The difference in the EXAFS of a reduced and RT oxidized catalyst represents the surface composition since the core atoms remain unchanged and are subtracted from the two spectra. These reduced, oxidized and difference spectra are shown in Figure 2.11. In Figure 2.11A, the large peaks (solid line) of the reduced catalysts represent both Pt-Pt and Pt-Co bonds from 2 to 3 Å. The dotted spectrum in 6a shows the oxidized spectrum with loss of metallic neighbors and addition of a Pt-O peak at about 1.5 Å (phase uncorrected distance). In these bimetallic Pt-Co catalysts, the fraction of surface atoms is high, thus there is a significant Pt-O peak, which can be fit. However, in larger particles greater than about 10 nm the smaller number of Pt-O bonds often overlap the larger metal peaks in the oxidized sample and are difficult to accurately fit. In the difference spectrum, any atoms that are unchanged are not present in the difference spectrum. Thus, the Pt-Pt, Pt-Co and Pt-O are more easily resolved and fit in the difference EXAFS spectrum (Figure 2.11B). The fits for the difference EXAFS are shown in Table 2.6.

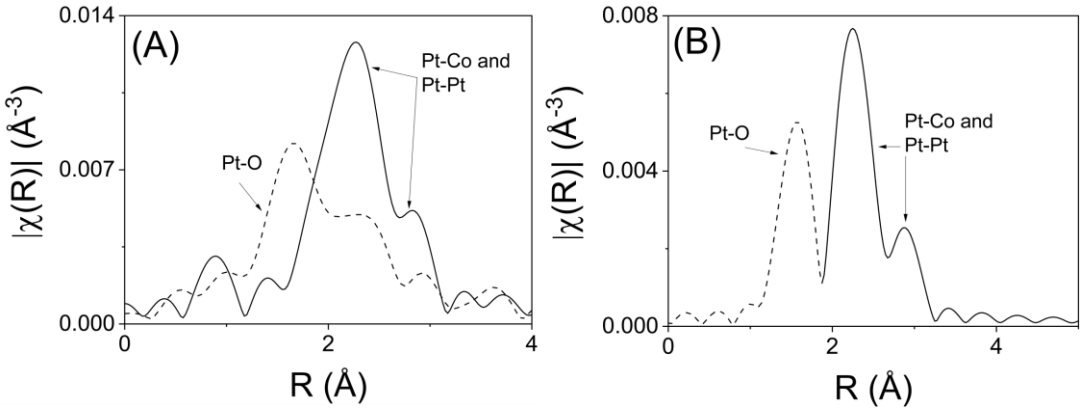

Figure 2.11. FT magnitude of the EXAFS for 2Pt1Co at the Pt L_{III} edge, where (A) shows both oxidized (dashed line) and fully reduced catalyst (solid line), and (B) is magnitude of the FT of the difference EXAFS spectrum with Pt-O peaks (dashed line) and metallic peaks (solid line). Reprinted with permission from *ACS Catal.*, 2019, 9, 6, 5231-5244[43]. Copyright 2019 American Chemical Society.

Table 2.6. Fitting results for the Fourier Transform Magnitude for the difference spectra at the Pt L_{III} edge for the bimetallic Pt-Co and monometallic Pt catalysts. Reprinted with permission from *ACS Catal.*, 2019, 9, 6, 5231-5244[43]. Copyright 2019 American Chemical Society.

Sample	Bond	Bond Length (Å)	CN	(Pt-Co):(Pt-Pt) ratio	σ^2	E_0 shift (keV)
3Pt	Pt-O	2.05	0.9	-	0.001	-1.10
	Pt-Pt	2.77	2.5	-	0.002	0.00
2Pt0.6Co	Pt-O	2.05	0.2	-	0.001	0.31
	Pt-Pt	2.73	0.6	0.5	0.002	-0.25
	Pt-Co	2.56	0.3		0.002	6.41
2Pt1Co	Pt-O	2.05	0.9	-	0.001	-4.62
	Pt-Pt	2.73	2.1	0.5	0.002	1.32
	Pt-Co	2.56	1.0		0.002	-3.64
2Pt2Co	Pt-O	2.05	0.9	-	0.001	-1.77
	Pt-Pt	2.73	2.4	0.5	0.002	-2.35
	Pt-Co	2.56	1.2		0.002	3.02

2Pt4Co	Pt-O	2.05	0.7	-	0.001	-2.16
	Pt-Pt	2.73	1.9	0.5	0.002	-3.14
	Pt-Co	2.56	0.9		0.002	2.53

An unexpected result in Table 2.6 is that the (Pt-Co):(Pt-Pt) CN ratio is 0.5 for all catalysts, despite the clear difference in their average and core compositions. This suggests that all catalysts likely have the same surface structure with different core compositions.

2.4.5 Catalyst Performance Testing

To further probe their surface, the bimetallic catalysts were tested for their propane dehydrogenation performance. A comparison between the catalytic surface of the bimetallic particles and their monometallic catalysts counterpart, i.e. Pt and Co, allows the identification of the exposed metals on the surface of the bimetallic catalysts.

Catalytic dehydrogenation of propane to propylene was conducted under two different conditions: without and with H_2 co-feeding at 550^{o}C. The latter provides a more severe test of catalyst performance than the former.

The experimental results in the absence of H_2 are shown on Figure 2.12a. Each data point corresponds to the selectivity and conversion from a separate catalyst test. For each test the catalysts were tested over a period of 30 min and the conversion and selectivity were extrapolated to zero time and minimal deactivation, which is plotted in Figure 12. The space velocity was varied (at constant temperature) to achieve different propane conversions from 5 to about 40%.

For the monometallic catalysts, there is a very sharp decrease in selectivity as the conversion increases. For monometallic Pt (without H_2), the selectivity is around 88% at 10% conversion, which decreases to about 72% at 25% conversion. For the monometallic Co, the selectivity is even

lower, about 60% at 10% conversion. The activity of the Co NP's was low and it was difficult to obtain much higher conversions at 550°C. The single site catalyst, $Co^{(II)}/SiO_2$, was also tested at the same temperature and space velocity, but the obtained conversions were negligible under these conditions. Due to its low activity, $2\%Co^{(II)}/SiO_2$ requires significantly more catalyst and lower flowrates of C_3H_8 to reach 5% conversion, where the selectivity was high at 99%. Therefore, in the Pt-Co bimetallic catalysts the contribution from single site catalysts is negligible at the tested temperature and space velocities.

The bimetallic Pt-Co samples, on the other hand, showed a very different trend compared to monometallic Pt and Co. As the conversion increases, all the bimetallic samples showed a slight decrease in the selectivity. The 2Pt0.6Co catalyst maintained a constant selectivity at 96% from 10% to 25% conversion. Both 2Pt1Co and 2Pt2Co catalyst, from 10% to 20% conversion, had a similar selectivity to 2Pt0.6Co, at 96% selectivity. Despite the large fraction of metallic Co in 2Pt4Co, this catalyst also had a constant selectivity around 92% from 10 to 20% conversion.

Since hydrogen (H_2) is required for hydrogenolysis, co-feeding H_2 is a more severe test of propylene selectivity. A second set of experiments was performed with 1.25% H_2 and 2.5% C_3H_8 (1:2 ratio). The conversion versus selectivity at the zero time on-stream of monometallic and bimetallic catalysts are shown in Figure 2.12b.

With addition of H_2, Pt catalysts display a significant decrease in the selectivity compared to no H_2. As the conversion increases, the selectivity loss is less rapid than in the absence of H_2. At high conversions, the olefin selectivity is very similar with and without H_2, about 60% at 30% conversion.

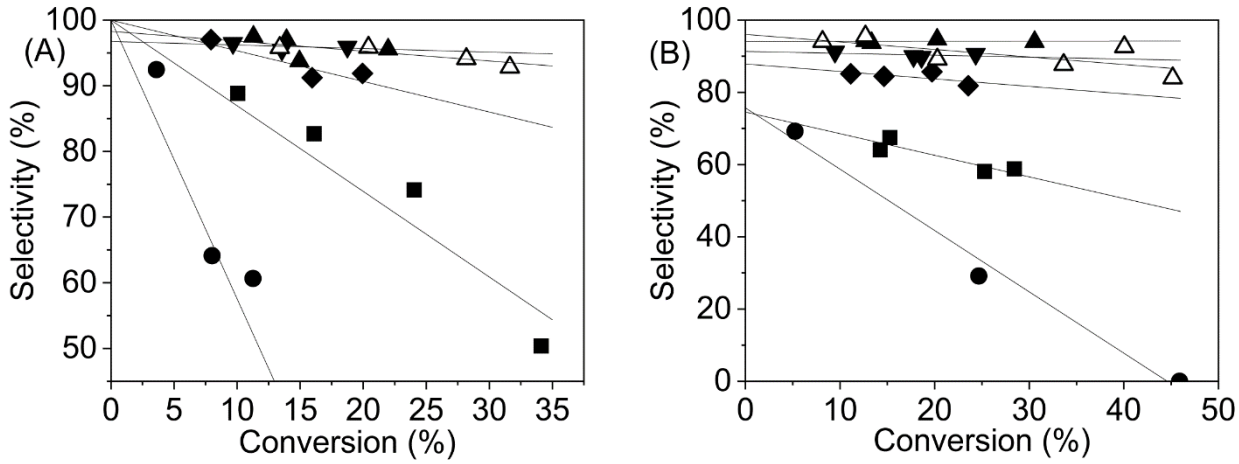

Figure 2.12. Conversion vs Selectivity at 550ºC and atmospheric pressure: (a) without H_2 at total flowrate of 200 cm^3/min, 2.5% C_3H_8; and (b) in the presence of H_2, total flowrate of 250 ccm^3/min, 2% C_3H_8 and 1% H_2. Catalysts evaluated: 3Pt (squares), 10Co (circles), 2Pt0.6Co (triangle), 2Pt1Co (downwards triangle), 2Pt2Co (unfilled triangle) and 2Pt4Co (rhombus). Reprinted with permission from *ACS Catal.*, 2019, 9, 6, 5231-5244[43]. Copyright 2019 American Chemical Society.

The propylene selectivity of 2Pt0.6Co decreased much less than observed for Pt and this selectivity remained nearly constant at 94% (compared to 96% without H_2) with increasing conversion, a behavior similar to the experiments in absence of H_2. Both 2Pt1Co and 2Pt2Co had a slightly lower selectivity than 2Pt0.6Co, but their selectivity also remained constant at about 90% with increasing conversions from 7% to 25%. The 2Pt4Co/SiO_2 had the lowest selectivity of these bimetallic catalysts. In the presence of H_2, the selectivity decreased to 85% from 10% to 25% conversion, compared to 92% without H_2.

Table 2.7. Propylene selectivity at zero deactivation time at 20% conversion of propane. Reprinted with permission from *ACS Catal.*, 2019, 9, 6, 5231-5244[43]. Copyright 2019 American Chemical Society.

	Without H_2 feeding[a]		H_2 cofeeding[b]	
Sample	$CH_4/C_2H_6/C_2H_4$ Yield (%)	Propylene Selectivity (%)	$CH_4/C_2H_6/C_2H_4$ Yield (%)	Propylene Selectivity (%)
2Pt0.6Co	1.1/0.4/2.5	96	1.2/0.9/3.3	94
2Pt1Co	0.6/0.5/2.9	96	2.4/2.6/4.5	90
2Pt2Co	0.6/0.4/3	96	2.4/3.3/5.3	89
2Pt4Co	3/0.4/4.6	92	5.8/2/7.2	85
3Pt	17/1/5	77	28/2/8	62
10Co	61/0/20	19	47/0/13	40

[a]No H_2 cofeed in the inlet. Reaction conditions: 550°C, atmospheric pressure. Total flowrate: 200cm^3/min, 2.0%C_3H_8 and balance N_2. [b]H_2 was cofed in the inlet stream. Reaction conditions: 550°C, atmospheric pressure. Total flowrate: 250cm^3/min, 2.0%C_3H_8, 1.0% H2 (2:1 ratio) and balance N_2

Table 2.7 summarizes the propylene selectivity at 20% conversion for these catalysts in absence and presence of H_2. The yields for the remaining products (methane, ethane and ethylene) are also given. Although both monometallic Pt and Co display low propylene selectivity, all bimetallic Pt-Co catalysts have significantly improved olefin selectivity, generally greater than about 95% in the absence of H_2. This similar selectivity suggests that the catalytic surface is similar in all lower loadings of Co (0.6% to 2%), i.e. Pt_3Co. The slightly lower selectivity in the 2Pt4Co suggests that excess Co in the bimetallic NP's has a slightly negative impact on the selectivity, which is likely due to the presence of monometallic Co nanoparticles and Co-rich core. In the more severe testing condition, i.e. in presence of H_2, the propylene selectivity affects the catalysts differently: the slight decrease in selectivity as the loading increase suggest that the excess Co

might have a slight negative effect on selectivity under harsher conditions, despite the same surface composition. This effect might be due to either to adsorption of H_2 on the neighboring Co atoms or due to the subsurface composition of the nanoparticles. The effect of the subsurface composition on the olefin selectivity has recently been reported, where different selectivities were achieved based on the subsurface layer composition[17].

2.4.5.1 Turnover Rate (TOR) Determination

For a reliable comparison of catalytic rates and identification of the active metal, it is necessary to normalize the conversion by the number of active sites, i.e., a turnover rate (TOR). In these catalysts, both Pt and Co are potentially the active atoms. Therefore, it's necessary to normalize the rate based on the surface composition of each metal. While a common method for determination of the fraction of surface atoms is chemisorption, this method is not effective for quantification of active Co and Pt since both metals may adsorb CO. To overcome this problem, the previous shown difference EXAFS spectra can be used to quantify the surface fraction of each metal.

Since fully oxidized Pt has 4 Pt-O bonds (at 2.05 Å), the Pt dispersion can be calculated by dividing the Pt-O CN (the difference spectra in Table 2.6) by 4. The fraction of surface Co atoms was calculated to be 1/2 that of the Pt dispersion since each catalyst appears to have a surface composition of Pt_3Co with a (Pt-Co):(Pt-Pt) ratio of 1:2. Table 2.8 summarizes the Pt dispersion and TOR's calculated for each catalyst for both the surface Pt and surface Co. For 10%Co/SiO_2, the dispersion was calculated based on the nominal dispersion from the XRD and STEM particle size determination.

Table 2.8. Summary of dispersion obtained from EXAFS Difference Spectra. Reprinted with permission from *ACS Catal.*, 2019, 9, 6, 5231-5244[43]. Copyright 2019 American Chemical Society.

Catalyst	Surface Pt[(a)]	TOR – Pt (s^{-1})[(b)]	TOR – Co (s^{-1})[(c)]
$3Pt/SiO_2$	0.23	0.2	-
$10Co/SiO_2$	-	-	0.1×10^{-1} [(d)]
$2Pt0.6Co/SiO_2$	0.08	0.8	1.6
$2Pt1Co/SiO_2$	0.23	0.9	2.4
$2Pt2Co/SiO_2$	0.23	0.9	1.8
$2Pt4Co/SiO_2$	0.18	0.4	0.7

[(a)] The fraction of surface Pt was calculated based ratio between the CN for Pt-O from the difference spectra and the CN of 4 for Pt-O in the reference used. [(b)] TOR for both bimetallic and monometallic Pt was based on the number of Pt atoms exposed on the surface, obtained from the surface Pt in the previous column. [(c)] TOR for the bimetallic Pt-Co catalysts was based on the exposed Co atoms on the surface. This was obtained from the 1:2 ratio of Pt-Co:Pt-Pt bonds on the Pt_3Co alloy. [(d)] Surface Co atoms for the monometallic catalyst was based on the nominal dispersion from the average particle size from STEM, i.e. 0.08 fraction of surface Co.

As shown in Table 2.8, the TOR for monometallic Co is much lower than monometallic Pt, i.e., 1.0×10^{-2} and 2.0×10^{-1}, respectively. The TOR's for the bimetallic catalysts based on Pt are similar in all catalysts and similar to that of monometallic Pt. On the other hand, the TOR's based on (bimetallic) Co are much higher than monometallic Co. Thus, the TOR's suggest that Pt is the active site for propane dehydrogenation and Co contributes little to the observed conversion.

2.5 Discussion

2.5.1 Alloy Formation

According to the Pt-Co phase diagram[62], there are two ordered intermetallic structures for binary alloys (Figure 2.2): Pt_3Co and PtCo with Au_3Cu and AuCu structure types, respectively.

The catalysts in this study show not only the presence of both structures but also the evolution of their formation with increasing Co loading.

Pt reduces at much lower temperature (250^{o}C) than Co (750^{o}C). Thus, it's likely that small Pt nanoparticles are initially formed. The addition of Co leads to bimetallic Pt-Co at lower temperature than required for Co reduction, suggesting that Pt catalyzes the reduction of Co, likely near the Pt NP. The catalyzed reduction of Co leads to small bimetallic NP of similar size to the initially formed monometallic Pt. At low Cobalt loadings, i.e. 2Pt0.6Co, there are two phases: fcc Pt and Pt_3Co (Au_3Cu structure type). The difference EXAFS and catalytic performance indicates that the surface is Pt_3Co (Figure 2.2B); while the metal peaks of the oxidized sample indicate a Pt-rich interior. The XANES at the Co K edge indicates the presence of both Co^0 and $Co^{(II)}$ oxidation states, about 0.41 $Co^{(II)}$ single sites and 0.59 Co^0 associated with the bimetallic particles. Recent calculations by Saedy *et al*[73], showed that Co atoms easily diffuse into Pt NP's and spread evenly among the Pt layers, maximizing the Pt around Co interaction and preferentially forming Pt_3Co. The fcc-like structure minimizes the energy required for rearrangement from the Pt fcc structure. Although there is sufficient Co in 2Pt0.6Co for a full Pt_3Co alloy, the formation of a stable surface Pt_3Co on the Pt-rich core also indicates that the Co atoms do not diffuse to the NP interior until there is additional Co near the NP surface. The unreduced Co^{2+} in the catalysts, therefore, is likely away from the bimetallic NP's.

As the Co loading increases, for example in 2Pt1Co catalyst, a full Pt_3Co alloy is formed. The NP composition is confirmed by XRD. The EXAFS of the reduced particle (Table 2.2) and difference (Table 2.5) EXAFS of the surface have (Pt-Co):(Pt-Pt) CN ratios around 0.5, consistent with a bulk and surface of Pt_3Co[74]–[77]. The Co K edge XANES indicates there are both $Co^{(II)}$

and Co^0, 0.89 and 0.11, respectively (Table 2.3). Thus, since the excess Co does not reduce at 550C, the $Co^{(II)}$ ions are likely distant from the bimetallic NP's.

Further increases in Co loading, e.g., 2Pt2Co, produce reduced bimetallic NP's with a (Pt-Co):(Pt-Pt) CN ratio of about 1, which indicates the presence of more Co than required for the Pt_3Co structure. While Pt_3Co has a (Pt-Co):(Pt-Pt) CN ratio of 0.5, the PtCo alloy (Figure 2.2a) has 8 Pt-Co bonds at 2.6 Å and 4 Pt-Pt bond at 2.69Å and a (Pt-Co):(Pt-Pt) CN ratio of 2. Thus, the 2Pt2Co is likely a mixture of these two phases. While the average (Pt-Co):(Pt-Pt) CN ratio is 1, the surface CN ratio is about 0.5 consistent with Pt_3Co. The metallic core has a (Pt-Co):(Pt-Pt) CN ratio of 1.7 consistent with a large fraction of PtCo. The Co K edge is a mixture of $Co^{(II)}$, about 0.79, and 0.21 Co^0 (or 0.4% Co). Full formation of PtCo would require 0.6 g of Co for a full PtCo alloy. Thus, the fraction of metallic Co from the XANES is also consistent with a mixture of Pt_3Co and PtCo. The XRD pattern for this catalyst contains peaks consistent with Pt_3Co; however, these are weak and other peaks are also present, which doesn't allow for precise determination of the structure(s). Thus, the XRD supports a Pt_3Co phase but it is inconclusive for the presence of a PtCo alloy phase. Nevertheless, the EXAFS indicates that in 2Pt2Co the NP's are more Co rich than in 2Pt1Co, for example. Thus, despite the similarity in the surface structure, the core is likely a large fraction of PtCo alloy. The presence of $Co^{(II)}$ in this catalyst again indicates that the majority of the Co is distant from the bimetallic NP's and dispersed on the support.

At the highest loading, the 2Pt4Co, the EXAFS indicates a (Pt-Co):(Pt-Pt) ratio of 2.23, very similar to a PtCo structure. The NP core has a (Pt-Co):(Pt-Pt) CN ratio near 2 consistent with PtCo alloy at the NP interior. However, the difference spectrum of the surface has a 0.5 ratio, suggesting a Pt_3Co structure, similar to the other catalysts. The XRD, however, is inconclusive for the identification of these two phases, due to the very small, broad peaks of the bimetallic particles

and the interference of large Co NP peaks. Although the Pt_3Co on the surface cannot be confirmed in the XRD, this diffraction pattern does show two phases: Co hcp structure, with sharp peaks; and broad peaks of PtCo, with a AuCu structure type. In this catalyst, nearly all of the Co is reduced to metallic NP's, either as in the PtCo alloy or monometallic Co. Nevertheless, the excess Co, which forms large monometallic NP's, does not lead to enrichment of the Pt_3Co surface. Thus, it's possible Pt_3Co is a more thermodynamically stable phase.

The summary of these characterizations leads to structures and morphologies shown in Figure 2.13. The specific NP composition, structure and morphology depends on the Pt:Co ratio and the availability of Co near the Pt NP's, which are initially formed. While the exact structure and morphology are different at different Co loadings, the surface of each is a Pt_3Co structure.

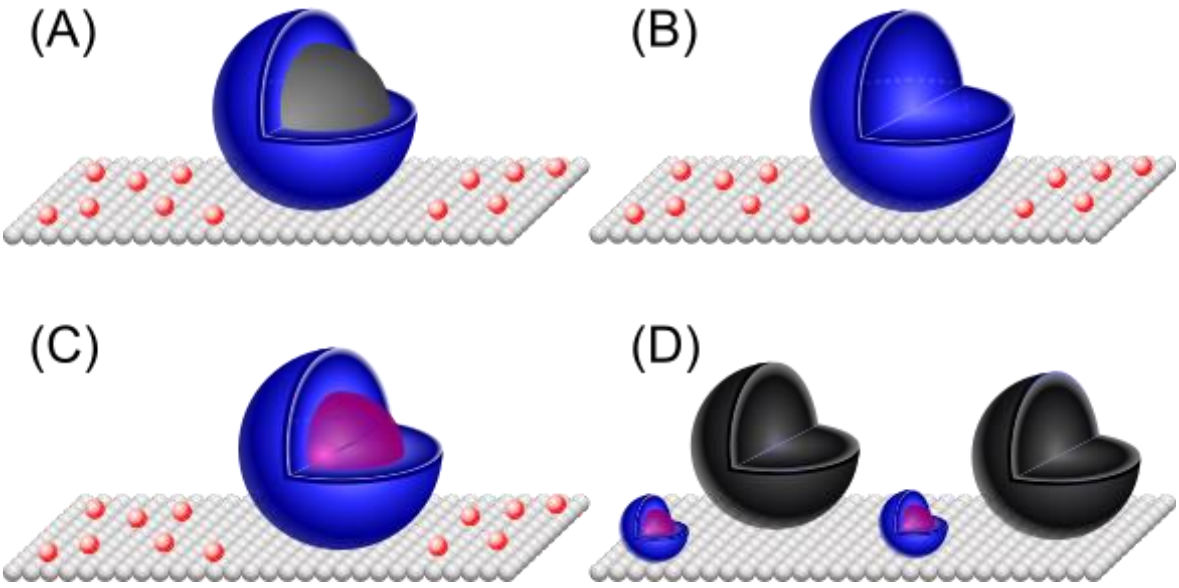

Figure 2.13. Schematics of the evolution of alloy formation as the Co loading increases: (A) 2Pt0.6Co – Pt_3Co alloy surface (blue) with a Pt core (grey); (B)2Pt1Co – full Pt_3Co alloy (blue sphere); (C)2Pt2Co - Pt_3Co alloy surface (blue) with a PtCo alloy core (purple); (D)2Pt4Co – same bimetallic particles as the 2Pt2Co and large monometallic Co nanoparticles. The excess $Co^{(II)}$ single sites are represented as the red spheres in pictures (A) to (C). Reprinted with permission from *ACS Catal.*, 2019, 9, 6, 5231-5244[43]. Copyright 2019 American Chemical Society.

2.5.2 Geometric Effect of Pt_3Co on Propylene Selectivity

Based on the TOR shown in Table 2.8, monometallic Co has a TOR about 20 times lower than monometallic Pt. The TOR based on the Pt atoms on the surface of the bimetallic Pt-Co catalysts have a similar value to that of monometallic Pt. The similarity in TOR as well as the difference between the TOR of monometallic Pt and Co, suggest that Co activity is negligible compared to that of Pt and propane molecules preferentially react on Pt sites. Therefore, despite monometallic Co catalysts being active, metallic Co behaves as an inactive structural promoter in Pt-Co alloys, similarly to Zn, Sn, Ga, In, and other post-transition elements and Pt atoms behave as the only active site.

In the bulk face centered cubic (fcc) structure, Pt has 12 other Pt neighbors at a bond distance of 2.774 Å. In the Pt_3Co intermetallic alloy, there is a decrease in the Pt-Pt coordination number to 8 with 4 Pt-Co bonds. Assuming the surface plane is the most stable with the highest atom density, the Pt-Pt ensembles of the (111) planes in Pt and Pt_3Co are shown in Figure 2.14. In the monometallic Pt, there are ensembles of more than 7 Pt atoms. In a Pt_3Co, however, there are 3-fold Pt-Pt ensembles at 2.75 Å symmetrically distributed.

Since hydrogenolysis is a structure sensitive reaction, the decrease in the Pt ensembles size significantly inhibits the cleavage of C-C bonds. For example, in the Pt (111) face, where ensembles of more than 5 Pt atoms are close together, hydrogenolysis is still likely due to adsorption of propane on multiple Pt atoms. The Pt catalyst has a propylene selectivity of 77% at 20% conversion (Table 2.7). Once a Pt_3Co surface is formed, the large Pt ensembles are broken, and the new ensembles have 3 adjacent Pt atoms on a (111) face. Propane now has fewer Pt sites and hydrogenolysis is inhibited. This leads to a decrease in the rate of the structure sensitive hydrogenolysis, while having little effect on rate of structure insensitive dehydrogenation reaction[78], [79]. Propylene selectivity increases to 96% at the same conversion (Table 2.7). In

summary, the suppression of hydrogenolysis by structural changes on the surface leads to an increased propylene selectivity. Similar geometric effects for non-active promoter atoms have been reported for Pt_3M and PtM intermetallic alloys with Sn, Zn, In, Mn and Cu[16]–[18], [61], [80].

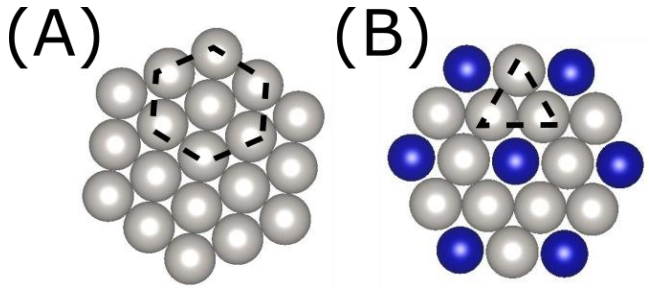

Figure 2.14. Possible exposed planes and their respective Pt ensembles size (dashed black line) for each structure: (a) Pt (111); (b), Pt_3Co (111). Pt atoms are in grey and Co atoms in blue. Reprinted with permission from *ACS Catal.*, 2019, 9, 6, 5231-5244[43]. Copyright 2019 American Chemical Society.

In the absence of cofed H_2, the selectivity is similar in all Pt-Co catalyst despite the increased Co loading, due to the same Pt_3Co surface in all catalysts. As the Co content of the bimetallic NP's increase, there is a slight but continual decrease in the olefin selectivity in the presence of cofed H_2 suggesting that the core composition affects the selectivity. As the Co in the core increases, there is a slight decrease in the olefin selectivity.

2.5.3 Electronic Effects of Alloying

As observed in Figure 2.5, the formation of bimetallic Pt-Co particles affects the XANES spectra, resulting in a slightly lower intensity of the white line and an edge shift towards higher energies. Since the XANES spectra results from a dipole allowed, photo-excitation of a 2p electron and an unfilled Pt 5d-orbital, these changes suggest an increase in the energy of the unfilled d-orbitals. Thus, bonding of Co with Pt changes the energy of the valance orbitals responsible for

catalysis. Resonant inelastic X-ray spectra of a Pt_1Zn_1 intermetallic showed that when the energy of the unfilled orbitals increase, there is a similar decrease in the energy of the filled 5d orbitals, which are responsible for catalysis[61]. The energy of the XANES also increases with increasing Co loading. In order to determine the shift in energy responsible for catalysis, one needs to determine the structure of the surface and also prepare a phase pure sample of this surface structure. For example, in 2Pt0.6Co, the surface is Pt_3Co, but the XANES is characterized by the sum of all Pt atoms. Since there are two phases, Pt_3Co and Pt, the XANES energy shift is not characteristic of the surface. For this sample the XANES energy is too low. Similarly, for 2Pt4Co, there are also two phases, Pt_3Co and PtCo. Again, the surface is Pt_3Co, but the XANES energy is too large and not representative of the surface. Only in the 2Pt1Co, is there a single phase where the NP and surface composition are the same. Thus, the XANES of this sample correctly reflects the electronic changes in the surface Pt atoms. Other methods for characterization of the electronic properties, for example XPS or RIXS, would be similarly affected. Proper quantification of the changes in the electronic properties of the surface are also important for DFT modeling of the proper catalytic structure.

The XANES shift to higher energies in Pt_3Co also suggests a lowering of the energy of the filled 5d-orbitals. Since the filled Pt 5d orbitals form bonds with reactants, the resulting metal-adsorbate bonds are weaker. These weaker bonds result in lower surface coverage of reactants and products including propylene and hydrogen. Facile desorption of propylene would also lead to fewer side reactions, like hydrogenolysis and coking. A lower surface coverage of H_2 would also lead to lower hydrogenolysis rates and improved olefin selectivity. Similar conclusions from theory[17], [73], [81] and experiment[17] have been reported for other alloy dehydrogenation catalysts.

2.6 Conclusion

Bimetallic catalysts with two active metals, Pt and Co, were synthesized with different Co loadings for propane dehydrogenation. Using in situ XAS, XRD, and an XAS surface analysis, the catalysts were shown to lead to different intermetallic structures with different morphologies related to their Co loading. At low Co loadings, stable surface Pt_3Co surface alloys with a Pt-rich core were formed. As the Co content increased, the catalyst composition formed a full Pt_3Co phase with excess the excess $Co^{(II)}$ remaining on the silica. Further increases in Co lead to a PtCo alloy phase in the core, despite the surface remaining as Pt_3Co. At high Co loadings, the Co in excess of that needed for bimetallic alloy formation resulted in large monometallic Co nanoparticles. Despite the different nano-structures in these catalysts, the catalytic surface in each of these catalysts had a Pt_3Co structure.

All Pt-Co catalysts have much higher propylene selectivity for propane dehydrogenation than mono-metallic Pt or Co. The high selectivity was maintained at high conversion and in the presence of co-fed H_2. The TOR of Pt in the bimetallic catalysts is similar to that of mono-metallic Pt and is suggested to be the active site in these alloys. The catalytic performance of bimetallic Pt-Co is typical of other intermetallic Pt alloys with non-catalytic post transition elements like Sn, Zn, Ga and In. The ability of Co to act as a non-active promoter is likely due to the lower TOR than Pt. The high olefin selectivity of the surface Pt_3Co is suggested to be due to geometric effects where there are smaller Pt-Pt ensembles as well as a decrease in the energy of the Pt 5d orbitals than in monometallic Pt. Therefore, if the activity between two metals is significantly different, i.e. by an order of magnitude, the least active metal will likely behave as a non-catalytic promoter, allowing the geometric effects to enhance the selectivity.

Quantification the surface structure was only possible due to the analysis of the difference EXAFS spectrum of the reduced and oxidized catalyst. The changes in the surface were generally

too small to detect by the average EXAFS, or XRD of the reduced sample. Identification of a specific structure by EXAFS is generally not possible. However, utilization of XRD to confirm possible nano-structures where the EXAFS can also be obtained allows one to identify the structure from ratios of CN's. Determination of the surface structure is essential for determination of correct structural and electronic effects affecting the catalytic performance. Proper identification of the surface structure along with preparation of NP's with the same uniform structure will allow for proper determination of the geometric and electronic properties, which control the catalytic performance.

3. ETHYLENE OLIGOMERIZATION ON $CO^{(II)}$ SINGLE SITE CATALYSTS SUPPORTED ON SILICA

3.1 Introduction

Ethylene oligomerization is a key process in the chemical industry, as the produced higher molecular olefins are further upgraded into a wide range of valuable products, such as polyethylene, lubricants and even fuels[36], [82], [83]. The current supply of ethylene is mainly produced by ethane steam cracking process[82]. Due to the increase in shale gas exploitation, of which ethane corresponds to about 70% of the non-methane hydrocarbon composition, an increase in the capacity of the ethane crackers is expected and, consequently, the larger ethylene supply will motivate the research of new processes and catalysts for ethylene oligomerization[3]. The current commercial oligomerization process utilizes homogeneous transition metal, organometallic catalysts, such as Ni, Cr, Zr, Ti. Co-catalysts such as methylaluminoxane, MAO, are often also required as initiators[84], [85]. During initiation, the co-catalyst provides the alkyl ligand to the metallic center, creating an M-alkyl bond, enabling a Cossee-Arlman mechanism, i.e., ethylene insertion to the M-alkyl bond leading to chain growth, followed by product formation by a β-hydride elimination[28], [82]. Ethylene insertion to the metal-hydride regenerates the M-alkyl intermediate. In this process, the product distribution usually follows a Schulz-Flory distribution[24]. Among the homogeneous catalysts, Ni^{+2} compounds are widely used due to its high activity and selectivity[2], [84], for example, as in the SHOP process.

However, homogeneous processes have several disadvantages for large scale applications. Catalyst recovery and reusability are low due to the complex separation of the catalyst form products and solvent. In addition, the high sensitivity to impurities limit catalyst recycle. More importantly, the process is not environmentally friendly due to the high usage of solvents, which

are problematic in wastewater treatment facilities[86]. Thus, the search for green catalysts has motivated the research for suitable heterogeneous catalysts.

Due to the high activity of Ni homogeneous catalysis, the majority of reported heterogeneous catalysts are Ni^{2+}, especially on acid supports like silica-alumina, SBA-15 or zeolites[37], [40], [82], [87], [88]. The interaction between the Ni^{+2} sites and zeolite Brønsted acid sites is reported to enhance the ethylene oligomerization activity. These catalysts show a high conversion over temperature from about 50ºC to 200ºC and high ethylene pressures. In some of these processes, the catalysts are operated inside slurry batch reactors, with heptane solvent. At higher temperatures, C_2H_4 can be fed in the gas phase, which facilitates the separation process between catalysts and products and allows for a continuous process. At temperatures above 300ºC, heterogeneous Ni^{+2} catalysts begin to deactivate due to reduction to metallic Ni and zeolite's pore blockage by high molecular hydrocarbons.

For both homogenous and heterogeneous oligomerization catalysts, there is general agreement that Ni^{+2} hydride and alkyl groups are intermediates[15]. In a study by Hu *et al*[16], Co^{2+} single sites supported on SiO_2 catalyzed the dehydrogenation of propane at 550ºC and hydrogenation of propylene at 200ºC. Key reaction intermediates for these reactions with single site catalysts were suggested for cation hydride and alkyl groups[16-20]. While homogeneous Co organometallic complexes are commonly proposed for ethylene oligomerization[25], due to their lower intrinsic activity compared to Ni^{+2}, few studies have been reported for heterogeneous Co oligomerization catalysts[89], [90].

Since dehydrogenation and hydrogenation reaction of single site Co^{II}/SiO_2 catalysts are thought to be the same as those required for oligomerization, the goal of this work is to evaluate these catalysts for olefin oligomerization. The catalysts were prepared by Strong Electrostatic

Absorption (SEA), and their known catalytic performance forpropane dehydrogenation, propylene hydrogenation were confirmed. Similarly, the catalyst's structure was confirmed by X-Ray Absorption Spectroscopy, including under oligomerization reaction conditions at high temperature. The presence of Co^{+2} hydride reaction intermediates was confirmed by HD formation in H_2/D_2 isotopic exchange experiments.

3.2 Experimental Section

3.2.1 Catalyst Synthesis

The Co^{II}/SiO_2 catalysts were synthesized by strong electrostatic adsorption (SEA), as described by Hu et al[66], to achieve Co^{2+} single site catalysts. A precursor solution was prepared with 2.5 g of hexamine cobalt chloride ($Co(NH_3)_6Cl_3$ – Sigma-Aldrich) dissolved in 25 mL of Millipore water. Simultaneously, 10.0 g of SiO_2 (Davisil 636 silica gel, Sigma–Aldrich, 35-60 mesh, surface area = 480 m^2/g, pore volume = 0.75 cm^3/g) was put in a separate beaker containing 50 mL of Millipore water. The pH for the SiO_2 container was corrected to 11 using 30% ammonium hydroxide solution (NH_4OH). Due to the slightly acidic nature hydroxyl groups on groups on SiO_2, at high pH deprotonation of the SiOH groups leads to a negative surface charge. This allows a strong interaction between the cationic ligands and the negative surface, resulting in homogeneously dispersed on the SiO_2 surface. The two solutions, precursor and SiO_2, were combined and stirred for 5 minutes to allow the saturation of the Co cation on the SiO_2 surface. After stirring, the SiO_2 was left to decant from the solution. The solids, SiO_2, were triple rinsed with Millipore water followed by vacuum filtration to remove all solution from the solids. The resulting catalyst was dried in the oven for 12 h at 125°C and then calcined at 300°C for 3h. Atomic Absorption Spectrometry (AAS) confirmed a Co loading of 3.1 wt.%.

A single site Ni^{II}/SiO_2 was also synthesized for benchmarking, according to the experimental procedure reported by Guanghui et al[91]. The Ni loading was also similar to that of the Co catalyst at about 3 wt%.

3.2.2 Structural Characterization - X-Ray Spectroscopy

The *In situ* XAS experiments were carried out at the 10-BM beamline at the Advanced Photon Source (APS) at Argonne National Laboratory (ANL). All measurements were performed at the Co K edge (7.709 keV) in transmission mode in fast scan from 250 eV below the edge to 550 eV above the edge, taking approximately 10 minutes per scan. The monochromator was calibrated for the edge energy of a Co metal foil. Simultaneous measurements of this foil was taken along the samples spectra for energy calibration of each spectra edge energy.

The Co^{II}/SiO_2 catalysts were pressed into a stainless-steel 6-shooter sample holder and placed inside a 1-inch quartz tube (XAS cell). Inside the cell, different treatments were carried out for the catalysts: (1) heated to 500^{o}C in He, held for 30 minutes and cooled down to room temperature (RT) in He; (2) heated to 200^{o}C in H_2, held for 30 minutes and cooled down to RT in H_2; (3) heated to 200^{o}C in C_2H_4, held for 30 minutes and cooled down to RT in C_2H_4; (4) heated to 550^{o}C in H_2, held for 30 minutes and cooled down to RT in H_2. After each treatment, the cell was sealed to avoid air contamination and measured at the BM-line. All measurements were carried out at RT to avoid thermal distortion in the spectra and allow an accurate comparison between samples. Additionally, an Oxytrap was used on all gas lines to avoid trace air contamination.

All the data were analyzed using WinXAS 3.1, Artemis and IFEFF-fit software to find the coordination number and bond distance using standard procedures. An initial analysis of the Co foil was carried out in Artemis to obtain the S_o^2 magnitude (S_o^2=0.749) for FEFF calculations. The

phase and amplitude functions for Co-O bonds were calculated in FEFF6 using cobalt oxide (CoO) as a reference (CN=6, R=2.13 Å). Then, the spectra for each treatment was fit in the first coordination shell of the k^2-weighted Fourier transform (FT) from the corresponding k-space from Δk=2.5-10.6 $Å^{-2}$ using the method of the least square method. This first coordination shell in R-space was in the range from ΔR=0.8-2.0$Å^{-1}$ and both imaginary and magnitude components were fit.

3.2.3 Propane Dehydrogenation and Propylene Hydrogenation

Catalytic performance tests for propane dehydrogenation and propylene hydrogenation were carried out in a fixed bed reactor within a 3/8-inch OD quartz reactor tube. Quartz wool was used to keep the catalyst bed in place. The reactor was loaded inside a vertical tubular clam shell furnace for temperature control.

For the propane dehydrogenation experiments, about 1.000 g of Co^{II}/SiO_2 was loaded to the reactor. The catalyst bed was dehydrated in 100 mL/min of N_2 at 500ºC for 30 minutes. The temperature was then ramped up to 550ºC to start the reaction. The reaction was carried out under atmospheric pressure (1.3 atm) and a total flowrate of 82 mL/min, consisting of 3.0% C_3H_8 and 2.0% H_2 in balance N_2. The reaction was carried out for about 1.5 hours and conversion was targeted around 5.0%.

For the propylene hydrogenation experiments, about 0.250 g of Co^{II}/SiO_2 was mixed with 0.750 g of SiO_2 to compose the catalytic bed loaded into the reactor. The catalysts were pretreated using one of the following pretreatments: 1) ramped to 200°C in 100mL/min of N_2, 2) ramped to 200°C in 100 mL/min of 5.0% H_2 in balance N_2, or 3) ramped to 550°C in 100 mL/min of 5.0% H_2 in balance N_2 and then cooled to 200°C for the reaction. The reaction was carried out at 200ºC under atmospheric pressure (1.3 atm) and a total flowrate of 104 mL/min, consisting of 0.66%

C_3H_8 and 3.4% H_2 in balance N_2. The reaction was also carried out for about 1.5 hours and conversion was targeted around 7.5%.

Data points were collected every 4.5 minutes for both reactions. Dehydrogenation and hydrogenation products were analyzed with a Hewlett Packard (HP) 6890 Series gas chromatograph (GC) using a flame ionization detector (FID) with a Restek Rt-Alumina Bond/Na_2SO_4 GC column (30 m in length, 0.32 mm ID, and 0.5 μm film thickness). Conversion was calculated by the molar difference between the hydrocarbon reactant (propane or propylene) in the inlet and outlet, while the selectivity (propylene or propane) was calculated based on the gas product distribution. Turnover Frequency (TOF) were calculated by the normalization of reactant consumption by the metallic moles present. The equations are shown below.

$$X=\frac{\text{moles of reactant in inlet-moles of propane in outlet}}{\text{moles of propane in inlet}}*100\%$$

$$S=\frac{\text{moles of } C_3H_6}{\text{moles of } C_3H_6+\frac{2*\text{moles of } C_2}{3}+\frac{\text{moles of } CH_4}{3}}*100\%$$

3.2.4 High Pressure Ethylene Oligomerization

Due to the low activity of Co^{II}/SiO_2 at atmospheric pressures, C_2H_4 oligomerization reactions were carried out at high pressures, different temperatures and varying space velocities. Two sets of experiments were carried out: (1) Ni^{II}/SiO_2 benchmarking and (2) Higher pressures and temperatures. For the first set, the reaction pressure was set at 400 psi and reaction temperature was 250ºC. The reaction feed consisted of 10 mL/min of 5% CH_4 in balance N_2, to be used as an internal standard, and varying flowrates of pure C_2H_4. Both Ni^{II}/SiO_2 and Co^{II}/SiO_2 were evaluated with total catalyst loading of 1.000g. For the second set, the pressure was set at 500 psi and varying

flowrates of pure C_2H_4 was fed, with no cofeeding of CH_4. Reaction temperature was varied in a range from 300°C to 500°C. Only Co^{II}/SiO_2 was evaluated with loadings varying from 0.500g to 2.000g.

The oligomerization reactions were carried out in a 1/2-inch OD 360 stainless steel tube. The catalyst was held in place by a quartz wool bed loaded around halfway length in the reactor and a 1/4-inch 360 stainless steel tube, “dead man”, under the quartz wool and reaching the bottom of the reactor. The reactor was sealed using VCR fittings in both inlet and outlet. The reactor was loaded inside a vertical tubular clam shell furnace for temperature control.

Before each experimental run, the catalyst was pretreated with flowing 100 mL/min of N_2 at the reaction temperature and pressure for about 1 and a half hour for the gas and GC stabilization. After this period, the gases were switched to start the reaction. The reaction was carried out for about 1.5 hour for each flowrate before switching to new flowrates. Due to the lack of deactivation, the experiments were run continuously at the same pressure for about 8 hours, switching flowrates.

Data points were collected every 30 minutes for each space velocity and partial pressure. The oligomerization products were analyzed with a Hewlett Packard (HP) 7890 Series gas chromatograph (GC) using a flame ionization detector (FID) with an Agilent HP-1 column (60 m in length, 0.32 mm ID, and 5 μm film thickness). Conversion was determined based on the total moles of carbon detected by the column, while the oligomers yield was determined by the distribution yield of the detected products, as shown in equations 2-3. The turnover rate (TOR) was calculated by the normalization of reactant consumption by the metallic moles present. The equations are shown below

$$\text{ethylene conversion (\%)} = \frac{\text{moles of carbon in the overall detected products}}{\text{overall moles of carbon detected at the outlet}} * 100\%$$

$$C_n\text{selectivity} = \frac{\text{moles of carbon in } C_n \text{ group}}{\text{moles of carbon in the overall detected products}} * 100\%$$

$$\text{TOR} = \frac{\text{moles of ethylene converted}}{\text{moles of Co in } Co/SiO_2} * 100\%$$

3.2.5 H_2/D_2 Exchange

The H_2/D_2 isotopic exchange experiments were performed using a Micromeritics Autochem II 2920 chemisorption analyzer, equipped with a residual gas analyzer (RGA - Model 200, Stanford Research Systems). This experiment allowed the quantification of H_2 adsorbed on the Co catalysts for formation of hydrides intermediates. Approximately 0.050 to 0.100 g of the Co^{II}/SiO_2 catalysts were loaded into a quartz U-tube reactor and initially treated in flowing air (8.3-16.7 cm^3s^{-1} g_{cat}^{-1}, 99.999% UHP, Matheson Tri-Gas) at 500°C for dehydration of the surface. The temperatures were then changed to the target experimental temperatures: 200°C, 250°C, 450°C and 550°C. For each experiment, a new load of catalyst was used to assure a clean surface, free of previous hydrides species. Once the temperatures were reached, a mixture of 5% H_2 in balance Ar was flowed over the catalyst for 1 hour to ensure complete surface coverage. The gas flow was switched to 5% D_2 in balance Ar for an additional 1 to 2 hours, until HD detector response reached a baseline. By switching the gases from H_2 to D_2, the physiosorbed H_2 on the Co sites reacted with D_2 to form HD. This gas scrambling procedure was carried out twice to assure accurate and stability of the quantified moles over time. Background corrections were performed by carrying out the experiments on both the empty quartz tube and pure SiO_2 loads at the same weight loading.

The combination of H_2, D_2, and HD was detected using the RGA. The H_2 and D_2 consumption corresponded to the HD formation stoichiometrically. Thus, the moles of HD formed for each experiment were averaged and normalized by the moles of Co in the Co^{II}/SiO_2 samples.

This ratio corresponds to the amount of Co-H formed on the surface, due to the stoichiometric ratios.

3.3 Results

3.3.1 Structural Characterization - X-Ray Spectroscopy (XAS)

The XAS measurements for the single site catalysts were performed at the Co K edge (7.709 keV). For in-situ characterization, the measurements were taken at room temperature in He atmosphere after pretreating at 500^{o}C in He. The XANES spectrum provides information regarding the oxidation state of the cobalt species in the catalyst, while the EXAFS spectrum gives information regarding the local coordination environment of the atomic species, such as coordination number and bond length.

The XANES spectrum for the Co^{II}/SiO_2 catalyst is shown in Figure 3.1A, along with CoO reference and Co foil. In a Co foil spectra, Co is fully reduced, i.e., Co^0, and the edge energy is expected at 7.709keV. In the CoO reference, the XANES energy is shifted to higher energy, 7.721 keV, Table 1. There is also a small pre-edge feature at 7.7097 keV. The similar shape of the white line and the presence of a pre-edge peak at 7.708 keV indicates that the oxidation state in the Co^{II}/SiO_2 catalyst is the same as that for the CoO reference. The pre-edge peak of Co^{II}/SiO_2 is also similar in energy to that in CoO confirming the Co^{+2} oxidation state of the catalyst similar to what was previously reported[16].

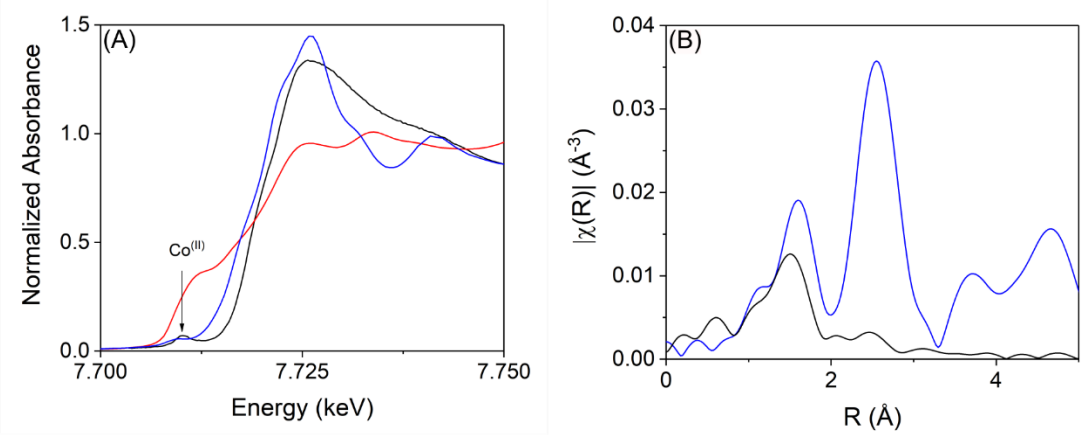

Figure 3.1. Spectra for both the (A) XANES and (B) EXAFS of Co^{II}/SiO2 Catalyst at the Co K edge. The Co^{II}/SiO2 catalyst is shown in black, metallic Co foil in red and CoO reference in blue.

Table 3.1. XAS Fitting results for the Fourier Transform Magnitude for the Co^{II}/SiO_2, Co foil and CoO reference at the Co K edge

Sample	Edge Energy (eV)	Pre-edge peak (keV)	Bond	Coordination Number (CN)	Bond Length (Å)
Co foil	7.7090	-	Co-Co	12.0	2.51
CoO	7.7210	7.7097	Co-O	6.0	2.13
			Co-Co	12.0	3.03
Co^{II}/SiO_2	7.7171	7.7093	Co-O	4.0	1.97

Figure 3.1B shows the k^2-weighted Fourier Transform (FT) magnitude of the CoO reference (blue line) at the Co K edge. In a CoO reference, the 6 Co-O bonds with a bond distance of 2.13 Å occur below about 2Å phase uncorrected distance in the FT magnitude. In CoO there are also higher shell Co-Co peaks around 3.0Å phase uncorrected distance. This translates to 12 Co-Co neighbors with bond distance of 3.03Å.. Thus, a CoO structure has 6 Co-O nearest neighbors and 12 Co-Co second nearest neighbors.

The FT of the Co^{II}/SiO_2 catalyst (Figure 3.1B, black line) shows the Co-O peaks are shifted to lower R compared to CoO and the smaller magnitude of the FT indicates fewer Co-O bonds. The fitting results from the first shell indicate there are 4 Co-O bonds at 1.97Å. There are no higher

shells above 2 Å distinguishable from background The $Co^{(II)}$ ions are present as a tetrahedral structure (4 O neighbors) bonded to the O atoms in the SiO_2 surface, similar to what was previously reported[16].

This catalyst was also pretreated under different conditions for in-situ characterization: (1) flowing 3.5%H_2 in balance He at 550ºC and scanned at room temperature He and (2) flowing 20%O_2 in balance He at 300ºC and scanned at room temperature He. These treatments were used to investigate whether different pretreatments would affect the local structures. Comparison of the 3 spectra showed no difference indicating the oxidation state and single site structure was maintained under oxidizing and reducing conditions up to 550ºC.

3.3.2 Propane Dehydrogenation and Propylene Hydrogenation

Similarly to catalytic performance previously reported by Hu *et al*[16], the Co^{II}/SiO_2 catalyst displays catalytic activity for both propane dehydrogenation (Figure 3.2) and propylene dehydrogenation.

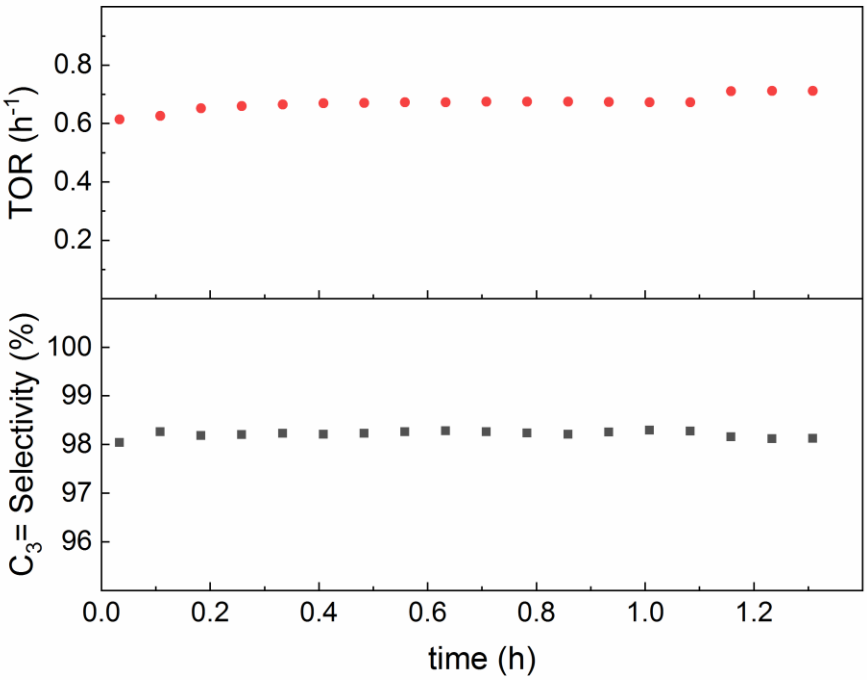

Figure 3.2. TOR (top) and propylene selectivity (bottom) for propane dehydrogenation reaction over time. Reaction conditions: 550°C, atmospheric pressure, flowrate of 82 mL/min, 3% C_3H_8, 2% H_2 in balance N_2.

Catalytic performance of propane dehydrogenation was evaluated at 550°C. Reaction flowrates and conditions were designed to achieve differential conversions, around 5%. Under similar conditions, equilibrium conversion is about 29%, assuring the measured conversions are below the equilibrium conversion. As shown on Figure 3.2, selectivity was stable around 98% and the TOR was measured as $0.6h^{-1}$. As indicated in Figure 3.2, there was no deactivation over a few hours during these tests in agreement to that observed by Hu *et al*[16].

Propylene hydrogenation activity was also confirmed for this catalyst at differential conversions of around 7%. Over a few hours of the test, there was no observed deactivation. The TOR was $1.2h^{-1}$ and no other products other than propane were observed in agreement with results reported by Hu *et al*[16].

The structural and catalytic characterizations confirm that the previously reported single site Co^{II}/SiO_2 catalyst has been prepared.

3.3.3 Ethylene Oligomerization

3.3.3.1 Ethylene oligomerization on Ni/SiO_2 and Co/SiO_2

Both single site catalysts were evaluated under the same for their C_2H_4 oligomerization activity. The maximum reported temperature for Ni catalysts were 250ºC for Ni supported on zeolites. The single site Ni/SiO_2 has been shown to be stable at this temperature and, hence, the ethylene oligomerization was carried out at 250ºC at 400 psi with varying space velocities and partial pressures for C_2H_4. For these experiments, 10 mL/min of 5% CH_4 in balance N_2 was cofed to be used as an internal standard. The Co^{II}/SiO_2 catalysts were also tested under the same conditions for comparison. The results are shown on Table 3.2.

Table 3.2. Comparison between single site Ni^{II}/SiO_2 and Co^{II}/SiO_2 at 250ºC a high pressure under varying space velocities and C_2H_4 flowrates

Catalyst [a]	C_2H_4[b] (atm)	C_2H_4 (mL/min)	WHSV (h^{-1})	Conv (%)	TOR (s^{-1})	Product Distribution (%)		
						C_4	C_6	C_8
Ni^{II}/SiO_2	22.7	50	3.8	20.5	1.5×10^{-2}	85.8	12.2	1.6
	24.0	75	5.6	15.7	1.7×10^{-2}	85.8	11.6	2.2
	19.4	25	1.9	20.4	7.4×10^{-3}	85.8	11.3	2.6
Co^{II}/SiO_2	22.7	50	3.8	0.04	2.8×10^{-5}	*tr.*[c]	*tr.*[c]	-
	20.4	30	2.3	0.03	1.3×10^{-5}	*tr.*[c]	*tr.*[c]	-
	13.6	10	0.8	0.03	4.9×10^{-6}	*tr.*[c]	*tr.*[c]	-

[a] Catalyst loading: 1.00 g of both Co^{II}/SiO_2 and Ni^{II}/SiO_2. [b] Total pressure: 400 psi; partial pressure was varied according to the total flowrate used. [c] trace amounts of C_4 and C_6 were detected.

As shown on Table 3.2, Ni^{II}/SiO_2 had a significantly higher conversion than Co^{II}/SiO_2 under the same conditions. At 250°C and 400 psi, Ni^{II}/SiO_2 showed a conversion between 15.7 and 20.5% conversion, with varying space velocities and C_2H_4 partial pressure. Due to the effect of the space velocities on the partial pressures, conversions were roughly the same at these conditions. The product distribution is also roughly the same, around 86% for C_4 linear isomers, 12% for C_6 isomers and 2% for C_8 isomers. For the C_4 oligomers, only linear olefins were observed (*cis*-2-butene, *trans*-2-butene, 1-butene) and isobutene formation was negligible, a selectivity of less than 0.1%.

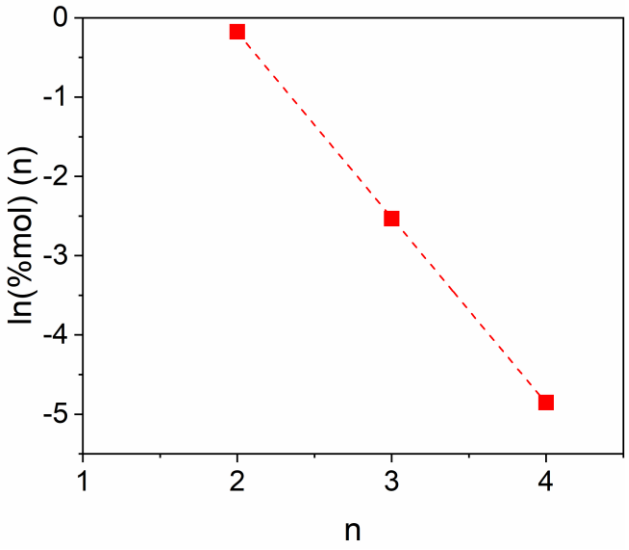

Figure 3.3. Schulz-Flory Distribution for Ni^{II}/SiO_2 single site catalysts, at 20.7% conversion, 22.7 atm partial pressure of C_2H_4. The y-axis is the natural log of the molar distribution of oligomers *vs* units of ethylene. The resulting fit for the linear graph was y=-2.3376x+4.49166, with an adjusted R^2=0.99996.

This products distribution follows a Schulz-Flory distribution, as shown in Figure 3.3. In this type of distribution, the slope of the linear curve gives the value of α by $\alpha=e^{slope}$. This represents the probability of chain growth, while the chain termination probability is given by 1- α[24]. According to the graph, α value for Ni^{II}/SiO_2 is about 0.10 This probability, i.e. 10%, is consistent with the high yield of C4 olefins obtained, as their formation was favored over the longer chains,

i.e. C_6 and C_8. This distribution agrees with previously proposed coordination-insertion mechanism for heterogeneous Ni catalysts[87], similar to a Cossee-Arlman mechanism for homogeneous catalysts.

The single site Co^{II}/SiO_2, on the other hand, shows a negligible conversion compared with Ni^{II}/SiO_2 under similar conditions. At the same weight hourly space velocity, 3.8 h^{-1}, conversion for Co^{II}/SiO_2 was roughly 0.04% with trace formation amounts of linear C_4 and C_6. At these conditions, the TOR for Co^{II}/SiO_2 is about 2.8 $x10^{-5}s^{-1}$, about 3 orders of magnitude lower than that of Ni^{II}/SiO_2, at 1.5 $x10^{-2}$. The C_2H_4 flowrates were lowered to achieve different space velocities but Co^{II}/SiO_2 gives negligible conversion under all conditions at 250ºC.

3.3.3.2 High Temperature ethylene oligomerization on Co/SiO_2

Due to the thermal stability and resistance to reduction of Co^{II}/SiO_2 for alkane dehydrogenation, the catalytic performance for olefin oligomerization was evaluated at elevated temperatures to achieve higher conversions. Initially the catalysts were evaluated at atmospheric pressure with temperatures varying from 250ºC to 350ºC and pure C_2H_4 flowrates from 2.7 to 16.6 mL/min and 1.00 to 2.00 g of catalyst. Under these conditions, Co^{II}/SiO_2 still showed poor activity with extremely low conversions between 0.01% and 1.0%, depending on the temperature. Since little butene production was observed, the reactions were then performed at 500 psi of C_2H_4 with a higher amount of catalyst, 1.00 to 2.00 g. Table 3.3 summarizes the conditions of each experiment, C_2H_4 conversion and product distribution.

Table 3.3. Catalytic performance of Co^{II}/SiO_2 at 500 psi of pure C_2H_4 (34 atm), with varying flowrates and temperatures.

T (^oC)	WHSV (h^{-1})	Conv. (%)	TOR (s^{-1})	Product Yield (%)						
				CH_4	C_2H_6	C_3[a]	C_4[b]	C_5	C_6	C_7+[c]
300[a]	0.4	0.7	4.5×10^{-5}	0.0	0.0	1.9	38.1	7.5	25.3	25.7
350[a]	1.9	3.0	1.0×10^{-3}	0.0	1.0	2.5	33.9	11.3	25.6	25.0
350[a]	1.1	4.6	9.7×10^{-4}	0.0	1.1	2.4	34.5	11.2	25.6	24.8
350[a]	0.2	7.3	2.6×10^{-4}	0.0	1.8	2.9	40.2	12.2	25.3	17.2
375[a]	0.4	18.3	1.3×10^{-3}	0.1	1.1	5.3	19.0	18.0	29.6	26.8
375[a]	0.9	13.5	2.4×10^{-3}	0.1	1.0	5.1	17.0	14.0	11.7	51.1
400[a]	1.9	16.2	5.7×10^{-3}	0.2	2.4	10.6	34.2	22.8	19.6	10.2
400[a]	0.9	19.1	3.4×10^{-3}	0.7	3.5	20.9	30.2	11.6	4.2	28.9
400[a]	0.4	32.7	2.3×10^{-3}	0.4	1.6	9.0	16.2	11.4	21.6	39.7
425[b]	9.4	86.9	-[c]	0.5	0.9	2.9	3.5	6.9	5.2	80.0
450[b]	5.6	98.5	-[c]	6.5	9.2	9.7	17.6	2.5	13.0	40.8
500[a]	2.8	99.3	-[c]	7.8	11.2	10.6	4.9	2.0	8.4	54.5

[a] Catalyst loading: 2.00 g of $Co^{(II)}/SiO_2$. [b] Catalyst loading: 1.00g of $Co^{(II)}/SiO_2$. [c] Conversion was too high for TOR to be determined

At higher pressures and temperatures, Co^{II}/SiO_2 becomes active towards ethylene conversions (Table 3.3). At 300^{o}C, Co^{II}/SiO_2 has a 0.7% conversion under 500 psi of C_2H_4 and most of the products are the expected oligomers, with C_4, C_6 and C_8 production. Small fractions of C_3 (propane and propylene), C_5 and C_7 are detected. As the temperature increases to 350^{o}C, the conversion ranges between 3.0% and 7.3%, depending on the space velocities. At this temperature,

the C_4 and C_6 isomers are still the highest yield product and maintain the same proportion observed for the lower temperature, around 30 to 40% and 25%, respectively. An increase in C_5 and the formation of C_2H_6 are also observed. The amount of C_5 isomers increases to about 12%, while a small yield, 1.5% of C_2H_6 appears. The yield of products higher than C_7 are about 17 to 25%.

At 400°C, the conversion increases significantly. An increase of 5-fold, from 10 mL/min to 50 mL/min, in the flowrate decreases conversion by about a half, from 33% to 16%. The trend observed in C_4 and C_6 products at lower temperatures are similar to those at lower temperature, and at 16.2% conversion the selectivity is about 34% and 20%, respectively. However, the selectivity of C_3 and C_5 products increased significantly, to 11% and 23% respectively, and the selectivity of C_7+ products decreased to 10%. As the conversion reached 32%, the amount of C_4 olefin isomers and C_5 decreased to 17% and 11%, while C_6 slightly increased and C_7+ increased significantly. The C_3 and C_2H_6 production remained roughly the same, while a small amount of CH_4 was produced.

At 500°C at a WHSV of 34.1h^{-1}, at nearly complete conversion (99.4%) of C_2H_4, 5% of the products are C_4 olefin isomers with only 2.0% C_5 and more than 70% are a mixture of C_6^+ olefins. A significant increase in the amount of low molecular weight products was also observed, with CH_4 and C_2H_6 yields of 8% and 11%, respectively, indicating an increase in thermal cracking side react. GC-MS analysis of these products revealed the presence of a mixture of isobutylene, C_5 and C_6 alkanes and alkenes, as well as the presence of some benzene and toluene products. Thus, as the conversion increases at high temperatures, an increase in light alkanes and higher molecular weights are observed and additional reactions occur, e.g., thermal cracking, isomerization and aromatization.

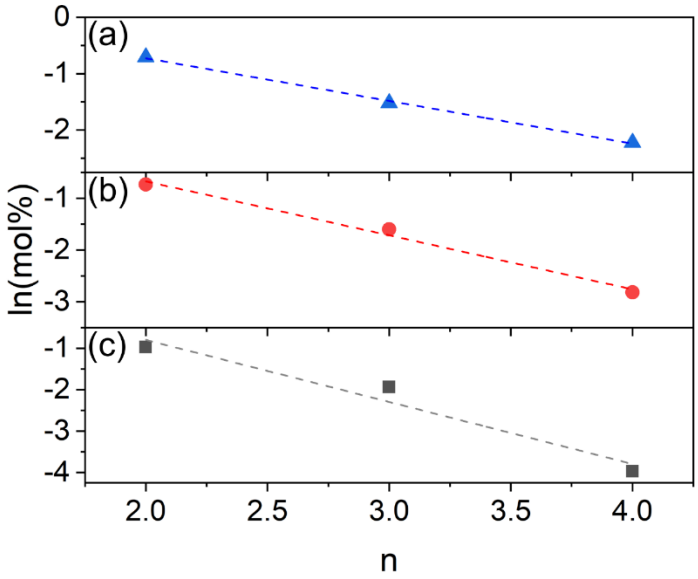

Figure 3.4. The Schulz-Flory distribution for C_4, C_6 and C_8 oligomer yields for Co^{II}/SiO_2. The y-axis is the natural log of the molar distribution of oligomers normalized by units of ethylene *vs* units of ethylene. (a) 0.7% conversion at 300°C, linear fit: y= -0.75703+0.78681, R^2= 0.99044; (b) 7.3% conversion at 350°C, linear fit: y= -1.04401x+1.41555, R^2= 0.99044; (c) 16.2% conversion at 400°C, linear fit: y= -1.49874x+2.20065, R^2= 0.9589.

Similar to Ni^{II}/SiO_2 oligomerization catalysts, the oligomer distribution on Co^{II}/SiO_2 also follows the Schulz-Flory distribution (Figure 3.4), for 300°C, 350°C and 400°C. The conversions at these temperatures were 0.7%, 7.3% and 16.2%, respectively. Based on the linear fits for each temperature, the slopes give α values of 0.47, 0.35 and 0.22, respectively. These higher results than that of Ni^{II}/SiO_2 is consistent with the higher yields of longer olefins for Co^{II}/SiO_2, given that α represents chain growth probability. A trend in the α values is observed, as the value decreases as the temperatures and conversions increase. As the conversions increased further, the Schulz Flory distribution was less reliable, likely due to the appearance of side reactions as the temperature increased, and a satisfactory fit was not obtained.

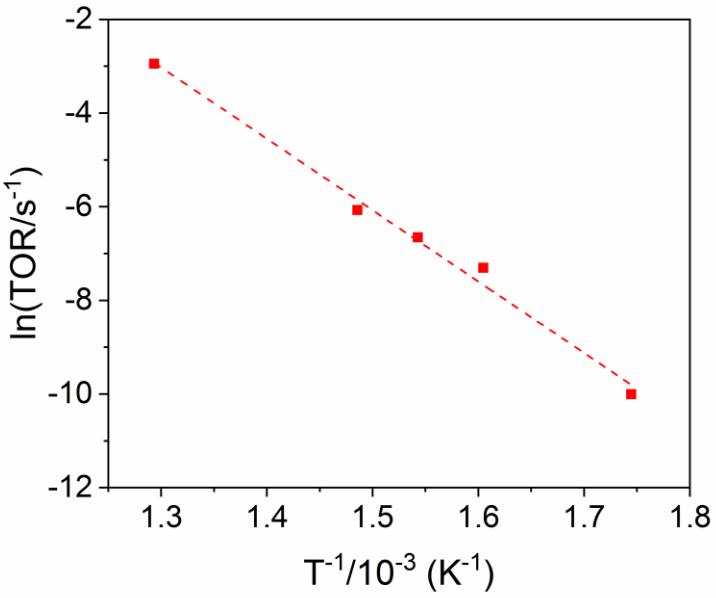

Figure 3.5. Arrhenius plot calculated from measured TOR for ethylene conversion on Co^{II}/SiO_2. The calculated TOR is shown as red squares. Reaction conditions: 10 mL/min of C_2H_4, total C_2H_4 pressure of 34.0 atm and varying conversions from 0.7% to 100%.

Due to the lack of deactivation of the Co^{II}/SiO_2 catalyst, the apparent activation energy was determined from an Arrhenius plot (Figure 3.5). The slope of the fitted curve is equivalent to the E_{app}/R, where E_{app} is the apparent activation energy and R is the ideal gas constant, 8.31 J mol^{-1} K^{-1}. The apparent activation energy is about 127 kJ/mol for ethylene oligomerization.

Although an extended life evaluation of Co^{II}/SiO_2 catalyst was not determined, the experiments at different space velocities and pressures were all carried out sequentially over the period of a several days. During this timeframe, there was no loss of activity. After experiments under harsher conditions and high conversions, the catalyst color changed from dark blue to black, likely due to carbon deposition on SiO_2. Regeneration of the catalysts was performed in a furnace at 550°C in flowing air. The catalysts regained the original blue color and no change in activity was observed after regeneration.

3.3.4 Reaction Intermediates Characterization

3.3.4.1 Difference Spectra – X-Ray Near Edge Spectroscopy (XANES)

Initial characterizations of the single site Co^{II}/SiO_2 catalyst with diluted gases (H_2, ethylene, etc.) in nitrogen and cooled to room temperature in He showed no difference in the EXAFS or XANES compared to drying in He, for example, spectra in Figure 3.1. This was likely due to the low partial pressure of the gases leading to low surface coverage of intermediates. Thus, new gas treatments were conducted to evaluate the potential to detect reactive intermediates and structural changes in the active sites under reaction conditions.

Additional EXAFS were performed after treatment with pure ethylene and H_2 to increase the Co surface species. The X-Ray near edge spectra (XANES) are shown in Figure 3.6A with H2 and Figure 3.6C with ethylene.

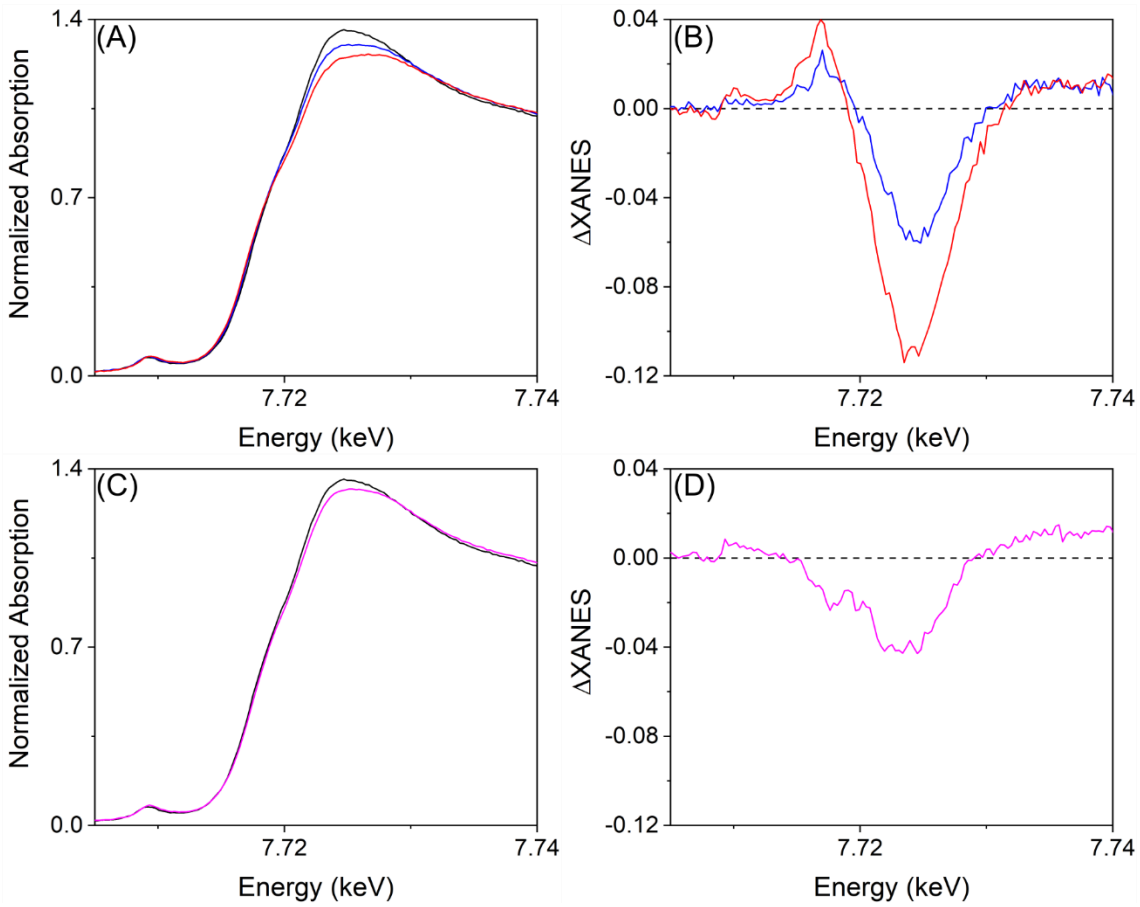

Figure 3.6. Comparison of XANES Spectra under different conditions and Difference XANES Spectra between each treatment spectrum and He at 500ºC Spectrum. (A) XANES Spectra for 500ºC in He (black), 200ºC in H_2 (blue) and 550ºC in H_2 (red); (B) Difference XANES for 200ºC in H_2 (blue) and 550ºC in H_2 (red); (C) XANES Spectra for 200ºC in C_2H_4 (magenta); (D) Difference XANES Spectrum for 200ºC in C_2H_4 (magenta).

As shown previously, the Co single site dehydrated in He at 500ºC (inert atmosphere) possesses a pre-edge peak at 7.7093 keV and edge energy at 7.7171 keV (Table 3.1). Both of these features slightly change under different treatments.

For the Co^{II}/SiO_2 treated in H_2 at 200ºC, both the pre-edge and edge energy remained at 7.7093 keV and 7.7171 keV, respectively (Table 3.4). Thus, the oxidation state remains Co^{2+}. However, a slight decrease in the white line is observed in comparison with inert atmosphere, He, which increases with increasing temperature, Figure 3.6A. For a better evaluation between these changes, difference spectra (ΔXANES) are plotted in Figure 3.6B by subtracting the 550ºC in He

spectrum from the spectrum of each H_2 treatment. Treatment in H_2, leads to increase in the energy of the leading edge of the XANES, but a decrease in the white line intensity.

The treatment at C_2H_4 at 200ºC had a slight shift towards higher energies for both the pre edge and edge energy, 7.7094 keV and 7.7174 keV (Table 3.4 and Figure 3.6C), respectively. Different from treatment in H_2, the ΔXANES of C_2H_4 (Figure 3.6D) shows a decrease in intensity of the leading edge of the XANES and decrease in the white line intensity.

When compared at the same temperature, the decrease in the white line is smaller in the C_2H_4 atmosphere compared to H_2. Also, the edge energy in the C_2H_4 shift towards higher energies, while XANES energy in H_2 shifts to lower energy.

3.3.4.2 Extended X-Ray Fine Structure (EXAFS)

The EXAFS spectra for the different treatments are shown in Figure 3.7, compared to the He pretreated catalyst: (A) Pretreated in H2 at 200oC, (B) Pretreated in H2 at 550oC, and (C) pretreated in C2H4 at 200oC. Table 3.4 shows the fits for CN and bond distances at the different treatments.

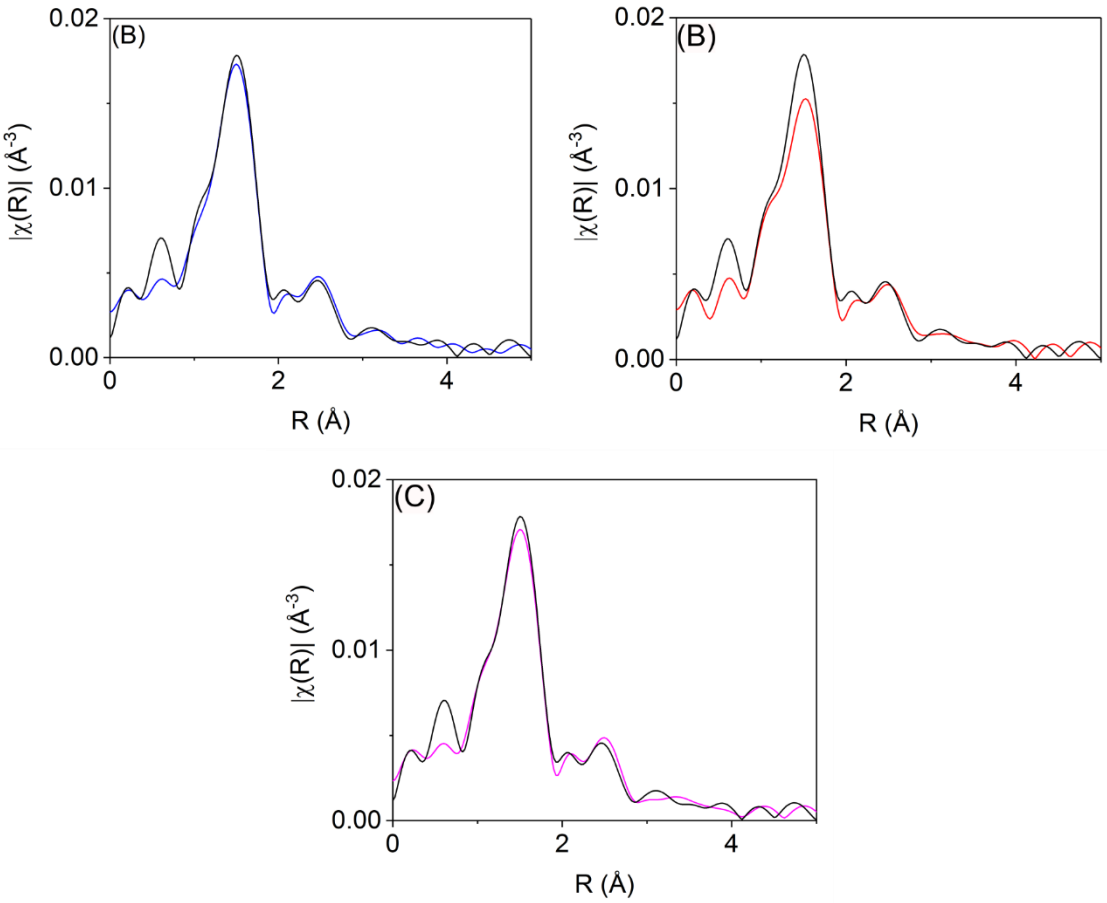

Figure 3.7. EXAFS FT magnitude of Co^{II}/SiO_2 catalyst under different treatments compared with 500°C in He (black line): (A) 200°C in H_2 (blue line), (magenta line) (B) 550°C in H_2 (red line), and (C) 200°C in C_2H_4.

Figure 3.7A shows the EXAFS FT-magnitude for the catalysts treated at 200°C in pure H_2 gas. The fits for this treatment show the Co-O CN of 3.9 at the bond length of 1.97Å. At higher reduction temperature, Figure 3.7B, there is a further decrease in the Co-O CN to 3.5 at 1.97 Å, consistent with the larger changes in XANES at higher temperature. Thus, comparison with the pretreated He, treatment in H_2 leads to decrease in the Co-O coordination. No increase in the magnitude of higher shells were observed, suggesting that the cobalt species were not reduced to metallic Co.

Table 3.4. Results from the EXAFS spectra for Co^{II}/SiO_2 at the Co K edge from the different treatments in inert and reactive atmospheres.

Treatment	Edge Energy (keV)	Pre-edge Energy (keV)	Bond	Coordination Number - CN	Bond Length (Å)	E_0 shift (eV)
500°C in He	7.7171	7.7093	Co-O	4.0	1.97	-1.3
200°C in H_2	7.7171	7.7093	Co-O	3.9	1.97	-0.6
200°C in C_2H_4	7.7174	7.7094	Co-O	3.9	1.97	-0.9
550°C in H_2	7.7167	7.7095	Co-O	3.5	1.97	0.8

Similar to the 200°C in H_2, pretreatments in C_2H_4 show a slight loss in Co-O coordination number (Figure 3.7C). Fits for Co-O show a CN of 3.9 and bond length of 1.97Å. Similar to the changes in XANES, the change in the EXAFS is small at 200°C.

3.3.4.3 H_2/D_2 Exchange

Isothermal H_2/D_2 exchange experiments were performed to determine whether Co^{II}/SiO_2 single site catalysts could form Co hydrides, which would also affect H/D exchange. The results are shown in Table 3.5, with the uptake of H_2 normalized per mole of Co.

Table 3.5 H_2/D_2 exchange results for the HD formation in Co^{II}/SiO_2 and Ni/SiO_2 catalyst, corrected for background and normalized by moles of Co.

Catalyst	H_2/D_2 Exchange Temperature	mol HD/mol Co
Co^{II}/SiO_2	250°C	0.26 ± 0.02
	450°C	0.54 ± 0.03

The resulting HD formation is shown to increase by almost a 2-fold from 250ºC to 450ºC. At 250ºC, there were about 0.26 moles of HD formed per mole of Co on the catalyst. At 450ºC, the formation increased to 0.54 moles of HD per mole of Co. Thus, the stoichiometric ratio suggests that the uptake of H_2 absorbed by the catalysts increases with increasing temperature. These results are also consistent with changes in intensity in the ΔXANES, Figure 3.6B.

3.4 Discussion

3.4.1 Catalyst Structure and Co^{II}-Hydride Formation

Consistent with the previous results for single site Co/SiO_2 propane dehydrogenation catalysts, XAS indicates the initial structure in He or air is a Co^{II} ion with 4 Co-O bonds at 1.97 Å. There is also little change in this structure up to about 550°C with low concentrations, e.g., < 5%, of H_2, propane or ethylene[66]. The XANES and EXAFS, however, show small changes in the Co^{II}/SiO_2 with higher concentrations of H_2 and C_2H_4, especially at high temperature. It was previously proposed that H_2 is heterolytically dissociated across the M-OSi bond in single site catalysts forming a M-H and SiO-H[66], [92]–[95]. Due to its low atomic number, there is no scattering from H atoms in the Co-H bond, for example. Since H_2 dissociation leads to a loss of Co-O bonds, the Co-H is inferred by the decrease in Co-O coordination. Additionally, these changes in the M ion coordination, i.e., loss of M-O and addition of M-H, yield a simultaneous change in the XANES white line intensity[92], [94], [95].

These XANES and EXAFS changes are small at 200°C consistent with the low oligomerization rate. At 250ºC, the oligomerization rate in single site Ni^{II}/SiO_2 is about 1000 times higher than that of Co^{II}. However, unlike Ni, which begins to reduce near 250°C[91], single site Co^{II} ions are resistant to reduction to NP's up to about 750°C[43], likely due to the distance

between Co-Co neighbors. At higher temperatures in presence of H_2, for example at 550°C, the XAS changes are larger, consistent with increased oligomerization rates.

As evidenced in this and previous study[66], catalytic hydrogenation of propylene, where propylene and hydrogen are the reactants, occurs at about 200°C. Isotopic exchange of H_2/D_2 shows that Co-H is formed around this temperature, albeit in low amounts. The molar fraction of Co-H is estimated to be about 0.26 mol/mol of Co at 250°C. At 450ºC, this increases to 0.56 mol/mol of Co, or about twice as much as formed at 250°C. Similarly, the changes in the ΔXANES spectra in 100% H_2, Figure 3.6B, approximately double upon increase of temperature to 550°C from 200ºC, consistent with the interpretation of formation of Co-H with the loss of Co-O bonds, Figure 3.7A and B. There are two conclusions from these results. First, single site Co^{II}/SiO_2 heterolytically dissociates H_2 and, second, the rates are low at about 200°C, but become significant at temperatures above 400°C.

Alkane dehydrogenation is an equilibrium limited reaction requiring high temperatures for significant conversion. In this and the previous study[66] of Co^{II}/SiO_2, propane dehydrogenation occurs at 550°C, suggesting that C-H bonds in alkanes can be possibly activated at high temperatures. For olefin oligomerization, likewise, the catalyst must form Co hydride and alkyl group in situ to play as a reaction intermediate. In the absence of added H_2, it is necessary to first activate a vinyl C-H bond of ethylene, forming a $Co\text{-}C_2H_3$ and SiO-H. As demonstrated here, C-H activation of ethylene can occur as low as 200°C, as shown in the XANES and EXAFS spectra in Figure 3.6D and Figure 3.7C, respectively. At this low temperature, however, the rates and surface coverage are low and almost negligible conversion is obtained. Nevertheless, ethylene activation is possible. As the catalytic performance indicates (Table 3.3), higher temperatures and pressure favor higher rates and conversions.

3.4.2 Reaction Mechanism for Oligomerization

Based on the reaction conditions and TOR for both single sites Co^{II}/SiO_2 and Ni^{II}/SiO_2 at 250ºC, it's clear that single-site Ni/SiO_2 has a TOR about 1000 times higher than that of Co^{II}/SiO_2. Ni^{II} catalysts on zeolites operate at high pressures with temperatures in the range of 50ºC to 250ºC. The Brønsted acid sites on zeolites have been reported to enhance the catalytic activity of Ni^{II} sites. In addition to the typical linear, even-numbered carbon products for ethylene oligomerization, branched and odd numbered carbon products are produced. These are thought to result from secondary reactions of the primary oligomerization products over Brønsted acid sites in the zeolite[29], [36], [39], [40], [96]–[100]. As shown in this paper, the single site Ni^{II}/SiO_2 showed catalytic activity at 250ºC and varying C_2H_4 partial pressures, with a TOR around $1.5x10^{-2}$ s^{-1}. The structure of the active site is a tetrahedral Ni^{II} ion covalently bonded on the surface if silica[24]. In the absence of acid sites, the products displayed a typical Schulz-Flory distribution of even-numbered oligomerization products. The reported Ni supported on zeolite catalysts reported on the literature are evaluated at much lower temperatures and their TOR's vary from 1.5 x10 h^{-1} to 1.4 $x10^3$ h^{-1}, i.e., $4.2x10^{-3}$ to $4.0 x10^{-1}$ s^{-1} with the higher TOR found on MCM-41[36], [83], [99]. Thus, the TOR of Ni^{II}/SiO_2 on this study can be up to 100 times lower than those reported for ion exchanged Ni^{II} in zeolites. Both on zeolites and SiO_2, the maximum reported temperature for these catalytic evaluations have been 250ºC. Higher temperatures have not been reported due to reduction of Ni^{2+} active sites to metallic Ni^0 NP's.

For both heterogeneous and homogeneous catalysts, Co has a much lower intrinsic TOR than Ni. In a recent study by Xu *et al* [90], CoO clusters supported on N-doped carbon supports were reported with maximum conversion of 32% for ethylene oligomerization at 80ºC and 31 bar, with about 50% C_2H_4 and balance He. In our study, the single site Co^{II}/SiO_2 catalysts were evaluated under the similar conditions and displayed negligible ethylene oligomerization conversion.

Significant conversions were only observed at much higher temperatures, starting at 300°C. Previous reports have shown that CoO clusters reduce around 320°C[101], [102]. High conversion for ethylene oligomerization for the latter catalyst is only possible since the single site Co^{II} is resistant to reduction up to high reaction temperature, 750°C[43].

The mechanism of ethylene oligomerization for Ni^{II} ions in zeolites has been proposed[14]. Initiation is thought to occur by heterolytic dissociation of a vinyl C-H bond of ethylene forming a Ni^{II}-C_2H_3 and an Al-O(H)-Si Brønsted acid site. An additional ethylene insertion and β-H elimination give a stoichiometric yield of butylene and Ni^{II}-hydride intermediate. Olefin propagation occurs by additional ethylene insertion forming longer Ni^{II}-alkyl intermediates. β-H elimination of these longer alkyl gives the oligomerization products, i.e. C_6 and C_8, and recovers the Ni^{II}-hydride. In zeolites, even in those which prior to reaction do not have Brønsted sites, the formed acid sites lead to secondary reactions of the primary oligomer products, e.g, isomerization and cracking, leading to branched olefins and olefins with odd carbon numbers, for example, propylene and i-pentene.

The results for Co^{II}/SiO_2 oligomerization are consistent with the mechanism proposed for Ni^{II}/zeolite catalysts[14]. Propane dehydrogenation and changes in the EXAFS after reaction with ethylene suggest that Co^{II}/SiO_2 activate C-H bonds in alkanes and olefins at temperatures as low as 200°C. Propylene hydrogenation suggests that Co^{II}-H bonds insert olefins and similarly suggests Co^{II}-alkyl groups catalyze the same reaction. Finally, like Ni^{II} ions, β-hydrogen elimination from Co^{II} ions would be expected. Three factors distinguish heterogeneous oligomerization on Co^{II}/SiO_2 from Ni^{II}/zeolite catalysts. As previously discussed, Ni^{II} sites are significantly more reactive at 250°C, about 1000 times higher TOR, than Co^{II} sites. Although the intrinsic rate of Co^{II} is low, significant catalytic rates are possible at much higher reaction

temperatures since the active site is difficult to reduce. Second, on zeolite catalysts, initiation leads to Brønsted acid sites; while on SiO_2 supports, initiation leads to non-acidic silanol groups. This leads to a different product distribution. On the former, isomerization and cracking occur giving high selectivity to branched and odd numbered olefin products. On silica, at low temperature a typical Schulz-Flory product distribution is obtained, as shown by the Ni^{II}/SiO_2; while (much) higher temperatures favors low selectivity to olefin hydrogenation, hydrogenolysis, isomerization and even aromatization products. Finally, Co^{II}/SiO_2 oligomerization leads to higher molecular weight products than Ni^{II} catalysts. While higher molecular weight products on zeolites would undergo acid catalyzed cracking, even on Ni^{II}/SiO_2 no hydrocarbons with greater than 8 carbons were observed and the α value from Schulz-Flory was much lower than those observed for Co^{II}/SiO_2.

The reaction intermediates and reaction steps generally accepted for the Cossee-Arlman oligomerization mechanism [24], [35] are similar to those thought responsible for olefin hydrogenation and alkane dehydrogenation of heterogeneous single site catalysts[66], [92]–[95], [103]. For all three reactions (olefin oligomerization and hydrogenation and alkane dehydrogenation), metal hydride and alkyl intermediates are key intermediates. In addition, β-hydrogen elimination is necessary to yield olefin products by oligomerization and alkane dehydrogenation. The proposed relationship between the three pathways is shown in Figure 3.8.

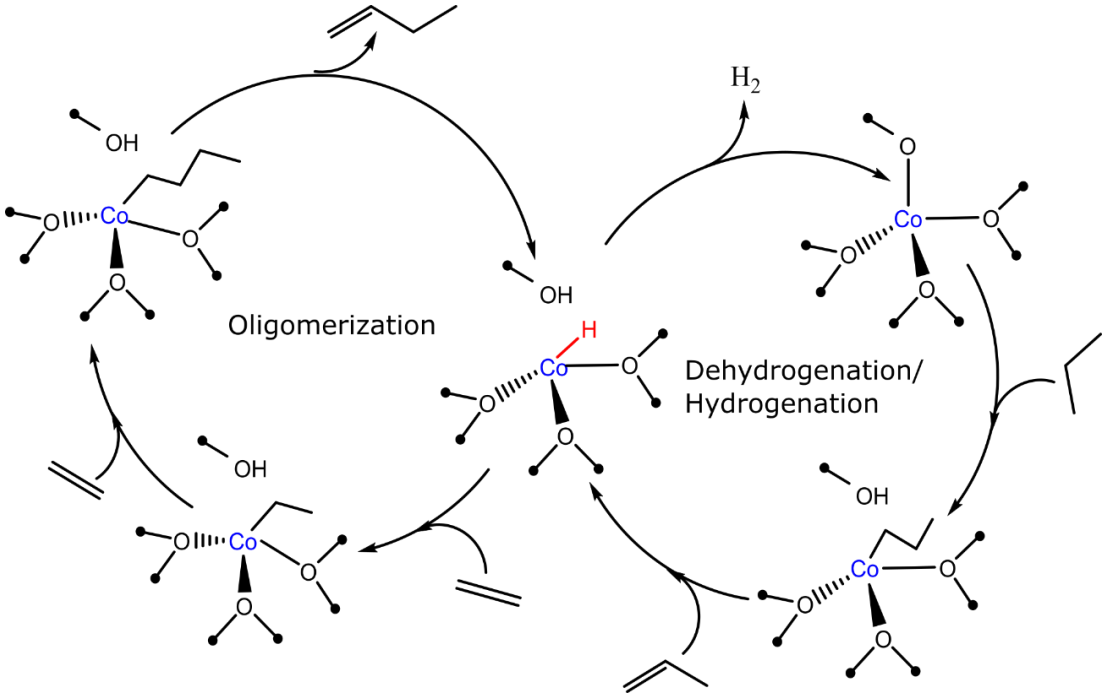

Figure 3.8. Proposed pathways for alkane dehydrogenation, alkene hydrogenation (right catalytic cycle) and ethylene oligomerization (right catalytic cycle). All pathways have common Co-H and Co-R reaction intermediates.

While alkane dehydrogenation, olefin oligomerization and oligomerization have common reaction intermediates and elementary reaction steps, the reaction conditions differ. Although alkane dehydrogenation and olefin oligomerization occur at about the same temperature, the former is favored at low pressure, while the latter is favored at high pressure. Thus, higher molecular weight products were not observed during dehydrogenation.

Olefin hydrogenation was previously studied at low temperature and hydrogen partial pressure and the rate would be expected to increase with increasing temperature and pressure, for example at 500°C. During higher temperature oligomerization low selectivity to aromatics suggests that small amounts of H_2 may also have been produced. These would be expected to saturate olefins giving small amounts of alkanes.

3.4.3 Prospects

Homogenous olefin oligomerization catalysts are generally tailored to give highly selective product distributions, primarily for production of chemical intermediates, for example, 1-butene. Due to the high reaction temperature and multiple catalytic pathways which occur on these heterogeneous Co^{II}/SiO_2 catalysts, high selectivity to a single product seems unlikely. However, limited deactivation, facile regeneration and structural stability make this ideal for production of transportation fuels, especially, diesel and distillate fuels. With vast amounts of ethane available in shale gas production, especially in remote areas, excess olefin production could be converted to premium motor fuels by olefin oligomerization on Co^{II}/SiO_2 catalysts. The products are primarily linear olefins, with small amounts of branched olefins and aromatics. The products are also S-free and have no polyaromatic compounds. Mild hydrogenation of the products a premium diesel fuel for local markets.

3.5 Conclusion

Cobalt single site catalysts, Co^{II}/SiO_2, have been shown to be thermally stable at temperatures as high as 550^{o}C through propane dehydrogenation, used as a probe reaction. Despite its low activity compared to Ni^{II}/SiO_2 at 250^{o}C under the same conditions, Co^{II}/SiO_2 was highly active at a higher temperature range, from 350^{o}C to 500^{o}C, at 34.0 atm of C_2H_4. XAS characterization indicates the catalyst is Co^{II} with 4 Co-O bonds at 1.97 Å. The XANES, EXAFS and H_2/D_2 isotopic scrambling suggest that H_2 forms approximately 25% surface coverage of Co^{II} hydride bonds at 250°C, with approximately 50% at 450°C. C_2H_4 is also shown to react poorly at the Co^{II} single sites at 250°C.

At 250^{o}C and 400 psi, Ni^{II}/SiO_2 has a TOR of about 1000 times higher than Co^{II}/SiO_2. The latter has little rate at temperatures typical of heterogeneous, Ni^{II} oligomerization catalysts.

However, Co^{II}/SiO_2 is stable to much higher reaction temperatures, thus high olefin conversion can be obtained above about 400°C. At these elevated temperatures, however, additional reactions occur leading to moderate selectivity to odd-numbered carbon hydrocarbons, e.g., C_3, C_5 and C_7, isomerized olefins, aromatics and alkanes. Key reaction intermediates (Co^{II} hydride and alkyl groups) and elementary reaction steps (alkylation and β-hydride elimination) for olefin oligomerization are similar to those for alkane dehydrogenation and olefin hydrogenation.

4. SUMMARY

The works in this dissertation elucidate some of the fundamental knowledge for the development of catalysts for upgrading light alkanes into fuel grade higher olefins.

In the first half, bimetallic catalysts with two active metals, Pt and Co, were synthesized and evaluated for propylene selectivity. The use of several characterization techniques allowed the differentiation between the surface and core structures in these catalysts. More specifically, a traditional bulk analysis technique, EXAFS, was successfully used for a surface analysis of these catalysts. The difference spectra between the oxidized and reduced catalysts allowed the identification of the same surface, Pt_3Co, in all the catalysts despite the increasing loading of Co. At low Co loadings, the interior of the nanoparticle was formed of monometallic Pt core, while the surface consisted of Pt_3Co. As the Co loading increased, the Co atoms were allowed to diffuse into the nanoparticle, achieving a homogeneous Pt_3Co structure throughout the nanoparticle radial composition. At the highest loadings, the Co atoms further diffused inside the nanoparticle, forming a Co-rich core, with a PtCo phase, in an AuCu structure. Not all Co atoms were alloyed, though. At the lowest to medium loadings of Co, some Co^{2+} ions remained on the surface as Co^{2+} single sites on the SiO_2. At the highest loading, the excess Co species fully reduced into monometallic Co nanoparticles.

All the catalysts were probed for propane dehydrogenation and showed similar propylene selectivity and a TOR similar to monometallic Pt. The similar selectivity reinforces the fact not only reinforces that the catalysts share a similar surface, but also shows the effects of geometry over selectivity. Meanwhile, the similar TOR to Pt suggests that Pt is the active site, while Co behaves as non-active metal. It is believed the isolation of Pt sites inhibits the side reaction,

hydrogenolysis, and, consequentially, the selectivity towards propylene are increased. Thus, geometric effects determine the selectivity upon alloying Pt and non-active promoters. This work shows that, despite Pt and Co being active in their monometallic counterparts, Co catalysts are much lower in activity than Pt and, upon Pt-Co alloy formation, Co behaves as a non-active promoter, while Pt is the preferred active site for reaction. This further reinforces the understanding that ordered alloy structures are necessary for dehydrogenation reaction and their geometric effects enhances the selectivity towards the desired products.

The proper identification of the surface and its correlation to the geometric effects was only possible due to the difference EXAFS spectra analysis. The application of this methodology helped elucidate the complex alloy formation involved in the nanoparticle synthesis.

In the second half of this work, Cobalt single site catalysts, Co^{II}/SiO_2, have been shown to be highly active at high temperatures, despite its negligible conversion at temperatures lower than 250^{o}C. As evidenced by the *in-situ* EXAFS characterization, the Co^{2+} active sites remain stable with the same oxidation state, suggesting ethylene conversion occurs through a non-redox reaction mechanism. This stability as maintained at temperatures as high as 550^{o}C. Under reaction conditions, the active site Co^{2+} go through a loss of Co-O bonds to form the reaction intermediates, either Co-H or Co-alkyls. The XANES, EXAFS and H_2/D_2 isotopic scrambling suggest that Co-H formation is favored at higher temperatures and, consequentially, Co-alkyl formation is also favored, increasing the ethylene oligomerization reaction rates. Key reaction intermediates (Co^{II} hydride and alkyl groups) and elementary reaction steps (alkylation and β-hydride elimination) for olefin oligomerization are similar to those for alkane dehydrogenation and olefin hydrogenation. However, the elevated temperatures also favor side reactions, such as hydrogenation, thermal

cracking and aromatization, as evidenced by the high conversions and the odd-numbered hydrocarbons in the product distribution.

Nonetheless, ethylene oligomerization is possible at high temperatures, given the catalyst is thermally stable. The oligomerization catalysts reported have always been evaluated at low temperatures, from 50ºC to 200ºC due to the easy reduction of Ni^{2+} catalysts to metallic Ni and the pore blockage of zeolites due to longer chains of hydrocarbons. These Co^{II}/SiO_2 catalyst suggest that C-H bond activation at high temperature is also favored for oligomerization reactions, as well as for dehydrogenation. A practical application of this finding is that coupling both reactions in an industrial process is economically feasible, given that they can happen under similar conditions, with small modifications required.

4.1 Recommendation for Future Work

Based on the projects developed on this dissertation, the suggested future work would focus on expanding the understanding of single site catalysts for ethylene oligomerization at high temperatures. Homogeneous Nickel catalysts have been developed to target specific oligomer compositions. These catalysts are likely more selective towards dimers than longer oligomers. In the case of single site $Co^{(II)}$ on SiO_2, the catalysts showed a wide range of products at high temperatures, including odd-numbered olefins, such as C_5 and C_7. This type of product distribution is expected from the Nickel catalysts supported on zeolites, due to the presence of Brønsted acid sites promoting side reactions. The non-acidic nature of SiO_2 support suggest that the side reactions present on $Co^{(II)}/SiO_2$ are likely due to the elevated temperatures.

Future work with these catalysts should focus on understanding the effect of the temperature and conversion on the product distribution. By changing other reaction parameters, such as the ethylene pressure and WHSV, lower conversions at higher temperatures could be achieved. This

would facilitate the analysis of the temperature on the products and understand, for example, whether methane and propane formation are due to the thermal cracking of these catalysts. Multiple reaction pathways are involved under these conditions and efforts in understanding them are crucial.

For these experiments to be carried out, the High-Pressure reactor design would also need to be improved. At the high conversion, liquid higher molecular weight olefins were produced. Due to the temperature gradient in the reactor, these would condense on the reactor lines exposed to room temperature, making data collection and leak testing a strenuous process.

Additionally, the dehydrogenation and hydrogenation reactions can be used as probe reactions for suitable catalysts to be studied at similar conditions. For example, the single site Ni-P/SiO_2 catalyst developed by Guanghui *et al* is a promising candidate for this high temperature oligomerization. The presence of P ligands inhibited the reduction of Ni^{2+} for dehydrogenation reactions at 650^{o}C. Given the intrinsic selectivity of Nickel towards dimers over other catalysts, a comparison of the activity and the product distribution between the $Co^{(II)}/SiO_2$ and the Ni-P/SiO_2 is also suggested.

With the current abundance of ethane sources and the increase in the number of ethane cracker plants being built, the supply of ethylene will largely increase in the market. The low deactivation of these catalysts and high temperature stability might allow their use at similar conditions as the ethane crackers. Despite the low selectivity towards specific products, these catalysts achieved a wide range of olefin products, making it a suitable catalyst to be used in the diesel production from ethane, for example.

APPENDIX

A. SUPPORTING INFORMATION FOR CHAPTER 3

A.1. $Co^{(II)}/SiO_2$ Spectra from Different Pretreatments

The $Co^{(II)}/SiO_2$ were pretreated under different conditions before data measurements for EXAFS to evaluate whether the pre-treatments would affect the catalyst structures. In addition to the dehydration at 500°C in He, the catalyst was also pretreated in flowing air at 300°C and 3.5% H_2 in balance N_2 at 550°C. After pretreatments, the catalysts were cooled down in flowing He and scanned at room temperature. The spectra are shown in **Figure A.4.1** and the respective fittings are shown in Table A.1.

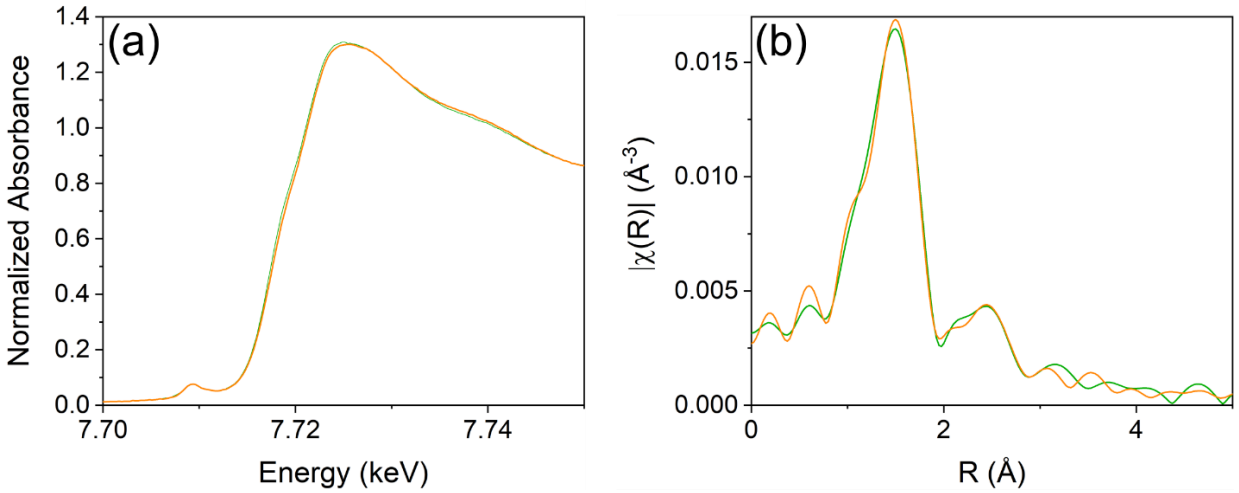

Figure A.4.1. Spectra for both the (A) XANES and (B) EXAFS of $Co^{II}/SiO2$ Catalyst at the Co K edge after different pre-treatments. The pretreatment under air at 300°C is shown in orange, while that of 550°C in H_2 is shown in green.

Table A.1. XAS Fitting results for the Fourier Transform Magnitude for the Co^{II}/SiO_2 at the Co K edge from different pretreatments

Pre-treatment	Edge Energy (keV)	Pre-edge Energy (keV)	Bond	Coordination Number - CN	Bond Length (Å)	E_0 shift (eV)
500°C in He	7.7171	7.7093	Co-O	4.0	1.97	-1.3
550°C in H_2	7.7172	7.7093	Co-O	4.0	1.97	-0.7
300°C in Air	7.7176	7.7093	Co-O	4.0	1.97	-0.9

As shown in Figure A.4.1A, there is no noticeable difference in the white line intensity between the two pretreatments. Both the edge energy and pre-edge peak are located around the same energies (Table A.1), suggesting that the coordination environment around Co was not affected by the pre-treatments and its oxidation state remained the same as Co^{2+}. Further analysis of the FT magnitude of the EXAFS spectra for both pre-treatments and the pretreatment at 500°C in He confirms the coordination environment remains the same, as the Co-O CN remains 4.0 and its bond distance remains at 1.97Å (Table A.1). Therefore, these different pre-treatments for the single site Co^{II}/SiO_2 catalysts does not show noticeable changes in its structure.

REFERENCES

[1] M. A. B. Siddiqui, A. M. Aitani, M. R. Saeed, N. Al-Yassir, and S. Al-Khattaf, "Enhancing propylene production from catalytic cracking of Arabian Light VGO over novel zeolites as FCC catalyst additives," *Fuel*, vol. 90, no. 2, pp. 459–466, 2011.

[2] J. C. Mol, "Industrial applications of olefin metathesis," *J. Mol. Catal. A Chem.*, vol. 213, no. 1, pp. 39–45, 2004.

[3] J. J. H. B. Sattler, J. Ruiz-Martinez, E. Santillan-Jimenez, and B. M. Weckhuysen, "Catalytic Dehydrogenation of Light Alkanes on Metals and Metal Oxides," *Chem. Rev.*, vol. 114, no. 20, pp. 10613–10653, 2014.

[4] B. K. Bahuleyan, D.-W. Park, C.-S. Ha, and I. Kim, "Advances in late transition metal catalysts for olefin polymerization/oligomerizarion," *Catal. Surv. from Asia*, vol. 10, no. 2, pp. 65–73, 2006.

[5] X. Ding, C. Li, and C. Yang, "Study on the oligomerization of ethylene in fluidized catalytic cracking (FCC) dry gas over metal-loaded HZSM-5 catalysts," *Energy and Fuels*, vol. 24, no. 7, pp. 3760–3763, 2010.

[6] P. Sun, G. Siddiqi, M. Chi, and A. T. Bell, "Synthesis and characterization of a new catalyst Pt/Mg(Ga)(Al)O for alkane dehydrogenation," *J. Catal.*, vol. 274, no. 2, pp. 192–199, 2010.

[7] F. T. Zangeneh, S. Sahebdelfar, and M. Bahmani, "Propane Dehydrogenation over a Commercial Pt-Sn/Al_2O_3 Catalyst for Isobutane Dehydrogenation: Optimization of Reaction Conditions," *Chinese J. Chem. Eng.*, vol. 21, no. 7, pp. 730–735, 2013.

[8] X. Fan, J. Li, Z. Zhao, Y. Wei, J. Liu, A. Duan, and G. Jiang, "Dehydrogenation of propane over PtSn/SBA-15 catalysts: effect of the amount of metal loading and state," *RSC Adv.*, vol. 5, no. 36, pp. 28305–28315, 2015.

[9] G. J. Siri, J. M. Ramallo-López, M. L. Casella, J. L. G. Fierro, F. G. Requejo, and O. A. Ferretti, "XPS and EXAFS study of supported PtSn catalysts obtained by surface organometallic chemistry on metals: Application to the isobutane dehydrogenation," *Appl. Catal. A Gen.*, vol. 278, no. 2, pp. 239–249, 2005.

[10] H. Xiong, S. Lin, J. Goetze, P. Pletcher, H. Guo, L. Kovarik, K. Artyushkova, B. M. Weckhuysen, and A. K. Datye, "Thermally Stable and Regenerable Platinum–Tin Clusters for Propane Dehydrogenation Prepared by Atom Trapping on Ceria," *Angew. Chemie - Int. Ed.*, vol. 56, no. 31, pp. 8986–8991, 2017.

[11] Y. X. Li, K. J. Klabunde, and B. H. Davis, "Alloy formation in supported PtSn catalysts: Mossbauer studies," *J. Catal.*, vol. 128, no. 1, pp. 1–12, 1991.

[12] G. Siddiqi, P. Sun, V. Galvita, and A. T. Bell, "Catalyst performance of novel Pt/Mg(Ga)(Al)O catalysts for alkane dehydrogenation," *J. Catal.*, vol. 274, no. 2, pp. 200–206, 2010.

[13] J. R. Gallagher, D. J. Childers, H. Zhao, R. E. Winans, R. J. Meyer, and J. T. Miller, "Structural evolution of an intermetallic Pd–Zn catalyst selective for propane dehydrogenation," *Phys. Chem. Chem. Phys.*, vol. 17, pp. 28144–28153, 2015.

[14] S. Collins, M. Baltanas, J. Garciafierro, and A. Bonivardi, "Gallium–Hydrogen Bond Formation on Gallium and Gallium–Palladium Silica-Supported Catalysts," *J. Catal.*, vol. 211, no. 1, pp. 252–264, 2002.

[15] J. Wu, S. Mallikarjun Sharada, C. Ho, A. W. Hauser, M. Head-Gordon, and A. T. Bell, "Ethane and propane dehydrogenation over PtIr/Mg(Al)O," *Appl. Catal. A Gen.*, vol. 506, pp. 25–32, 2015.

[16] Z. Ma, Z. Wu, and J. T. Miller, "Effect of Cu content on the bimetallic Pt-Cu catalysts for propane dehydrogenation," *Catal. Struct. React.*, vol. 3, no. 1–2, pp. 43–53, 2017.

[17] Z. Wu, B. C. Bukowski, Z. Li, C. Milligan, L. Zhou, T. Ma, Y. Wu, Y. Ren, F. H. Ribeiro, W. N. Delgass, J. Greeley, G. Zhang, and J. T. Miller, "Changes in Catalytic and Adsorptive Properties of 2 nm Pt3Mn Nanoparticles by Subsurface Atoms," *J. Am. Chem. Soc.*, vol. 140, no. 44, pp. 14870–14877, 2018.

[18] E. C. Wegener, Z. Wu, H. T. Tseng, J. R. Gallagher, Y. Ren, R. E. Diaz, F. H. Ribeiro, and J. T. Miller, "Structure and reactivity of Pt–In intermetallic alloy nanoparticles: Highly selective catalysts for ethane dehydrogenation," *Catal. Today*, vol. 299, no. October 2016, pp. 146–153, 2018.

[19] Z. Wu, E. C. Wegener, H.-T. Tseng, J. R. Gallagher, J. W. Harris, R. E. Diaz, Y. Ren, F. H. Ribeiro, and J. T. Miller, "Pd–In intermetallic alloy nanoparticles: highly selective ethane dehydrogenation catalysts," *Catal. Sci. Technol.*, vol. 6, no. 18, pp. 6965–6976, 2016.

[20] J. I. Martínez-Araya, R. Quijada, and A. Toro-Labbé, "The mechanism of ethylene polymerization reaction catalyzed by group IVB metallocenes. A rational analysis through the use of reaction force," *J. Phys. Chem. C*, vol. 116, no. 40, pp. 21318–21325, 2012.

[21] J. T. Dixon, M. J. Green, F. M. Hess, and D. H. Morgan, "Advances in selective ethylene trimerisation - A critical overview," *J. Organomet. Chem.*, vol. 689, no. 23, pp. 3641–3668, 2004.

[22] Z. Xu, J. P. Chada, D. Zhao, C. A. Carrero, Y. T. Kim, D. C. Rosenfeld, J. L. Rogers, S. J. Rozeveld, I. Hermans, and G. W. Huber, "Production of Linear Octenes from Oligomerization of 1-Butene over Carbon-Supported Cobalt Catalysts," *ACS Catal.*, vol. 6, no. 6, pp. 3815–3825, 2016.

[23] D. S. McGuinness, "Olefin oligomerization via metallacycles: Dimerization, trimerization, tetramerization, and beyond," *Chem. Rev.*, vol. 111, no. 3, pp. 2321–2341, 2011.

[24] G. J. P. Britovsek, R. Malinowski, D. S. McGuinness, J. D. Nobbs, A. K. Tomov, A. W. Wadsley, and C. T. Young, "Ethylene Oligomerization beyond Schulz-Flory Distributions," *ACS Catal.*, vol. 5, no. 11, pp. 6922–6925, 2015.

[25] K. P. Tellmann, V. C. Gibson, A. J. P. White, and D. J. Williams, "Selective dimerization/oligomerization of α-olefins by cobalt bis(imino)pyridine catalysts stabilized by trifluoromethyl substituents: Group 9 metal catalysts with productivities matching those of iron systems," *Organometallics*, vol. 24, no. 2, pp. 280–286, 2005.

[26] B. L. Small and R. Schmidt, "Comparative Dimerization of 1-Butene with a Variety of Metal Catalysts, and the Investigation of a New Catalyst for C□H Bond Activation," *Chem. - A Eur. J.*, vol. 10, no. 4, pp. 1014–1020, 2004.

[27] I. Introduction, "Dimerization Ethylene Catalyzed Transition-Metal," no. 1, pp. 353–399, 1986.

[28] G. Allegra, "Discussion on the mechanism of polymerization of a-olefins with Ziegler-Natta catalysts," *Makromol. Chem.*, vol. 145, pp. 235–246, 1971.

[29] F. Speiser, P. Braunstein, and L. Saussine, “Catalytic ethylene dimerization and oligomerization: recent developments with nickel complexes containing P,N-chelating ligands,” *Acc. Chem. Res.*, vol. 38, no. 10, pp. 784–793, 2005.

[30] W. Keim, “NICKEL HYDRIDES: CATALYSIS IN OLIGOMERIZATION AND POLYMERIZATION REACTIONS OF OLEFINS,” *Ann. N. Y. Acad. Sci.*, vol. 415, no. 1, pp. 191–200, 1983.

[31] L. Fan, A. Krzywicki, A. Somogyvari, and T. Ziegler, “A theoretical study of ethylene oligomerization by organometallic nickel catalysts,” *Stud. Surf. Sci. Catal.*, vol. 100, no. C, pp. 507–514, 1996.

[32] R. Robinson, D. S. Mcguinness, and B. F. Yates, “The mechanism of ethylene dimerization with the Ti(OR′) 4/AlR3 catalytic system: DFT studies comparing metallacycle and Cossee proposals,” *ACS Catal.*, vol. 3, no. 12, pp. 3006–3015, 2013.

[33] D. S. McGuinness, J. A. Suttil, M. G. Gardiner, and N. W. Davies, “Ethylene oligomerization with Cr-NHC catalysts: Further insights into the extended metallacycle mechanism of chain growth,” *Organometallics*, vol. 27, no. 16, pp. 4238–4247, 2008.

[34] R. Arteaga-Müller, H. Tsurugi, T. Saito, M. Yanagawa, S. Oda, and K. Mashima, “New tantalum ligand-free catalyst system for highly selective trimerization of ethylene affording 1-hexene: New evidence of a metallacycle mechanism,” *J. Am. Chem. Soc.*, vol. 131, no. 15, pp. 5370–5371, 2009.

[35] S. Forget, H. Olivier-Bourbigou, and D. Delcroix, “Homogeneous and Heterogeneous Nickel-Catalyzed Olefin Oligomerization: Experimental Investigation for a Common Mechanistic Proposition and Catalyst Optimization,” *ChemCatChem*, vol. 9, no. 12, pp. 2408–2417, 2017.

[36] A. Finiels, F. Fajula, and V. Hulea, “Nickel-based solid catalysts for ethylene oligomerization – a review,” *Catal. Sci. Technol.*, vol. 4, no. 8, pp. 2412–2426, 2014.

[37] S. Moussa, M. A. Arribas, P. Concepción, and A. Martínez, “Heterogeneous oligomerization of ethylene to liquids on bifunctional Ni-based catalysts: The influence of support properties on nickel speciation and catalytic performance,” *Catal. Today*, vol. 277, pp. 78–88, 2016.

[38] E. D. Metzger, R. J. Comito, C. H. Hendon, and M. Dincă, “Mechanism of single-site molecule-like catalytic ethylene dimerization in Ni-MFU-4l,” *J. Am. Chem. Soc.*, vol. 139, no. 2, pp. 757–762, 2017.

[39] an Mlinar, B. Keitz, D. Gygi, and E. Bloch, “Selective Propene Oligomerization with Nickel (II)-Based Metal-Organic Frameworks,” *ACS Catal.*, vol. 4, no. Ii, pp. 717–721, 2014.

[40] A. N. Mlinar, G. B. Baur, G. G. Bong, A. Getsoian, and A. T. Bell, “Propene oligomerization over Ni-exchanged Na-X zeolites,” *J. Catal.*, vol. 296, pp. 156–164, 2012.

[41] J. F. Knifton, J. R. Sanderson, and P. E. Dai, “Olefin oligomerization via zeolite catalysis,” *Catal. Letters*, vol. 28, no. 2–4, pp. 223–230, 1994.

[42] R. Henry, M. Komurcu, Y. Ganjkhanlou, R. Y. Brogaard, L. Lu, K. J. Jens, G. Berlier, and U. Olsbye, “Ethene oligomerization on nickel microporous and mesoporous-supported catalysts: Investigation of the active sites,” *Catal. Today*, vol. 299, no. February 2017, pp. 154–163, 2018.

[43] L. G. Cesar, C. Yang, Z. Lu, Y. Ren, G. Zhang, and J. T. Miller, “Identification of a Pt 3 Co Surface Intermetallic Alloy in Pt–Co Propane Dehydrogenation Catalysts,” *ACS Catal.*, pp. 5231–5244, 2019.

[44] J. H. Sinfelt, “Catalytic Specificity,” *AIChE J.*, vol. 19, no. 4, pp. 673–683, 1973.

[45] R. D. Cortright and J. A. Dumesic, “Effects of Potassium on Silica-Supported Pt and Pt/Sn Catalysts for Isobutane Dehydrogenation,” *J. Catal.*, vol. 157, no. 2, pp. 576–583, Dec. 1995.

[46] P. Sun, G. Siddiqi, W. C. Vining, M. Chi, and A. T. Bell, “Novel Pt/Mg(In)(Al)O catalysts for ethane and propane dehydrogenation,” *J. Catal.*, vol. 282, no. 1, pp. 165–174, 2011.

[47] Y. Zhang, Y. Zhou, A. Qiu, Y. Wang, Y. Xu, and P. Wu, “Propane dehydrogenation on PtSn/ZSM-5 catalyst: Effect of tin as a promoter,” *Catal. Commun.*, vol. 7, no. 11, pp. 860–866, 2006.

[48] H. N. Pham, J. J. H. B. Sattler, B. M. Weckhuysen, and A. K. Datye, "Role of Sn in the Regeneration of Pt/γ-Al_2O_3 Light Alkane Dehydrogenation Catalysts," *ACS Catal.*, vol. 6, pp. 2257–2264, 2016.

[49] F. T. Zangeneh, S. Mehrazma, and S. Sahebdelfar, "The influence of solvent on the performance of Pt-Sn/θ-Al_2O_3 propane dehydrogenation catalyst prepared by co-impregnation method," *Fuel Process. Technol.*, vol. 109, pp. 118–123, 2013.

[50] F. T. Zangeneh, A. Taeb, K. Gholivand, and S. Sahebdelfar, "Kinetic study of propane dehydrogenation and catalyst deactivation over Pt-Sn/Al_2O_3 catalyst," *J. Energy Chem.*, vol. 22, no. 5, pp. 726–732, 2013.

[51] O. A. Barias, A. Holmen, and E. a Blekkan, "Propane Dehydrogenation over Supported Pt and Pt-Sn Catalysts: Catalyst Preparation, Characterization, and Activity Measurements," *J. Catal.*, vol. 12, no. 158, pp. 1–12, 1996.

[52] S. Gómez-Quero, T. Tsoufis, P. Rudolf, M. Makkee, F. Kapteijn, and G. Rothenberg, "Kinetics of propane dehydrogenation over Pt-Sn/Al_2O_3," *Catal. Sci. Technol.*, vol. 3, no. 4, pp. 962–971, 2013.

[53] A. D. Ballarini, P. Zgolicz, I. M. J. Vilella, S. R. de Miguel, A. A. Castro, and O. A. Scelza, "n-Butane dehydrogenation on Pt, PtSn and PtGe supported on γ-Al_2O_3 deposited on spheres of α-Al_2O_3 by washcoating," *Appl. Catal. A Gen.*, vol. 381, no. 1–2, pp. 83–91, 2010.

[54] S. A. Bocanegra, O. A. Scelza, and S. R. De Miguel, "Behavior of PtPb/MgAl2O4 catalysts with different Pb contents and trimetallic PtPbIn catalysts in n-butane dehydrogenation," *Appl. Catal. A Gen.*, vol. 468, pp. 135–142, 2013.

[55] C. Ye, Z. Wu, W. Liu, Y. Ren, G. Zhang, and J. T. Miller, "Structure Determination of a Surface Tetragonal Pt1Sb1Phase on Pt Nanoparticles," *Chem. Mater.*, vol. 30, no. 14, pp. 4503–4507, 2018.

[56] M. Boudart, A. Aldag, J. E. Benson, N. A. Dougharty, and C. G. Harkins, "On the Specific Activity of Platinum Catalysts," *J. Catal.*, vol. 6, pp. 92–99, 1966.

[57] M. Boudart, “Catalysis by Supported Metals,” *Adv. Catal.*, vol. 20, pp. 153–166, 1969.

[58] J. Manassen, “The Mechanism of Dehydration of Alcohols over Alumina Catalysts,” *Adv. Catal.*, vol. 16, pp. 49–93, 1966.

[59] M. Che and C. O. Bennett, “The Influence of Particle Size on the Catalytic Properties of Supported Metals,” *Adv. Catal.*, vol. 36, pp. 55–172, 1989.

[60] J. K. A. Clarke and J. J. Rooney, “Stereochemical Approaches to Mechanisms of Hydrocarbon Reactions on Metal Catalysts,” *Adv. Catal.*, vol. 25, pp. 125–183, 1976.

[61] V. J. Cybulskis, B. C. Bukowski, H.-T. Tseng, J. R. Gallagher, Z. Wu, E. Wegener, A. J. Kropf, B. Ravel, F. H. Ribeiro, J. Greeley, and J. T. Miller, “Zinc Promotion of Platinum for Catalytic Light Alkane Dehydrogenation: Insights into Geometric and Electronic Effects,” *ACS Catal.*, vol. 7, no. 6, pp. 4173–4181, 2017.

[62] H. Okamoto, “Co-Pt (Cobalt-Platinum),” *J. Phase Equilibria*, vol. 22, no. 5, pp. 591–591, Oct. 2001.

[63] N. Du, C. Wang, R. Long, and Y. Xiong, “N-doped carbon-stabilized PtCo nanoparticles derived from Pt@ZIF-67: Highly active and durable catalysts for oxygen reduction reaction,” *Nano Res.*, vol. 10, no. 9, pp. 3228–3237, 2017.

[64] C. Song, D. Zhang, B. Wang, Z. Cai, P. Yan, Y. Sun, K. Ye, D. Cao, K. Cheng, and G. Wang, “Uniformly grown PtCo-modified Co_3O_4 nanosheets as a highly efficient catalyst for sodium borohydride electrooxidation,” *Nano Res.*, vol. 9, no. 11, pp. 3322–3333, 2016.

[65] B. A. T. Mehrabadi, S. Eskandari, U. Khan, R. D. White, and J. R. Regalbuto, “A Review of Preparation Methods for Supported Metal Catalysts,” *Adv. Catal.*, vol. 61, pp. 1–35, 2017.

[66] B. Hu, A. Bean Getsoian, N. M. Schweitzer, U. Das, H. Kim, J. Niklas, O. Poluektov, L. A. Curtiss, P. C. Stair, J. T. Miller, and A. S. Hock, “Selective propane dehydrogenation with single-site Co^{II} on SiO_2 by a non-redox mechanism,” *J. Catal.*, vol. 322, pp. 24–37, 2015.

[67] C. A. Schneider, W. S. Rasband, and K. W. Eliceiri, “NIH Image to ImageJ: 25 years of image analysis,” *Nat. Methods*, vol. 9, no. 7, pp. 671–675, 2012.

[68] T. Ressler, “WinXAS: A program for X-ray absorption spectroscopy data analysis under MS-Windows,” *J. Synchrotron Radiat.*, vol. 5, no. 2, pp. 118–122, 1998.

[69] B. Ravel and M. Newville, "ATHENA, ARTEMIS, HEPHAESTUS: Data analysis for X-ray absorption spectroscopy using IFEFFIT," *J. Synchrotron Radiat.*, vol. 12, no. 4, pp. 537–541, 2005.

[70] A. P. Hammersley, S. O. Svensson, M. Hanfland, A. N. Fitch, and D. Häusermann, "Two-dimensional detector software: From real detector to idealised image or two-theta scan," *High Press. Res.*, vol. 14, no. 4–6, pp. 235–248, 2007.

[71] L. Lutterotti, D. Chateigner, S. Ferrari, and J. Ricote, "Texture, residual stress and structural analysis of thin films using a combined X-ray analysis," *Thin Solid Films*, vol. 450, no. 1, pp. 34–41, 2004.

[72] J. T. Miller, A. J. Kropf, Y. Zha, J. R. Regalbuto, L. Delannoy, C. Louis, E. Bus, and J. A. van Bokhoven, "The effect of gold particle size on Au-Au bond length and reactivity toward oxygen in supported catalysts," *J. Catal.*, vol. 240, no. 2, pp. 222–234, 2006.

[73] S. Saedy, D. Palagin, O. Safonova, J. A. van Bokhoven, A. A. Khodadadi, and Y. Mortazavi, "Understanding the Mechanism of Synthesis of Pt3Co Intermetallic Nanoparticles via Preferential Chemical Vapor Deposition," *J. Mater. Chem. A*, vol. 5, pp. 24396–24406, 2017.

[74] J. C. Woolley, J. H. Phillips, and J. A. Clark, "Ordering in CoPt-CrPt and CoPt-MnPt alloys," *J. Less Common Met.*, vol. 6, no. 6, pp. 461–471, Jun. 1964.

[75] E. Raub, "Metals and alloys of the platinum group," *J. Less Common Met.*, vol. 1, no. 1, pp. 3–18, 1959.

[76] K. H. J. Buschow, P. G. van Engen, and R. Jogenbreur, "Magneto-optical properties of metallic ferromagnetic materials," *J. Magn. Magn. Mater.*, vol. 38, no. 1, pp. 1–22, Aug. 1983.

[77] S. U. Jen, "Effect of atomic order on some physical properties of $Co_{25}Pt_{75}$," *J. Alloys Compd.*, vol. 234, no. 2, pp. 231–234, Feb. 1996.

[78] R. P. Chambers and M. Boudart, "Lack of Dependence of Conversion on Flow Rate in Catalytic Studies," *J. Catal.*, vol. 6, pp. 141–145, 1966.

[79] M. Boudart, “Turnover Rates in Heterogeneous Catalysis,” *Chem. Rev.*, vol. 95, no. 3, pp. 661–666, 1995.

[80] V. Galvita, G. Siddiqi, P. Sun, and A. T. Bell, “Ethane dehydrogenation on Pt/Mg(Al)O and PtSn/Mg(Al)O catalysts,” *J. Catal.*, vol. 271, no. 2, pp. 209–219, 2010.

[81] L. Nykänen and K. Honkala, “Density functional theory study on propane and propene adsorption on Pt(111) and PtSn alloy surfaces,” *J. Phys. Chem. C*, vol. 115, no. 19, pp. 9578–9586, 2011.

[82] S. Moussa, P. Concepción, M. A. Arribas, and A. Martínez, “Nature of Active Nickel Sites and Initiation Mechanism for Ethylene Oligomerization on Heterogeneous Ni-beta Catalysts,” *ACS Catal.*, vol. 8, no. 5, pp. 3903–3912, 2018.

[83] M. Lallemand, A. Finiels, F. Fajula, and V. Hulea, “Continuous stirred tank reactor for ethylene oligomerization catalyzed by NiMCM-41,” *Chem. Eng. J.*, vol. 172, no. 2–3, pp. 1078–1082, 2011.

[84] W. Keim, “Oligomerization of Ethylene to a-Olefins: Discovery and Development of the Shell Higher Olefin Process (SHOP),” *Angew. Chemie - Int. Ed.*, vol. 52, pp. 12492–12496, 2013.

[85] A. M. Al-Jarallah, J. A. Anabtawi, M. A. B. Siddiqui, A. M. Aitani, and W. A. Al-Sa’doun, “Ethylene dimerization and oligomerization to butene-1 and linear α-olefins: A review of catalytic systems and processes,” *Catal. Today*, vol. 14, no. 1992, pp. 1–121, 1992.

[86] O. Jan, K. Song, A. Dichiara, and F. L. P. Resende, “Ethylene Oligomerization over Ni-Hβ Heterogeneous Catalysts,” *Ind. Eng. Chem. Res.*, vol. 57, no. 31, pp. 10241–10250, 2018.

[87] R. Joshi, G. Zhang, J. T. Miller, R. Gounder, and C. D. Davidson, “Evidence for the Coordination-Insertion Mechanism of Ethene Dimerization at Nickel Cations Exchanged onto Beta Molecular Sieves Evidence for the Coordination---Insertion Mechanism of Ethene Di---merization at Nickel Cations Exchanged onto Beta Molecular S,” 2018.

[88] R. Y. Brogaard and U. Olsbye, “Ethene Oligomerization in Ni-Containing Zeolites: Theoretical Discrimination of Reaction Mechanisms,” *ACS Catal.*, vol. 6, no. 2, pp. 1205–1214, 2016.

[89] C. T. O'Connor, L. L. Jacobs, and M. Kojima, "Propene oligomerization over synthetic mica-montmorillonite (SMM) and SMM incorporating nickel, zinc and cobalt," *Appl. Catal.*, vol. 40, no. C, pp. 277–290, 1988.

[90] Z. Xu, J. P. Chada, L. Xu, D. Zhao, D. C. Rosenfeld, J. L. Rogers, I. Hermans, M. Mavrikakis, and G. W. Huber, "Ethylene Dimerization and Oligomerization to 1-Butene and Higher Olefins with Chromium-Promoted Cobalt on Carbon Catalyst," *ACS Catal.*, vol. 8, no. 3, pp. 2488–2497, 2018.

[91] G. Zhang, C. Yang, and J. T. Miller, "Tetrahedral Nickel(II) Phosphosilicate Single-Site Selective Propane Dehydrogenation Catalyst," *ChemCatChem*, vol. 10, no. 5, pp. 961–964, 2018.

[92] N. M. Schweitzer, B. Hu, U. Das, H. Kim, J. Greeley, L. A. Curtiss, P. C. Stair, J. T. Miller, and A. S. Hock, "Propylene hydrogenation and propane dehydrogenation by a single-site Zn2+ on silica catalyst," *ACS Catal.*, vol. 4, no. 4, pp. 1091–1098, 2014.

[93] B. Hu, N. M. Schweitzer, G. Zhang, S. J. Kraft, D. J. Childers, M. P. Lanci, J. T. Miller, and A. S. Hock, "Isolated Fe^{II} on silica as a selective propane dehydrogenation catalyst," *ACS Catal.*, vol. 5, no. 6, pp. 3494–3503, 2015.

[94] V. J. Cybulskis, S. U. Pradhan, J. J. Lovón-Quintana, A. S. Hock, B. Hu, G. Zhang, W. N. Delgass, F. H. Ribeiro, and J. T. Miller, "The Nature of the Isolated Gallium Active Center for Propane Dehydrogenation on Ga/SiO2," *Catal. Letters*, vol. 147, no. 5, pp. 1252–1262, 2017.

[95] A. Getsoian, U. Das, J. Camacho-Bunquin, G. Zhang, J. R. Gallagher, B. Hu, S. Cheah, J. A. Schaidle, D. A. Ruddy, J. E. Hensley, T. R. Krause, L. A. Curtiss, J. T. Miller, and A. S. Hock, "Organometallic model complexes elucidate the active gallium species in alkane dehydrogenation catalysts based on ligand effects in Ga K-edge XANES," *Catal. Sci. Technol.*, vol. 6, no. 16, pp. 6339–6353, 2016.

[96] M. Iwamoto and Y. Kosugi, "Highly Selective Conversion of Ethene to Propene and Butenes on Nickel Ion-Loaded Mesoporous Silica Catalysts Highly Selective Conversion of Ethene to Propene and Butenes on Nickel Ion-Loaded Mesoporous Silica Catalysts," *Society*, pp. 1–4, 2007.

[97] C. P. Nicholas, “Applications of light olefin oligomerization to the production of fuels and chemicals,” *Appl. Catal. A Gen.*, vol. 543, no. June, pp. 82–97, 2017.

[98] A. N. Mlinar, S. Shylesh, O. C. Ho, and A. T. Bell, “Propene oligomerization using Alkali metal- and nickel-exchanged mesoporous aluminosilicate catalysts,” *ACS Catal.*, vol. 4, no. 1, pp. 337–343, 2014.

[99] M. Lallemand, A. Finiels, F. Fajula, and V. Hulea, “Ethylene oligomerization over Ni-containing mesostructured catalysts with MCM-41, MCM-48 and SBA-15 topologies,” *Stud. Surf. Sci. Catal.*, vol. 170, no. B, pp. 1863–1869, 2007.

[100] I. Agirrezabal-Telleria and E. Iglesia, “Stabilization of active, selective, and regenerable Ni-based dimerization catalysts by condensation of ethene withinordered mesopores,” *J. Catal.*, vol. 352, pp. 505–514, 2017.

[101] L. D. Souza, L. Jiao, J. R. Regalbuto, J. T. Miller, and A. J. Kropf, “Preparation of silica- and carbon-supported cobalt by electrostatic adsorption of Co (III) hexaammines,” vol. 248, pp. 165–174, 2007.

[102] L. J. Garces, B. Hincapie, R. Zerger, and S. L. Suib, “The Effect of Temperature and Support on the Reduction of Cobalt Oxide: An in Situ X‐ray Diffraction Study,” *J. Phys. Chem. C*, vol. 119, pp. 5484–5490, 2015.

[103] Y. Zhao, H. Sohn, B. Hu, J. Niklas, O. G. Poluektov, J. Tian, M. Delferro, and A. S. Hock, “Zirconium Modification Promotes Catalytic Activity of a Single-Site Cobalt Heterogeneous Catalyst for Propane Dehydrogenation,” *ACS Omega*, vol. 3, no. 9, pp. 11117–11127, 2018.

VITA

Laryssa G. Cesar was born and raised in a Northern city in Brazil, Manaus, in the heart of the Amazon Rainforest. She received her with a B.S. in Chemical Engineering in December 2014 from the University of the State of Amazonas, in Brazil. During her undergraduate years, she was actively engaged in the small student organization in her college, where she acted as a class representative and was also one of the organizers of the Chemical Engineering Week event in her city. She worked with undergraduate research in mathematical models for chemical compounds under the guidance of Dr. Claudia Candida Silva. In August 2015, she started her Ph.D. in Chemical Engineering at Purdue University as a Science without Borders Fellow, received from the Brazilian Government. She worked under the under the advising of Dr. Jeffrey T. Miller. Her research focused on the study of structural effects on heterogeneous catalytic activity. Her thesis work focused on the geometric effects and identification of Pt-Co bimetallic catalysts for propane dehydrogenation and characterization of single sites $Co^{(II)}/SiO_2$ catalysts for ethylene oligomerization at high temperatures, using *in-situ* Synchrotron X-Ray techniques. During her Ph.D, she also worked as an intern in the EOEG group at DOW, Freeport, TX, during summer 2018. Upon graduation in August 2019, she will join the Engineered Materials Process R&D group within Performance Silicones at Dow Chemical, Midland, MI.